NANOPLATE SURFACTANTS AND LIQUID CRYSTALS

A Dissertation

by

MINXIANG ZENG

Submitted to the Office of Graduate and Professional Studies of
Texas A&M University
in partial fulfillment of the requirements for the degree of

DOCTOR OF PHILOSOPHY

Chair of Committee,	Zhengdong Cheng
Committee Members,	Micah J. Green
	Svetlana Sukhishvili
	Lei Fang
Head of Department,	M. Nazmul Karim

December 2018

Major Subject: Chemical Engineering

ABSTRACT

Low-dimensional 2D materials, *i.e.*, nanoplates, show exceptional properties such as high surface area/volume ratio that make these materials important for applications demanding high levels of surface/interface interactions at nanoscale. Despite significant advances of nanoplates in energy applications, the role of nanoplates in binary complex fluids (*e.g.*, emulsions) or anisotropic fluids (*e.g.*, liquid crystals) remains underexplored. In this dissertation, we developed various surface-engineered nanoplates and investigated their collective behaviors as colloid surfactants, liquid crystals, and active soft materials. 2D nanoplates have been synthesized for use in stabilizing oil-in-water emulsions and regulating molecular delivery systems, in which they can interact with large amounts of key molecules, allowing superior control over transport/diffusion kinetics. In addition, strongly anisotropic nanoplates have also been developed with tunable photonic bandgaps and corresponding iridescent colors across the full visible spectrum in colloidal suspensions. We envision that the control of self-assembly of 2D building blocks would enable bottom-up fabrication of emerging multifunctional soft materials for diverse applications including specialty surfactants, photonic sensors, pollutant removal, and smart delivery systems.

ACKNOWLEDGEMENTS

I would like to express my sincere appreciation to my advisor Dr. Zhengdong Cheng. I would like to thank Dr. Cheng for his support, suggestions and encouragement throughout my research in Texas A&M University. Benefited from Dr. Cheng's every bit of guidance, assistance, and expertise, I readily adapted to life in Cheng laboratory during my first few semesters, and ventured into research on my own and branch out into new research areas. I am very grateful for the freedom that Dr. Cheng gave me for choosing the research topics, at the same time continuing to contribute valuable feedback, advice, and encouragement. The fully positive and committed attitude of Dr. Cheng in science has deeply inspired me and confirmed me to pursue my academic career.

I also want to thank all my committee members, Dr. Micah J. Green, Dr. Svetlana Sukhishvili, and Dr. Lei Fang, for their guidance and support throughout my graduate study. Without their help, finishing this dissertation would have been impossible. I am thankful to Dr. Green, an expert in 2D materials, for his help and guidance to my graphene quantum dots research. I also really appreciate Dr. Sukhishvili for her insightful comments and for sharing with me her tremendous experience in the polymer science. I am very appreciative of Dr. Fang for help and commitment to serve on my dissertation committee on such a short notice as a replacement for Dr. Mannan. I would like to express my gratitude for Dr. M. Sam Mannan (former thesis committee member), an excellent professor and pioneer in the safety and environmental engineering, who unfortunately passed away a few weeks before the official dissertation defense.

I would like to give thanks to my friends, colleagues, faculty, and staff in the department, for making my stay at Texas A&M University such a great journey. Special thanks to my fellow labmates Lecheng Zhang, Dali Huang, Dr. Ling Wang, Abhijeet Shinde, Shijun Lei, Mingfeng Chen, Hai Li, Carlos Mejia, Yi-Hsien Yu, Henry Lin, Daniel King, Ian Echols, Jianyu Li, and Ilse Nava for the stimulating discussions, for the wonderful collisions of research ideas, and for the good time we had been working together.

Last but not the least, I would like to express my deepest gratitude to my family and friends. This dissertation would not have been possible without their warm love, continued patience, and endless support. I would give special thanks to my grandmother Meide Chen, whose role in my life is immense. This last word of acknowledgment I have reserved for my dear wife Qingye Ma, who has been with me all these years and has made them the best years of my life.

CONTRIBUTORS AND FUNDING SOURCES

Contributors

This work was supervised by a thesis committee consisting of Dr. Zhengdong Cheng (advisor and committee chair) and Dr. Micah J. Green (committee member) of Texas A&M Artie McFerrin Department of Chemical Engineering, Dr. Svetlana Sukhishvili (committee member) of Texas A&M Material Science and Engineering Department, and Dr. Lei Fang (committee member) of Texas A&M Chemistry Department.

The author acknowledges the great contribution from Dr. Micah J. Green and Smit Alkesh Shah in the research of graphene quantum dots, Dali Huang, Lecheng Zhang, Xuezhen Wang, Dr. Baoliang Peng in the research of particle surfactants, Daniel King, Dr. Ling Wang in the research of active nanoplatelets, Abhijeet Shinde, Shijun Lei, Mingfeng Chen in the research of nanoplatelet liquid crystals, and Ian Echols, Dr. M. Sam Mannan in the research of 2D membranes.

Funding Sources

The author acknowledges financial support from PetroChina Scientific Research and Technology Development Project (2014A-1001-01), Texas A&M Water Seed Grant (28-163024-00001), Texas A&M Aggie Challenge Program, and NASA (NASA-NNX13AQ60G).

NOMENCLATURE

2D	Two-dimensional
BF	Barium ferrite
PtBF	Pt-coated barium ferrite
BP	Black phosphorus
COF	Covalent organic framework
GO	Graphene oxide
GQD	Graphene quantum dot
C_{18}-GQD	Octadecyl-GQD
C-GQD	Carboxyl-GQD
N-GQD	Amino-GQD
S-GQD	Sulfonate-GQD
KGM	Konjac glucomannan
KGMF	KGM-modified fabric
MXene	Transition metal carbide
MOF	Metal organic framework
PMFP	Polymer-modified filter paper

SJP	Smart jamming platelet
TMD	Transition metal dichalcogenide
ZrP	Zirconium hydrogenphosphate
ZrPM	ZrP-functionalized membrane
CVD	Chemical vapor deposition
DI	Deionized
SEM	Scanning electron microscopy
FTIR	Fourier transform infrared
TEM	Transmission electron microscopy
SEM	Scanning electron microscopy
XPS	X-ray photoelectron spectroscopy

TABLE OF CONTENTS

LIST OF FIGURES

CHAPTER I

INTRODUCTION

1.1 Two dimensional nanoplates and layered materials

Two dimensional (2D) materials exist ubiquitously, from kaolinite on earth, to asphalt in crude oil, and to red blood cells in human body.[1-3] The unique geometrical feature of 2D materials sparks great research interest, leading to the development of graphene, MoS_2, black phosphorous and other novel 2D nanostructures.[4-7] In semiconductor field, shape, being a vital parameter, plays a significant role in determining the optical spectra of the nanocrystals as well as microelectronic properties of charge carriers. For instance, from zero-dimensional structures, also known as nanocrystal quantum dots, to one-dimensional nanorods, and to the two-dimensional platelets, the state density of charge carriers vary significantly.[8-10] Therefore, the optical and electronic properties of 2D materials are usually different from their bulk counterparts, due to the synergetic effect of the electron confinements and the absence of interlayer interactions, leading to the variations in the band structures.[11] In colloid science, one of the most striking features of 2D particles lies in the ability to form rich liquid crystalline phases. Studies predicted that 2D platelets can produce lyotropic phases including isotropic (I), nematic (N), columnar (C), and smectic (S) phases. After pioneering works by Lerkerkerker on gibbsite liquid crystals, tremendous efforts have been made on lyotropic discotic liquid crystal, such as graphene oxide, zirconium phosphate, and titanium oxide nanosheets.[12-14]

In addition to the significant advances in LC and electronics, 2D materials show unique advantages for interfacial applications in binary complex fluids, including emulsion surfactant and drug delivery system. The low-dimensional feature of 2D materials, known as arguably the thinnest materials, enables possibly the highest surface area/volume ratio of all known materials. Such distinctive property makes these materials vital for applications demanding high levels of surface/interface interactions on a microscopic scale. Consequently, 2D materials have been developed for use in stabilizing oil-in-water emulsions and regulating drug delivery systems, in which they can interact with large amounts of key molecules, allowing superior control over transport/diffusion kinetics. Owing to their exceptional surface area to volume ratios, the high stabilization of fluid-fluid interfaces can be realized at relatively low concentrations, which is vital for manipulating interfacial properties at high sensitivity levels. Furthermore, the strong anisotropy of 2D materials may change the nature of fluid dynamics and open new research opportunities that allow them to react rapidly to external stimuli or signals, leading to diverse applications in chemical sensors, optical imaging, and high-performance catalyst. These unprecedented properties of 2D materials has led to dozens of 2D nanomaterials being described in the past decade including synthetic zeolite/silicate clays, layered double hydroxides (LDHs), transition metal oxides (TMOs), transition metal dichalcogenides (TMDs), transition metal carbides/nitrides (MXene), black phosphorus (BP), 2D metal-organic frameworks (MOFs), 2D covalent organic frameworks (COFs), and other types of 2D nanomaterials (Figure 1, Adapted with permission with ref. 15. Copyright 2015 John Wiley & Sons, Inc.).[15]

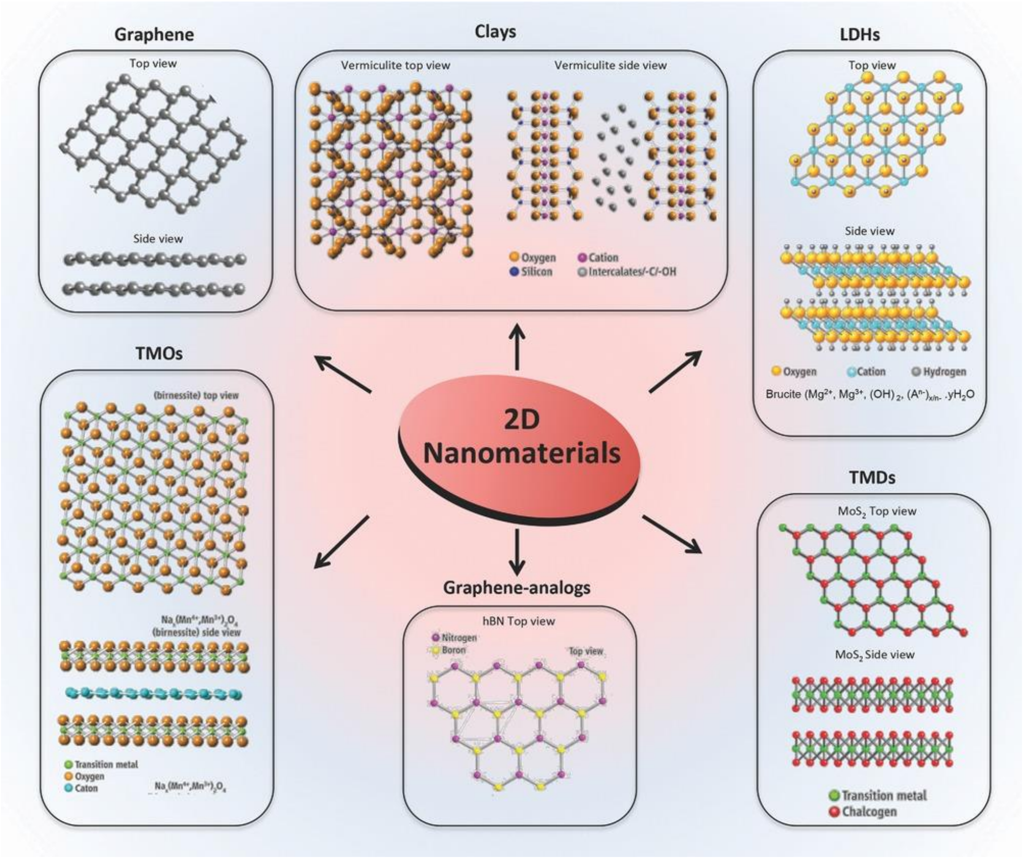

Figure 1. 2D nanoplates.[15] Reprinted with permission from ref. 15.

In this dissertation, nanoscale 2D materials that we developed included graphene quantum dots, ZrP nanosheets, barium ferrite, and kaolinite platelets, featuring the research in optical devices, photonic crystals, and interfacial science. We investigated collective behavior of these nanoplates at multiple length scales: 2D graphene quantum dots (<25 nm), magnetic barium ferrite nanoplatelets (20 to 50 nm), zirconium phosphate monolayers (300 to 1000 nm), and Janus clays (2 to 5 µm). In addition to nanoparticle-based 2D materials, macroscopic 2D membranes will be studied and applied to address the engineering challenges in the fields of complex fluids, e.g. oil/water separation. The proposed research attempts to offer an innovative approach to understand the structures, behaviors, and interactions of 2D materials, allowing applications in diverse fields includes enhanced oil recovery, oil spill mitigation, encapsulation and controlled release. In next section, we will review the common synthetic methods of 2D nanomaterials.

1.2 Synthetic methods

1.2.1 Micromechanical cleavage

The abilities for the synthesis of 2D materials with desired chemical composition, dimensions, crystalline phase, and surface properties are of particular significance. The micromechanical cleavage technique was used to fabricate thin flakes by exfoliation of layered bulk crystals. For example, using mechanical forces with Scotch tape, single/few layers of nanosheets can be achieved as the interlayered van der Waals forces have been overcome in bulk crystals. In 2004, Geim and co-workers first reported the micromechanical cleavage of graphite, where the bulk graphite can be attached to Scotch tapes followed by peeling into thin platelets with another adhesive surface.[16-19] By repeating such process several times, the desired thin flake can be obtained. After attaching freshly cleaved thin films to a flat substrate and removing scope tapes, single- or few-layers of graphene can be acquired.

This micromechanical cleavage technique can be extended to exfoliate other layered materials, including MoS_2, $NbSe_2$, and *h*-BN.[18] Recently, micromechanical cleavage technique has been widely used to cleave various kinds of ultrathin 2D nanomaterials ranging from TMDs, to topological insulator, to BP, and to antimonene. As a general method capable of fabricating all categories of nanosheets of which bulk crystals are layered structures, additional novel ultrathin 2D crystals are expected to be synthesized in this method. This methodology can be considered as a nondestructive process as no chemical reactions were required during the manufacture procedure. Consequently, the exfoliated nanosheets retained the pristine crystal quality of their layered counterparts. The dimensions of the formed 2D structures can reach micrometer levels, which enable the mechanically cleaved nanosheet a persuasive candidate for the researching the intrinsic mechanical, optical, and electronic properties of 2D nanomaterial.

In spite of several advantages of the micromechanical cleavage method, disadvantages still remain: 1) the fabrication yield of this method is relatively low, and impurities such as thick flakes always coexist with the single- or few-layers; 2) The manufacturing speed is not competitive to other methods such as solution-based approaches. The low yield together with the slow manufacturing rate make it problematic to meet the requirements for many practical applications, especially for large-scale manufacture; 3) the dimensions of the prepared 2D materials are hard to be regulated as the exfoliation route lacks the exactness, controllability, or repeatability; 4) Additional substrates are prerequisites to hold the formed 2D crystals during exfoliation, excluding the possibility of fabricating freestanding nanosheets. Recent efforts have been made to micromechanical cleavage method, showing that using oxygen plasma treatment with additional heating during the exfoliation substantially improved the uniformity of interface contact and thus increased the production yield of 2D nanosheets.[20]

1.2.2 Mechanically liquid exfoliation

Sonication has been commonly used as sources of mechanical force for exfoliating layered bulk materials, which are generally dispersed in a particular solvent. As the liquid cavitation was induced by sonication, the waves of mechanical vibrations through the layered crystals produced an intensive tensile stress, resulting in the exfoliation of starting materials into thin sheets.[21] The 2D nanosheets can be separated from the suspension using centrifugation. The key factor for achieving efficient exfoliation of layered bulk crystals is matching the surface energy between the layered bulk crystal and the solvent system. As it is relatively simple and effective without any complicated equipment, this sonication technique offers a new approach for the high-yield/large-scale fabrication of 2D nanosheets. For example, a fairly high concentration of graphene nanosheets suspension was achieved by the sonicating bulk graphite in isopropanol and chloroform.[22-23] In addition to graphene, other 2D nanomaterials, including $NbSe_2$, Bi_2Te_3, and *h*-BN have also been prepared by this technique.[24] The solvents choice and good matching of surface tension between the layered crystals play significant roles in the production of exfoliated nanosheets. It is noteworthy that although pure H_2O was constantly thought to be unsatisfactory for the exfoliation process of layered bulk materials, latest studies on pure water for the sonication-assisted exfoliation method showed that direct exfoliation and dispersion of 2D materials in pure H_2O can be achieved by elevating temperature. The exfoliated nanosheets can be stabilized due to the presence of colloidal surface charges brought by edge functionalization or high polarity, leading to the enhanced colloidal stability of 2D nanosheets. Such approach of exfoliating bulk materials in pure water makes this process promising for practical applications due to environmental friendly and low-cost feature.

It is challenging to find an appropriate solvent for each layered bulk materials, as the surface energy differs in different bulk crystals. Instead, the addition of polymers or surfactants provided another promising way for exfoliating 2D layered materials. The surface energy of the aqueous dispersion can be simply adjusted by introducing suitable surfactants in it, thus reducing the surface energy between layered bulk crystals and solvent and realizing effective exfoliation of layered constituents. For instance, functionalized pyrene derivatives have been reported as dispersants for producing graphene dispersions because of their ability to stabilize graphene at high concentration/dispersant ratios in comparison with traditional surfactants.[25-26] By introducing repulsive solvation and/or electrostatic forces on graphene sheets, pyrene derivatives are able to prevent nanosheet aggregation and thus stabilize graphene in aqueous dispersion.[27-29] In addition to pyrene derivatives, other species have been employed for exfoliating 2D nanosheets in water: polystyrene (PS), polyvinyl chloride (PVC), ethyl cellulose (EC), poly(methyl methacrylate) (PMMA), polyvinylpyrrolidone (PVP) , poly[styrene-*b*-(2-vinylpyridine)] (PS-*b*-P2VP), poly(isoprene-*b*-acrylic acid) (PI-*b*-PAA), P-123-polyoxyethylenes orbitanmonooleate, polyoxyethylene sorbitantrioleate, polyoxyethylene dodecyl ether, polyoxyethylene octadecylether, polyoxyethyleneoctyl phenyl ether, bovine serum albumin (BSA), Pluronic P-123, *n*-dodecyl β-d-maltoside (DBDM), and Arabic gum from acacia tree.[30-33]

Although the sonication-assisted exfoliation method can be applicable for a wide range of 2D materials with higher fabrication rate than that of micromechanical cleavage process, however, its fabrication rate remains relatively low for meeting the requirement for industrial scale. In order to scale up the process, shear force-assisted method was proposed. Using a high-shear rotor-stator mixer, high shear rates in suspension can trigger the exfoliation process and produce the exfoliated nanosheets in a much more efficient manner.[34] The shear-force device contained a mixing head composing of a rotor with a stator, a commercial available setup. Such technique was further extended for exfoliating BP crystal into few-layer platelets. Additionally, the exfoliated *h*-BN, MoS_2, and WS_2 nanosheets were reported by using the kitchen blender. Such results suggest that it is possible to use industrial stirring tank reactors for the large-scale 2D materials manufacture.

1.2.3 Intercalation-assisted liquid exfoliation

As a typical top-down approach, the ion intercalation strategy has been widely adopted for fabrication of ultrathin 2D nanosheets. Small ionic species, including Li^+, Na^+, K^+, can intercalate into the space between adjacent layers in layered bulk crystals, leading to the formation of ion-intercalated compounds. Consequently, the ion intercalation can considerably enlarge the interspacing and decline the van der Waals interaction in layered bulk crystals, facilitating the exfoliation process with short time. High yield of single- or few-layer nanosheets can be obtained after further purification to remove thick flakes via centrifugation. For example, the *n*-butyl lithium was treated with layered materials to formula a Li-intercalated structure in refluxed hexane solution for several days. After moved into water, the nanosheet suspension can be readily formed under sonication.

In spite of the exfoliation facilitated by ion intercalation, however, the intercalation process itself requests extended reaction time (for example, 3 days) and high temperature (for instance, 100 ℃) for some compounds, though some efforts have been made to address those two challenges for bulk TMDs. The lateral dimensions, quantity of deficiencies, sheet number, and concentration of formed nanosheets can be approximately adjusted by changing the tentative settings, such as the starting size of layered crystals, temperature, intercalating agents, and reaction time. One of the unique advantages of the ion-intercalation is that phase alteration occurs from semiconducting hexagonal (2H) and metallic octahedral (1T) phase for MoS_2 and WS_2, presenting a potent method for the phase engineering of 2D TMDs. Despite that metal ions can also be intercalated into layered metal selenide or telluride bulk crystals, ion intercalation remains challenging to be extend to exfoliation of layered metal selenide or telluride as the intercalated products are very sensitive that weaken the stability of bulk crystals of metal selenide or telluride, leading to the decomposition of metal selenide or telluride bulk crystals during the sonication process. Other layered bulk crystals, such as metal oxides, metal hydroxides, MOFs, and COFs.

It is worth noting that organometallic compounds adopted in this technique are extremely explosive and highly sensitive to humidity and oxygen, so the research condition requires to be operated in a glove box with utmost caution. The ion intercalation route is hard to regulate in this technique, making it challenging to circumvent inadequate or over ion-intercalation. Recently, safer salt choices including NaCl and $CuCl_2$ were proposed as intercalates for the exfoliation of graphite powder into graphene. Upon heated at 100 ℃ to vaporize the water, the Na^+ or Cu^{2+} can be intercalated into interlayer spacing of graphite. After sonicated in DMF or NMP for a short time, an up to 65% (1–5 layers) yield of graphene sheets can be prepared with large size up to tens of micrometer.

1.2.4 Ion exchange liquid exfoliation

For the exfoliating many oxygen-containing layered materials including metal hydrogen phosphate, metal oxides, and LDHs, various external ions with large radius can replace the present smaller ions, such as proton, which exist in the layered bulk structure. After such process, the expanded precursors can be simply exfoliated into nanosheets under sonication. As for now, both cations and anions have been reported, leading to ion exchange-assisted exfoliation of various layered materials.

As for cation exchange-assisted liquid exfoliation, a wide range of layered structures have been confirmed to be effortlessly exfoliated into 2D nanosheets including $Zr(HPO_4)_2$, $K_{0.45}MnO_2$, and $KCa_2Nb_3O_{10}$.[35] By just immersing these layered materials in acidic conditions, alkali metal cations will exchange with H^+ cation the interlayer structure, resulting in hydrated protonic compounds, e.g. $H_{0.7}Ti_{1.825}O_4 \cdot H_2O$. Upon further replacing the interlayer protons with tetrabutylammonium hydroxide (TBA^+OH^-; $(C_4H_9)_4N^+OH^-$) via an ion exchange process, the layered bulk materials was portentously enlarged with regard to their d-spacing and straightforwardly exfoliated into 2D nanosheets in aqueous dispersion.

In addition to cations, anions were also proven for exfoliating of layered LDHs via anion exchange-assisted liquid exfoliation technique. layered LDH crystals with a chemical formula of $M^{2+}{}_{1-x}M^{3+}{}_{x}(OH)_2A^{n-}{}_{x/n}\cdot yH_2O$ (M^{2+} = Mg^{2+}, Fe^{2+}, Co^{2+}, Ni^{2+}, Zn^{2+}, etc.; M^{3+}= Al^{3+}, Fe^{3+}, Co^{3+}, etc.; and A = $CO_3{}^{2-}$, Cl^-, $NO_3{}^-$) contain octahedral metal hydroxide layers along with charge-balancing anions (A^{n-}).[36] As the anions in LDH interlayers can be exchanged by other anions to enlarge the d-spacing, amino acids and sodium dodecyl sulfate have been used to demonstrate that ion exchange with existing anions in LDH layered bulk crystals occurs.[37] By sonication or heating treatment in suitable solvents, the ion-exchanged LDH crystals were readily exfoliated into 2D nanosheets in colloidal suspensions.

1.2.5 Oxidation-assisted Liquid Exfoliation

In oxidation-assisted exfoliation of graphite, commonly known as the Hummers' method, strong oxidizing agents, such as potassium permanganate or concentrated nitric acid, were applied to oxidize graphite and oxidation of graphite produces plentiful hydrophilic functional groups on each graphene layer, leading to enlarge the d-spacing of bulk graphite.[38-39] With increasing the treatment time and temperature, the expanded graphite oxides bulk materials were exfoliated into 2D graphene oxide monolayers, and possibly transformed into small-sized 2D graphene quantum dots. This technique enables high yield and large scale of the production of single-layer GO nanosheets in aqueous solution. Although this method is very efficient for producing GO nanosheets, however, further extend of this technique to other layered materials remains highly challenging.

It is noteworthy that the oxygen-containing functional groups of GO nanosheets can be partially eliminated using reduction strategy to form reduced GO nanosheets. Up to now, electrochemical reduction, thermal annealing, photochemical reduction, and chemical reduction were reported to remove oxygen-containing functional groups of GO. Since the residual groups on the surface of rGO nanosheets may still exist, the conductivity of reduced GO commonly cannot compete with graphene nanosheets from CVD method or mechanical exfoliation.

1.2.6 Selective etching

By using bulk MAX phases as the starting materials, the selective etching method can prepare 2D nanosheets of MXenes, a type of early transition metal carbides and/or carbonitrides.[40-41] MAX phases have a general formula of $M_{n+1}AX_n$ (n = 1, 2, or 3), where M, A, and X represent early transition metal, element of group IIIA or IVA, and C and/or N, respectively.[42-44] A clear difference of MAX phase materials from traditional van der Waals layered crystals lies in the metallic bonding between $M_{n+1}X_n$ layers in $M_{n+1}AX_n$ phases which shows much more robust interaction than the van der Waals forces of conventional layered materials including TMDs, graphite, and BP. Therefore, an elective etching technique based on using acidic HF solution to remove the A layers without destroying the bonds in $M_{n+1}X_n$ layers. The resulting etched materials with loosely packed layers were readily exfoliated into 2D nanosheets under sonication. Up to now, this technique has been magnificently useful for synthesizing many different types of MXenes including Al_3C_3, Ta_4C_3, Mo_2TiC_2, Nb_2C, Ti_4N_3, $Mo_2Ti_2C_3$, Ti_3CN, Mo_2CT_x, Cr_2TiC_2,Ti_2C, V_2C, $(Ti_{0.5},Nb_{0.5})_2C$, and $(V_{0.5},Cr_{0.5})_3C_2$. However, several limitations still exist in this technique as it is tough to apply this process to prepare other ultrathin 2D nanosheets, such as TMDs.

1.2.7 Chemical vapor deposition

In semiconductor industry, CVD technique has been extensively used for the massive production of high quality thin films of Si, SiO_2, metal plug and etc. In the meantime, extensive efforts have been made in developing CVD process as a consistent and influential method for manufacturing a huge number of 2D nanomaterials.[11] In a classic procedure, one or several gas precursors are introduced on the surface of a substrate in an oven chamber, where the gas species can react and/or deposit single to few layers of ultrathin 2D nanosheets on the surface of substrates. In some case, catalysts, such as transition metal salt, were used to promote such thin-film reaction process.

From the perspective of reaction kinetics, the CVD technique utilizes gaseous phase of precursors to react, transport, and deposit thin films of a great variety of materials.[45] The basic steps includes 1) molecular transfer, 2) adsorption on substrate 3) reaction, 4) nucleation, and 4) growth. There has been significant development of CVD-based depositions including more than 12 sub-techniques such as PECVD, LPCVD, ALD, etc., enabling the deposition almost any type of material: metals, insulator and semiconductors. By varying the growth parameters such as temperature, pressure, stream rate of carrier gas, concentrations of source materials, and the distance substrate and source, we can precisely control and engineer the film size, morphology, layers, orientation, and any dopants or defects in it. In addition to conventional CVD approaches to grow polysilicon electrodes, tungsten plug, and diamond film, modified CVD methods have been developed to grow large area and high quality 2D materials. For example, Wu et al. developed a local feed method by supplying the source gas to a single point with a small area in the CVD furnace to create only one nucleus, which later grew into an inch size single crystal graphene domain. Lately, modifications of CVD methods have been explored to formulate heterostructures of 2D materials, expanding the family of 2D materials. In addition, theoretical development of 2D material growth can advance the CVD method itself. In this regard, the development of CVD methods and 2D material growth may together promote the rapid development of research into 2D materials and accelerate their wide use with the availability of large-scale and high quality CVD-grown samples. Such vapor phase based direct growth strategy allows a scalable and well-regulated approach to develop high-quality and large-range 2D constituents with a practical price. These benefits mark CVD a crucial methodology for fundamental study as well as advanced applications of 2D materials.

1.2.8 Hydrothermal/Solvothermal synthesis

As a representative wet-chemical synthesis approach, the hydrothermal/solvothermal synthesis involves water or other solvents in a closed vessel, where reaction temperature is commonly higher than the boiling point of the solvent that generated high pressure to promote the reaction kinetics and increase the quality of crystal phase of as-prepared 2D nanomaterials. Remarkably, the solvent and additives, such as ligands or surfactants, are crucial factors in determining the synthesis, morphology, and properties of 2D nanosheets. For example, ultrathin cobalt nanosheets with tunable oxide state can be prepared by using hydrothermal condition of butylamine and dimethylformamide.[46] Single-layer noble metal nanosheets with size of few hundred nanometers can be prepared using PVP as surfactants. Besides metal nanosheets, metal oxides and TMDs nanosheets have also been produced by this hydrothermal/solvothermal technique.

As a simple and possibly scalable technique for the production of 2D nanomaterials, however, it is difficult to understand fully the mechanism details in every single reaction as all the reaction kinetics occurs in a sealed system, which make it challenging to apply the same experimental condition to other 2D material systems. Noteworthy, the hydrothermal/solvothermal synthesis is relatively sensitive to the experimental settings, which increase the challenge of precisely controlling the resulting 2D nanomaterials in different batches or different laboratories.

1.2.9 Oriented attachment method

Unlike the traditional mechanism, the oriented attachment method demonstrates an unusual growth progression and realizes nanostructures with well-defined shapes.[47] During this process, neighboring nanocrystals are attached and fused with each other, forming single-crystalline 2D sheets via involving a common phase facet due to the high interfacial energy facets. By applying close packing of oleic acid ligands on {100}, PbS nanocrystals can grow into single-crystalline 2D sheets. Studies also showed that other reagents, such as chlorine-containing reactants, can assist in activating the oriented attachment progression by uncovering the highly reactive {110} facets. In general, the growing mechanism is based on oriented attachment of small crystals, after which epitaxial recrystallization into large 2D nanostructures occurs.

Similar to the ligand attachment method, other templated strategies have been investigated for growing anisotropic nanostructures. For example, the hexagonal close-packed (*hcp*) gold nanosheets can be prepared by using the GO as a starting template. In addition, CuO nanoplates were also report for templated synthesis of α-Fe_2O_3 nanosheets, in which the CuO template was etched away during the nanosheet growth. Numerous 2D semiconductor nanosheets, including $CuInS_2$, $CuIn_xGa_{1-x}S_2$, and Cu_2ZnSnS_4, have also been fabricated by the 2D-templated production process.

1.2.10 Self-assembly of building blocks

Driven by the improvement of nanocrystal production, self-assembly of small building blocks has been developed to breed architectures with building blocks of nanocrystals in an orientationally/positionally ordered manner, in which presynthesized building blocks instinctively organize with each other by physical/chemical interactions including electrostatic interactions, van der Waals interactions, and hydrogen bonds.[48] Both nanoparticles and nanowires were shown to self-assemble into 2D materials, such as polycrystalline 2D CdTe nanosheet or the assembled Au nanosheets.

In addition to nanocrystals, organic molecules can also be used as building blocks for self-assembling into 2D materials by electrostatic interactions, van der Waals interactions, and hydrogen bonds. Well-organized photonic nanosheets were demonstrated by self-assembly of nonionic surfactant hexadecylglyceryl maleate.[49] It is reasonable to expect that more novel 2D materials would be developed via self-assembly of building blocks strategy.

1.2.11 Hot-injection method

The hot-injection method involves the fast addition of the extremely reactive starting materials into a warm solution comprising long-chain fatty acid or fatty amine surfactants, leading to the system reaching a high initial supersaturation. Such method was useful to produce monodispersed colloidal 2D metal chalcogenide nanostructures with uniform size and/or shape. For example, by heating the starting materials of $CdCl_2$ dispersed in octylamine and oleylamine, the hot injection of the above mixture in to and Se powder allowed the formation of single-crystalline 2D CdSe nanosheets with defined shape and thickness.[50] Note that the production of single-layer 2D nanosheets of layered metal chalcogenides can also be realized by this technique.

1.2.12 Other synthetic methods

Other synthetic approaches have also been established to manufacture 2D nanomaterials. For example, a strategy based on surface synthesis has been advanced for synthesizing COF nanosheets from starting materials on clean substrates.[51] Upon the surface of a specific substrate, the monomers were applied and reacted into 2D nanosheets of COF by the polymerization because of surface confinement effect. Remarkably, highly oriented pyrolytic graphite can also be used as the substrate to grow COF nanosheets of which the benzene-1, 3, 5-tricarbaldehyde react with aromatic diamide under heating condition. It is worth noting that the diffusion of monomers for bulky surface exposure and the monomer reaction were facilitated to produce single-layer COF. However, disadvantages still exist in this technique as the strict requirement of monomers which may limit the choice of 2D materials that can be synthesized via this method. It was also reported that the surface confinement of NaCl can also facilitate the growth of 2D materials. By confining ligand reaction at the water/air interfaces, other interface-mediated production technique is also employed for the synthesizing 2D nanomaterials, particularly useful for building up metal coordination polymers (CPs).[52-53]

1.3 Examples of 2D materials in this study

1.3.1 Graphene and graphene quantum dots

Graphene is a single to few layered graphite with 2D hexagonal-close-packed carbon network. As a prominent type of 2D materials, graphene received great research interest due to its exceptional mechanical and electronical properties.[54-55] In the field of complex fluids, surface-modified graphene oxide was reported as a particle surfactant due to its amphiphilicity, allowing strong adsorption to the oil–water interface.[56] However, the production of submicron emulsions from large-size graphene oxide surfactants remains highly challenging because of the curvature effect caused by their large dimension, which can be avoided by the small nanoparticle surfactants.[57]

Recently, graphene-based semiconductor nanoparticles, i.e. carbon quantum dots (CDs) and graphene quantum dots (GQDs), have fascinated substantial research attention as new types of luminescent NPs (Figure 2). They are mono- or few-layered graphene sheets with lateral dimensions smaller than 100 nm, though GQDs are of higher crystallinity.[58] Such quantum dots possess unique properties, such as high photoluminescent quantum yield, cost effectiveness, low cytotoxicity, and biocompatibility.[59-63] Therefore, they have been investigated extensively for applications such as bioimaging,[59, 64] solar cells,[60, 65] and surfactants.[57, 66-67] Experimentally, by carefully controlling surface chemistry and structure, GQDs have been fabricated by chemical oxidation of carbon black,[68] solvothermal cleaving of graphene oxides,[69] electrochemical exfoliation of graphite,[70] thermal degradation of organic molecules,[71-72] ruthenium-catalyzed decomposition of C_{60}[73] and stepwise organic synthesis.[74-75]

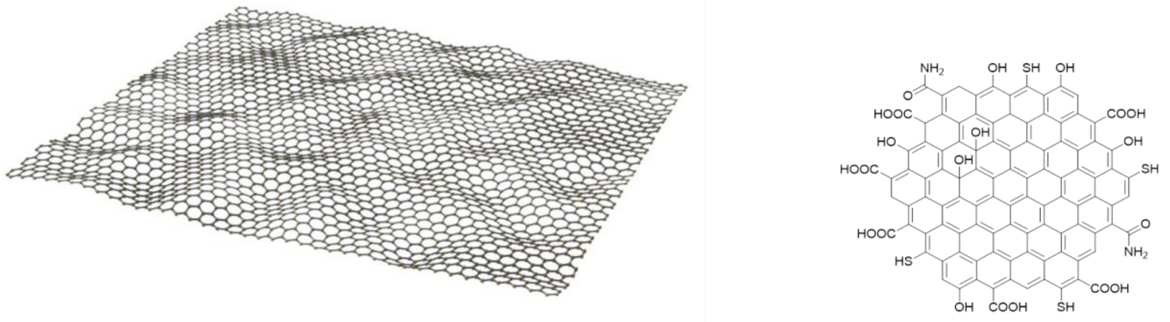

Graphene (10^2 to 10^3 nm)

Graphene Quantum Dots
(5 - 50 nm)

Figure 2. The schematic illustration of graphene and 2D GQDs

In addition, great promise as efficient surfactants in stabilizing oil-water interfaces was expected for GQDs if their surface properties can be precisely engineered. In particular, the efficiency of GQDs as surfactants can be greatly amplified due to their nanosized dimensions and high surface-to-volume ratio. Despite huge potentials of GQDs as particle surfactants, however, very limited works were reported probably due to the struggle of achieving desired surface properties. The surface of the GQDs is dominated by their large portion of hydrophilic edges which result in undesired interfacial property. A possible solution toward such challenge could be design of hydrophobic species that can modify the GQD surface in a controllable manner.

1.3.2 Zirconium hydrogenphosphate (ZrP)

The bulk ZrP has a layered crystal structure with water molecular intercalation in chemical formula of $Zr(HPO_4)_2 \cdot H_2O$. Due to the acidic hydroxyl group –OH, the bulk ZrP can be readily intercalated and exfoliated into monolayer by using exfoliation agents, such as tetramethylammonium hydroxide (TMAOH) or tetrabutylammonium hydroxide (TBAOH). The exfoliated ZrP shows a 2D shape with strongly anisotropic feature, i.e. high aspect ratio of diameter over thickness. Such 2D material offers a great platform to study lyotropic liquid crystal suspension via the charge platelet interaction.

1.3.3 Two-dimensional clay

Natural clays, such as kaolinite and montmorillonite, are layered silicate mineral with 2D structure. The OH groups on clay surface enable facile functionalization using reagents such as silanes, phosphonic acids, and dopamine (Figure 3). As natural clay platelets are abundant and cheap starting material, this may allow the application of nanotechnology in an affordable price, which is crucial for practical application of 2D material in large scale.

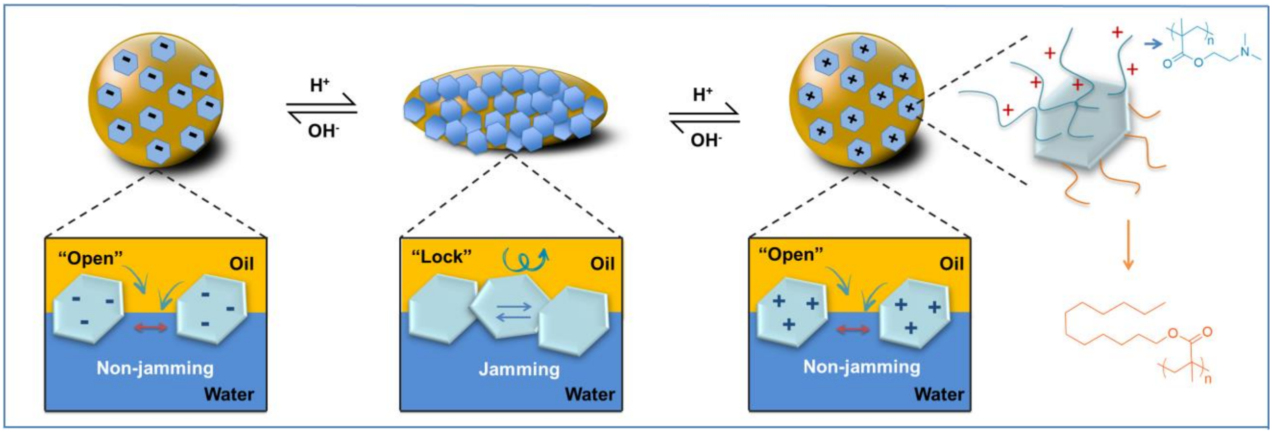

Figure 3. The schematic illustration of polymer-grafted clays as nanogates.

1.3.4 Barium ferrite (BF)

As the few examples of 2D magnetic nanoparticles, barium ferrite (BF) has drawn significant research interest in recent years.[76] As a widely used permanent-magnet material with the chemical formula $BaFe_{12}O_{19}$, BF has been extensively studied for application including high-density magnetic recording, microwave radiation absorber, and magnetic microwave devices. As a striking example of advancing cancer therapies, the magnetic nanodiscs will create an oscillation transmitting a mechanical force to the cell and so destroying it in vivo upon an alternating magnetic field.[77]

The incorporation of magnetic character in 2D nanomaterials may enable unique advantage of facile separation and recovery, facilitating the practical applications of 2D nanoparticles. In addition, the size of BF particle normally is in a range of 10 to 50 nm, which is a perfect candidate to investigate the diffusion behaviour under strong Brownian motions.

1.3.5 Two-dimensional membranes

As an example of 2D materials in macroscopic level, 2D membranes show unique advantages in separation science, such as liquid-liquid separation. By engineering the surface of 2D membrane, the materials demonstrate on-demand separation of oil-water mixture with high efficiency. In fact, the challenge of oil-water separation has already highlighted due to the recent oil spills and oil contaminated water from petrochemical industry.

For example, polycyclic aromatic hydrocarbons and other oily chemicals in wastewater pose a potential risk to aquatic ecosystems as their decomposition causes excessive oxygen consumption, which leads to an increased mortality rate in fish populations.[78] However, conventional oil-water separation methods, including gravity separation, air flotation, coagulation, and de-emulsification, have inherent disadvantages such as low efficiency, high energy consumption, and recontamination problems.[79-82] Separation of oil and water is essentially an interfacial science problem, and thus new strategies based on unique wettability materials have shown to be effective and advantageous (Figure 4).[83-84] This can be of great importance for application in diverse fields including wastewater treatment, fuel purification, and the cleanup of oil spills.

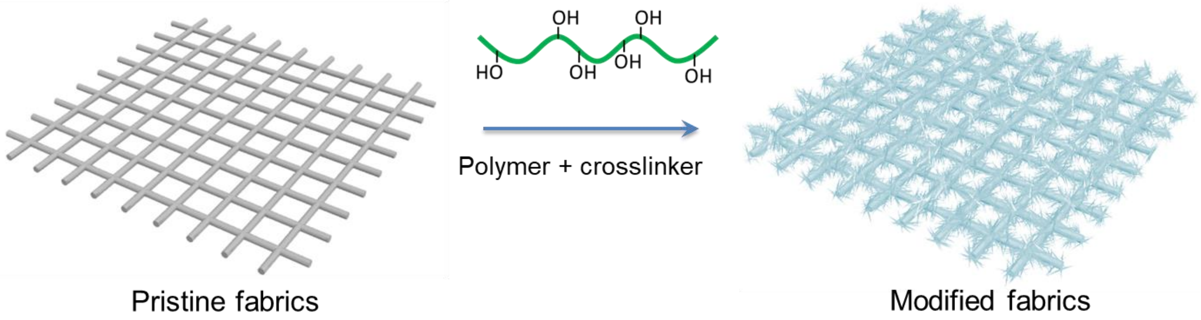

Figure 4. The schematic illustration of the surface modification of 2D membranes.

CHAPTER II

SURFACE-ACTIVE GRAPHENE NANOPLATELETS

2.1 Surface-active GQD for stabilizing liquid-liquid interfaces

2.1.1 Background

In Pickering emulsions, the solid particles play a key role at the interface of two immiscible phases to prevent the coalescence by generating a mechanically robust monolayer.**[85]** This field received widespread scientific interests on developing stable Pickering emulsions/foams,[86-88] double emulsions,[89-92] liquid marbles and superhydrophobic barriers.[93-94] As nano-manufacturing processes are getting mature and well-controlled, more and more nano-materials are adopted as the stabilizers for Pickering emulsions, such as functionalized silica, titania nanoparticles, zirconium phosphate, protein microgel, clay and polymer particles.[57, 95-104] However, most procedures are still relatively complicated and require costly reagents for synthesizing the amphiphilic nanoparticles with desired properties, resulting in limited applications.

Carbon-based nanoparticles have attracted much attention in past decades owing to their low cytotoxicity, chemical inertness, cost effectiveness, and biocompatibility.[58, 70-71, 105-108] Because it is also difficult to obtain the desired surface properties, there were only few works reporting graphene-based materials as surfactants.[56-57] Recently, Zhang *et al.* demonstrated that graphene oxide (GO) nanosheets were utilized in Pickering emulsion polymerization to form GO

Parts of this section are reprinted with the permission from ACS publishing (1) Zeng, M.; Shah, S. A.; Huang, D.; Parviz, D.; Yu, Y.-H.; Wang, X.; Green, M. J.; Cheng, Z., Aqueous exfoliation of graphite into graphene assisted by sulfonyl graphene quantum dots for photonic crystal applications *ACS Applied Materials & Interfaces* 2017, 9 (36), 30797-30804; Copyright (2017) American Chemical Society; and Hindawi (2) Zeng, M.; Wang, X.; Yu, Y.-H.; Zhang, L.; Shafi, W.; Huang, X.; Cheng, Z., The Synthesis of Amphiphilic Luminescent Graphene Quantum Dot and Its Application in Mini-Emulsion Polymerization *Journal of Nanomaterials*, **2016**, 1(1).

coated polystyrene (PS) microspheres with a narrow range of size distribution.[109] Although pristine GO nanosheets could not stabilize the styrene droplets in aqueous phase due to high hydrophilicity of GO, the hydrophobic modification by adsorbing PS oligomers on GO surface led to the nascent nuclei formation and continuous Pickering emulsion polymerization successfully. In 2014, Kim *et al.* reported a top-down method for synthesizing graphene quantum dots (GQDs) as surfactants.[57] Pristine GQDs (p-GQDs) were first studied, and showed poor emulsification performance. By thermally reducing the oxygen-containing groups on p-GQDs, the hydrophobicity was improved and further enabled the reduced GQDs (r-GQDs) serve as the interface stabilizer in toluene-in-water emulsions. However, due to the limited hydrophobicity introduced by thermal reduction, the average size of Pickering emulsions stabilized by r-GQDs were relatively large, and the size distribution of PS colloidal particles was much broader than that of PS colloidal particles stabilized by organic/polymer surfactant.[110] Therefore, it is desirable to develop a highly efficient particle surfactant by controlling the wettability of the amphiphilic GQDs.

An alternative method to improve hydrophobicity of nanoparticles can be achieved by introducing hydrophobic functional groups, such as alkane chain. In this study, we developed a facile bottom-up approach to synthesize octadecyl grafted luminescent graphene quantum dots (C_{18}-GQDs) surfactant with a controllable wettability. The oleophilicity and hydrophilicity of C_{18}-GQDs were balanced by controlling the chemical condensation of hydrophobic alkane chain. As a novel class of efficient particle stabilizers for Pickering emulsions, C_{18}-GQDs were demonstrated the ability of stabilizing dodecane-in-water emulsions and were employed to produce PS/GQDs microspheres via mini-emulsion polymerization of styrene. The pristine graphene quantum dots (p-GQDs) were also synthesized without octadecyl group grafting for comparison.

2.1.2 Synthesis of amphiphilic GQD

Figure 5 shows the schematic illustration of C_{18}-GQDs synthesis. First, the 1.0 g of citric acid monohydrate (4.8 mmol) was dissolved in 25 mL of ethanol, and then followed by adding an ethanol solution containing 0.75 g of octadecylamine (2.8 mmol). The mixture was stirred for 1 hour, and the formed precipitate was filtered, washed with ethanol several times. After dried in an oven at 65°C for 24 hours, the white solid product was mixed with 0.3g of glycine (4.0 mmol), and then transferred into a 20-ml glass vial and calcinated in air at 200°C for 3 h. The dark solid residue was further purified by column chromatography to remove unreacted starting materials for obtaining C_{18}-GQDs. For comparison, hydrophilic p-GQDs were prepared by a previous work.[71] Specifically, the citric acid was heated in a 20-ml glass vial in air at 200°C without the addition of octadecylamine as comparison.

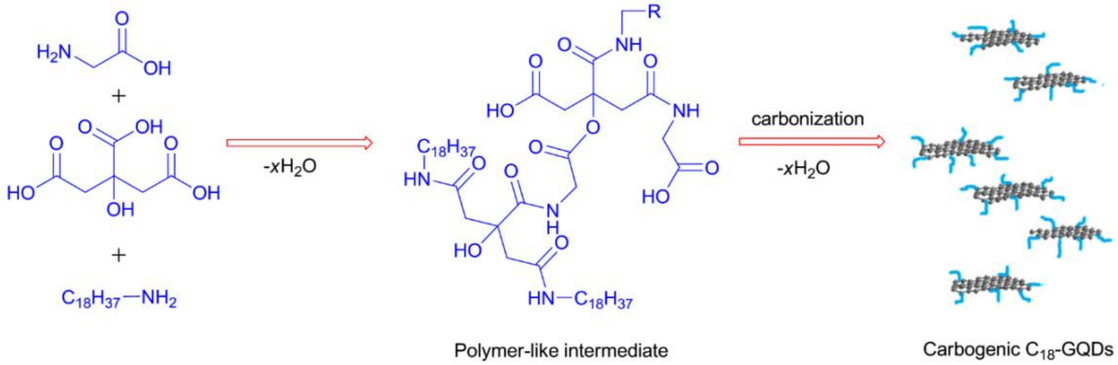

Figure 5. The schematic illustration of the formation of C_{18}-GQDs.

Homogeneous C_{18}-GQDs films were prepared by coating a few drops of C_{18}-GQDs dispersion (0.18 wt%) onto pre-cleaned glass plates, drying in air at 70 °C for 4 h. After cooled down to room temperature, one drop of deionized water was placed onto the surface and allowed to equilibrate for 20 s before making any measurement. Homogeneous p-GQDs films were prepared by the same procedure. A digital camera was used to record the images and their contact angles were calculated by *PolyPro* software package.

To prepare aqueous dispersion, the purified graphene quantum dots were dissolved in 1 ml acetone followed by 20 ml deionized water. Then, the acetone was removed at 65°C under a reduced pressure. Finally, the C_{18}-GQDs dispersion was centrifuged for 20 minutes at 4000 rpm to remove possible aggregates. Part of final dispersion was taken out to determine concentration by drying at 75 ℃ in an oven for 2 days. For Pickering emulsion formation, C_{18}-GQDs and p-GQDs dispersions with the designed weight percentages were brought into a glass vial, and then dodecane was slowly added into the dispersion under sonication for 2 minutes.

First prepare 0.9 ml C_{18}-GQDs aqueous solution (0.18 wt%) in a 5-ml glass vial, and 0.1 ml styrene and 2 mg azobisisobutyronitrile (AIBN) were then introduced. This mixture was manually shaken for 30 seconds. Finally, the entire suspension of C_{18}-GQDs/PS precursor was transferred into a 70 ℃ oven for 4 hours, allowing for the full polymerization of styrene. The products were washed with warm DI water (50 ℃) for twice and then dried using a freezing dry machine.

The morphologies of C_{18}-GQDs and C_{18}-GQDs/PS composites were characterized by a transmission electron microscopy (TEM, JEM-2010, JEOL) operated at an accelerating voltage of 200 kV and a field emission scanning electron microscopy (FE-SEM, Quanta 600, FEI). The particle-size distribution of C_{18}-GQDs Pickering emulsion droplets was determined by dynamic light scattering (DLS, Zetasizer Nano ZS90, Malvern Instrument).

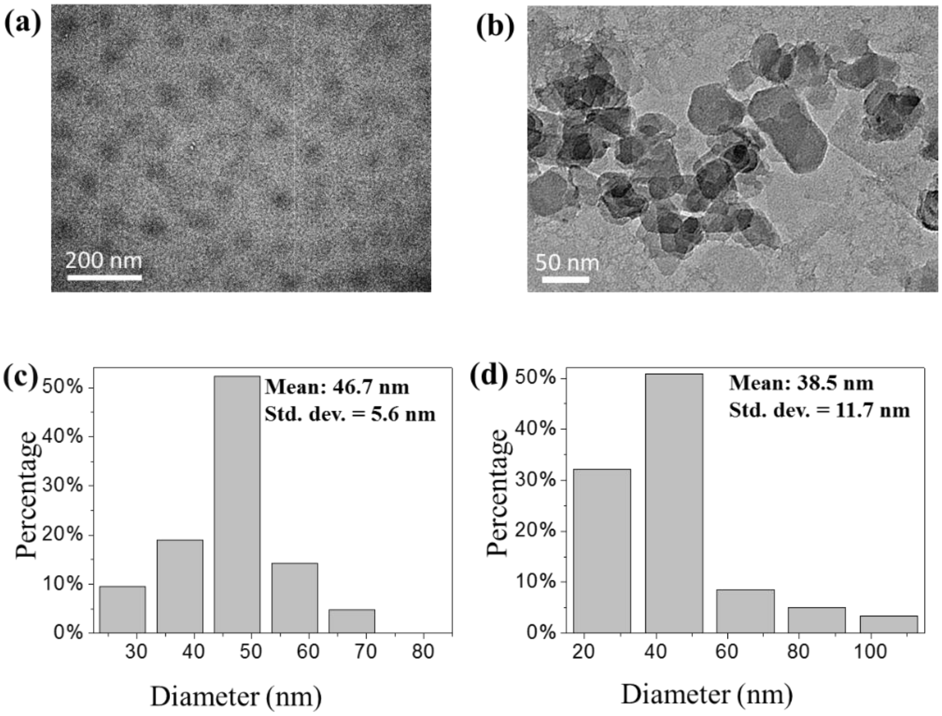

Figure 6. TEM images and size distribution histograms of GQDs.

2.1.3 Surface chemistry of GQD

Graphene quantum dots are commonly considered as mono- or few layered graphene sheets or poly-aromatic species with lateral dimensions in the range of 1–100 nm [59]. TEM images of C_{18}-GQDs were taken to verify their morphologies. In Figure 6, C_{18}-GQDs showed an average size of 46.7±5.6 nm, which resembled the results reported previously [58, 61, 111]. Comparing with p-GQDs, the low resolution/contrast of TEM image of C_{18}-GQDs might be due to the functionalization of edge of graphene sheets, which were also observed in other polymer functionalized GQDs.[58, 112]

Size distributions of GQDs were performed by analysis of TEM images, counting at least 100 particles. The size distribution of as-prepared C_{18}-GQDs was relatively narrow, suggesting a uniform arrangement. The morphologies of p-GQDs were also studied by TEM. The average size of p-GQDs was 38.5 nm with standard deviation of 11.7 nm, indicating that the average sizes of C_{18}-GQDs and p-GQDs were similar. The C_{18}-GQDs were found to be well dispersed in organic solvents such as acetone and toluene, but had only limited solubility in water, which indicated a successful grafting of organophilic groups on graphene nanoplatelets.[112] In contrast, p-GQDs behaved more like graphene oxide and were well-dispersed in the water due to the existence of hydrophilic carboxylic group (-COOH**).**[71]

The surface chemistry of C_{18}-GQDs was further confirmed by Fourier transform infrared spectroscopy (FTIR). In Figure 7, the characteristic vibrational bands at 1090, 1370, 1710, 2920, and 3380 cm^{-1} were found, which can be assigned to the stretching vibrations of C-N/C-O, vibrational band of carboxylate ion ($-COO^{-}$), the overlapped vibrational absorption bands of C=C and HN–(C=O)–R, the C–H stretching vibration, and the stretching vibrations of C-OH and N-H. These results indicated that the hydrophobic groups (i.e., alkyl groups) were functionalized by amide bonds.[113-115]

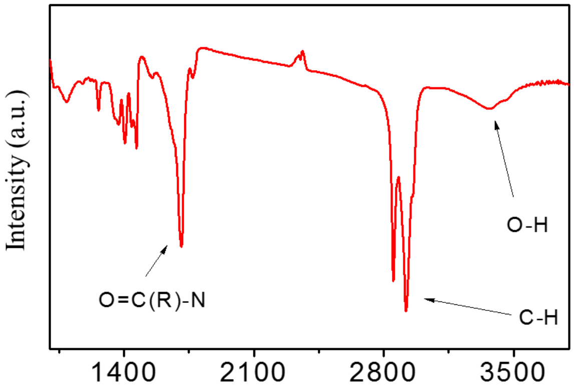

Figure 7. FT-IR spectrum of C_{18}-GQDs.

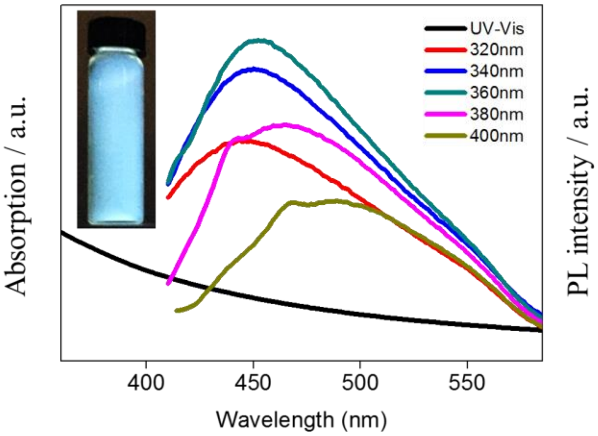

Figure 8. UV-Vis and PL spectra of C_{18}-GQDs. Inset: C_{18}-GQDs under UV light.

In order to further prove the successful synthesis of graphene quantum dots, the optical properties of C_{18}-GQDs were examined by the ultraviolet-visible spectrophotometry (UV-Vis) and photoluminescence (PL) spectra at variable excitation wavelengths, as shown in Figure 8. The UV-vis absorption spectrum of C_{18}-GQDs was generally broad in the range from 350 nm to 600 nm. In the Figure 8 inset, a bright blue luminescence light was observed at a low concentration (0.5 mg/ml) under the illumination of a UV (λ = 365nm). The PL spectra of C_{18}-GQDs were also broad and apparently dependent on the excitation wavelength. The PL peaks shifted to longer wavelengths as excitation wavelength increased from 320 to 400 nm. In particular, C_{18}-GQDs showed strong blue photoluminescence, and had optimal excitation and emission wavelengths at 360 nm and 450 nm, respectively. Although the mechanisms underlying the PL properties of graphene quantum dots have not been completely understood yet, some theoretical modelling and calculations gave good insights on understanding PL mechanism of GQDs. For instance, by employing density-functional theory (DFT) and time-dependent DFT calculations, Sk. *et al.* recently demonstrated that PL of a GQD could be essentially originated from the quantum confinement of conjugated π-electrons in sp^2 carbon grid, and can be tuned by its size, shape, edge configuration, attached chemical functionalities, and heteroatom doping and defects.[116]

2.1.4 GQD at interfaces

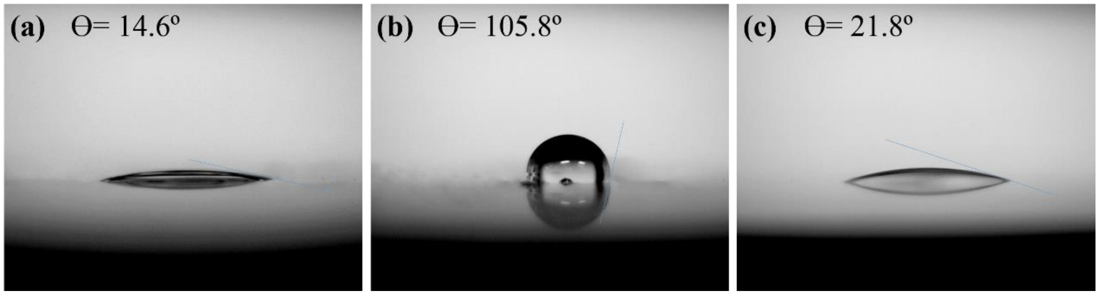

Figure 9. Contact angles of (a) p-GQDs, (b) C_{18}-GQDs and (c) bare substrate.

The wettability of C_{18}-GQDs was determined by measuring contact angles at water-air interface. As shown in Figure 9, the contact angle for p-GQDs is 14.6 °, indicating the high hydrophilicity due to the existence of hydrophilic carboxylic group.[71] By contrast, the contact angle of 105.8 ° for C_{18}-GQDs is significantly larger than p-GQDs as well as 21.8 ° on glass substrates, proving that functionalization of graphene quantum dots with octadecyl group introduces substantial hydrophobicity. The effective improvement of surface amphiphilicity suggested that C_{18}-GQDs is expected to be an attractive candidate for stabilizing Pickering emulsions in comparison with highly hydrophilic p-GQDs.

To examine the potential of the hydrophobic octadecyl grafted GQDs as the surfactant during emulsification, both p-GQDs and C_{18}-GQDs were used to prepare Pickering emulsions. At the relatively low concentration (0.1 wt%), p-GQDs were observed to have rarely emulsified the dodecane-in-water droplets (Figure 10), while the dodecane/water mixture in the presence of C_{18}-GQDs formed a uniform emulsion that was similar to emulsions produced by amphiphilic polymer-based surfactants.[110] The poor emulsification efficiency of p-GQDs indicated its overwhelming hydrophilicity, because the as-prepared p-GQDs contained a huge amount of oxygen-containing groups, including C–OH groups and -COOH groups.[58, 71] Thus, p-GQDs preferentially stayed in the aqueous medium. The introduction of octadecyl group on GQDs, however, induced a significant increase in the hydrophobicity and oleophilicity of the graphene quantum dots. The hydrophobic octadecyl group allowed GQDs to be strongly absorbed at the interface of water/dodecane, leading to a remarkable improvement in the emulsification efficiency. Moreover, as an effective means for estimating the emulsion stability and the emulsification effect,[117] the droplet size distribution of the Pickering emulsions stabilized by C_{18}-GQDs were studied by DLS, as showed in Figure 10. The average droplet size for dodecane-in-water emulsions was 263 nm, with standard deviation of 51 nm. Microscopic study of Pickering emulsion droplets was also performed, suggesting uniform Pickering emulsion droplets. However, well-focused microscopic images were difficult to obtain because the Pickering emulsion size fall into the range of visible light wavelength, as shown in Figure 10.

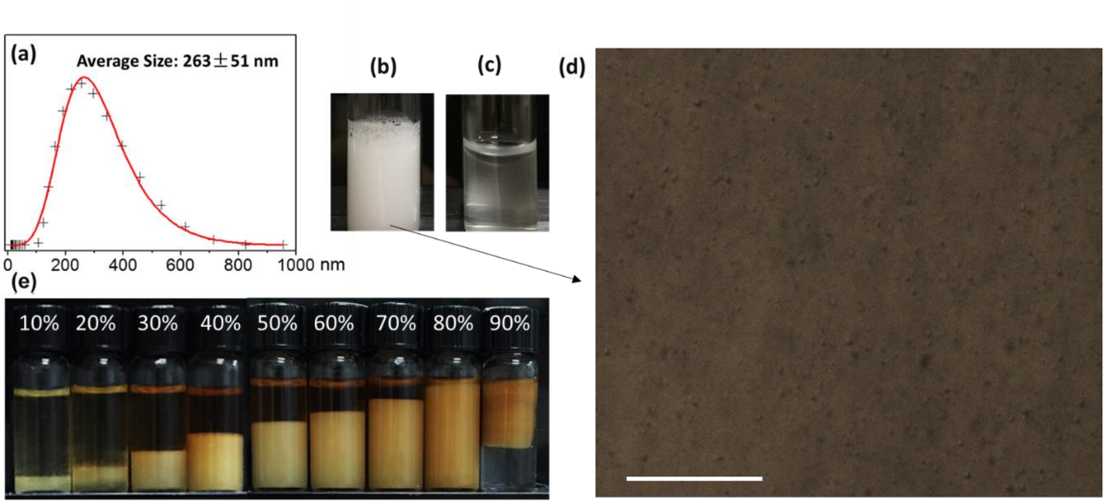

Figure 10. Emulsions stabilized by C_{18}-GQDs.

Figure 10 shows the observations of oil-in-water emulsions preferentially formed when C_{18}-GQDs were introduced into system at a relatively high concentration (2.0 wt%).[98, 118] The emulsion types (oil-in-water and water-in-oil) were examined qualitatively by checking their miscibility in the water or oil phase.[98] That is, a drop of each emulsion was added to pure dodecane or to deionized water. In water, the oil-in-water emulsions dispersed, but remained as drops in dodecane, and vice versa. As shown in Figure 10, the dodecane phase showed a dark brownish color due to the good solubility of C_{18}-GQDs in dodecane. Besides, oil-in-water emulsions (Winsor I type) were preferred to be formed when dodecane volume fraction was higher than 20%. However, phase inversion occurred if oil volume fraction was low according to phase diagram.[98, 118]

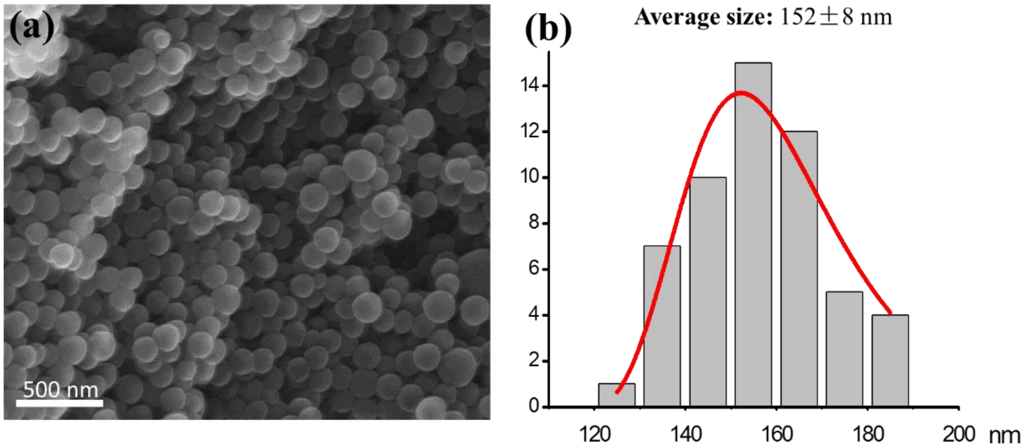

Figure 11. SEM image of uniform PS particles stabilized by C_{18}-GQDs.

To further demonstrate the potential of C_{18}-GQDs as a surfactant, C_{18}-GQDs were employed to produce polymeric nanocapsules through miniemulsion polymerization method. Up to date, predominantly the formation of polymeric capsules with a size of 1 μm and larger is demonstrated by Pickering polymerization. However, for many practical uses, especially in medicine and high-resolution electronic inks, smaller capsules with size between 50 and 300 nm are of high interest.[119] To achieve a successful miniemulsion polymerization, the emulsion surface is required to be stabilized by adsorption of surfactants. By using C_{18}-GQDs as a surfactant and AIBN as an initiator, styrene was successfully emulsified and polymerized to fabricate the uniform C_{18}-GQDs/PS microspheres, as shown in Figure 11. It was shown that the size of small microspheres was comparable to that of “thermodynamically” stable Pickering emulsions prepared by mechanical stirring of 3-methacryloxypropyl trimethoxysilane/H_2O mixture with magnetite nanoparticles.[97] An average size of the PS nanoparticles was determined to be 152 ± 8 nm, which was smaller than that of previously reported PS colloidal particles stabilized by graphene-based materials.[56-57, 109, 120-125] In addition, the morphologies of C_{18}-GQDs/PS composites are similar to that of PS nanoparticles produced by commercial surfactants.[110] These results render that C_{18}-GQDs is a promising candidate for a highly efficient surfactant forming oil-in-water Pickering emulsions. Further research is still needed, however, to address issues such as how to utilize photoluminescent properties and how to optimize the surface chemistry of functionalized graphene quantum dots.

2.1.5. Conclusions

In summary, we demonstrated that octadecyl grafted graphene quantum dots (C_{18}-GQDs) surfactants could be used as effective emulsifiers for stabilizing Picking emulsions as well as for mini-emulsion polymerization. Both the photoluminescent and excitation-dependent properties were characterized. Furthermore, by using functionalized graphene quantum dots, uniform Pickering emulsions of dodecane and water were formed with an average size of 263 ± 51 nm; in contrast, no stable Pickering emulsions were produced with solely addition of nonfunctionalized p-GQDs. Phase diagram of C_{18}-GQDs further confirmed the well-balanced amphiphilic property and suggested that water-in-oil emulsions could be created by C_{18}-GQDs. Moreover, C_{18}-GQDs exhibited the high efficiency as surfactants to synthesize uniform C_{18}-GQDs/PS nanocapsules via the mini-emulsion polymerization. In presence of C_{18}-GQDs, polymeric nanocapsules with an average size of 152 ± 8 nm were achieved. This facile one-pot bottom-up synthesis of amphiphilic GQDs combined with their luminescent property provides a possible direction for multifunctional carbon-based quantum dots.

2.2. Surface-active GQD for stabilizing solid-liquid interfaces

2.2.1 Background

In addition to its exceptional thermal and mechanical properties, graphene possesses a large delocalized π-electron system which results in a strong affinity for polyaromatic hydrocarbons (PAHs), which are widely present in dyes, pollutants, and biomolecules.[54-55] Owing to their tendency to interact with PAHs, graphene and its derivatives have been studied extensively as sorbents for wastewater treatment applications.[126-127] Functionalized pyrene derivatives have been reported as dispersants for producing graphene dispersions because of their ability to stabilize graphene at high concentration/dispersant ratios in comparison with traditional surfactants.[25-26] By introducing repulsive solvation and/or electrostatic forces on graphene sheets, pyrene derivatives are able to prevent nanosheet aggregation and thus stabilize graphene in aqueous dispersion.[27-29] Such dispersions with high colloidal stability may be used for direct inkjet printing of electronic structures.[128] Additionally, the ability of PAHs to form charged graphene species may allow for additional assembly techniques such as layer-by-layer film growth.[129]

The type and number of functional groups can play an important role in determining the quantity and quality of graphene dispersions prepared using pyrene derivatives. Theoretical simulations suggest that a higher dispersant polarity can facilitate exfoliation of graphite by accelerating “sliding” of the dispersant into the graphite interlayer.[130] Experimentally, the exfoliation efficiencies of pyrene derivatives with amino groups (-NH_2), carboxylic groups (-

COOH) and sulfonic groups (-SO_3H) were investigated under various pH values and processing conditions.[27] It was shown that functional groups with higher electronegativity were more efficient in enhancing the adsorption of stabilizers onto the graphene layers. In particular, pyrene derivatives with sulfonyl groups produced stable colloidal dispersions over a wide range of pH values. Herein, we aim to demonstrate that the concept of functionalizing pyrene as graphene dispersants can be generalized to larger polyaromatic particles (i.e., graphene quantum dots) acting as graphene dispersants.

Graphene quantum dots (GQDs) and carbon dots (CDs) are mono- or few-layered graphene sheets with lateral dimensions smaller than 100 nm, though GQDs are of higher crystallinity.[58] Such quantum dots possess unique properties, such as high photoluminescent quantum yield, cost effectiveness, low cytotoxicity, and biocompatibility.[59-63] Therefore, they have been investigated extensively for applications such as bioimaging,[59, 64] solar cells,[60, 65] and surfactants.[57, 66-67] Experimentally, by carefully controlling surface chemistry and structure, GQDs have been fabricated by chemical oxidation of carbon black,[68] solvothermal cleaving of graphene oxides,[69] electrochemical exfoliation of graphite,[70] thermal degradation of organic molecules,[71-72] ruthenium-catalyzed decomposition of C_{60}[73] and stepwise organic synthesis.[74-75] In fact, GQDs possess aromatic cores, and with proper functional groups, can be expected to prepare stable graphene dispersion. GQDs with carboxylic groups (-COOH) have been used to stabilize commercial graphene powder by He *et al*. in 2014,[131] but a direct exfoliation of graphite into graphene by GQDs has not been discussed. Recently, an attempt was made to prepare graphene from graphite by using small-sized CDs (~1.8 nm) with amino functional groups (-NH_2) to produce graphene aqueous dispersion.[132] Despite these prior studies, the influence of GQDs with different functional groups on producing graphene dispersions is still poorly understood, and a comprehensive study that provides a control of the functionalities of GQDs derivatives is missing.

In this study, we design and characterize novel graphene quantum dots with sulfonyl ($-SO_3^-$) functionalization (S-GQDs), and compare these against carboxylic functionalized GQDs (C-GQDs) and amine functionalized GQDs (N-GQDs) as dispersants for preparing graphene in aqueous solution. We show that the concentration of dispersed graphene depends considerably on polar functional groups present on the polyaromatic GQDs. We demonstrate that their functionalities affect the formation and strength of π-π stacking interactions, which determines graphene exfoliation efficiency. The as-prepared aqueous graphene dispersion demonstrates colloidal stability, which can be used for enhancing the color contrast of photonic crystals by suppressing incoherent scattering and multiple scattering.

2.2.2 Synthesis of amphiphilic S-GQD

S-GQDs were fabricated by direct condensation and pyrolysis of citric acid and 4-styrenesulfonic acid sodium salt. In a typical procedure, 1.4 g citric acid and 0.6 g 4-styrenesulfonic acid sodium salt were mixed by a homogenizer. The white solid mixture was then transferred into a 20-mL glass vial and calcinated in air at 200 ^{o}C for 80 min. The dark solid residue was further purified by a dialysis tube (2000 Da) to remove possible unreacted starting materials. The final product S-GQDs were further dried by a freeze-drying machine. GQDs with amine functional groups (N-GQDs) and carboxylic acid groups (C-GQDs) were prepared based on previous works.

2.2.3 S-GQD as solid-liquid surfactants

In light of the recent reports on improving the graphite exfoliation efficiency using polycyclic aromatic compounds, such as pyrene derivatives as dispersant, we synthesized novel aromatic GQDs with sulfonyl functionalization in the present work. As shown in Figure 12, S-GQDs were fabricated by a direct condensation and pyrolysis of citric acid and 4-styrenesulfonic acid sodium salt. At 200 ^{o}C in the presence of air, a polymer-like aromatic intermediate was first formed by condensation of citric acid, and then linked with C=C double bonds of 4-styrenesulfonic acid sodium salts via a thermal polymerization reaction.[71, 133-134] No products were observed if the reaction was performed in presence of pure nitrogen, indicating a crucial role of oxygen in free-radical polymerization as an initiator and promoter.[134] To remove excess starting materials and potential polymeric byproducts, the crude products were further purified by performing dialysis (2000 Da) for 4 days. This one-pot fabrication of sulfonyl graphene quantum dots is straightforward, low-cost, eco-friendly, and easily scalable. The fabrication conditions are fairly gentle without need of expensive catalysts or toxic organic solvents.

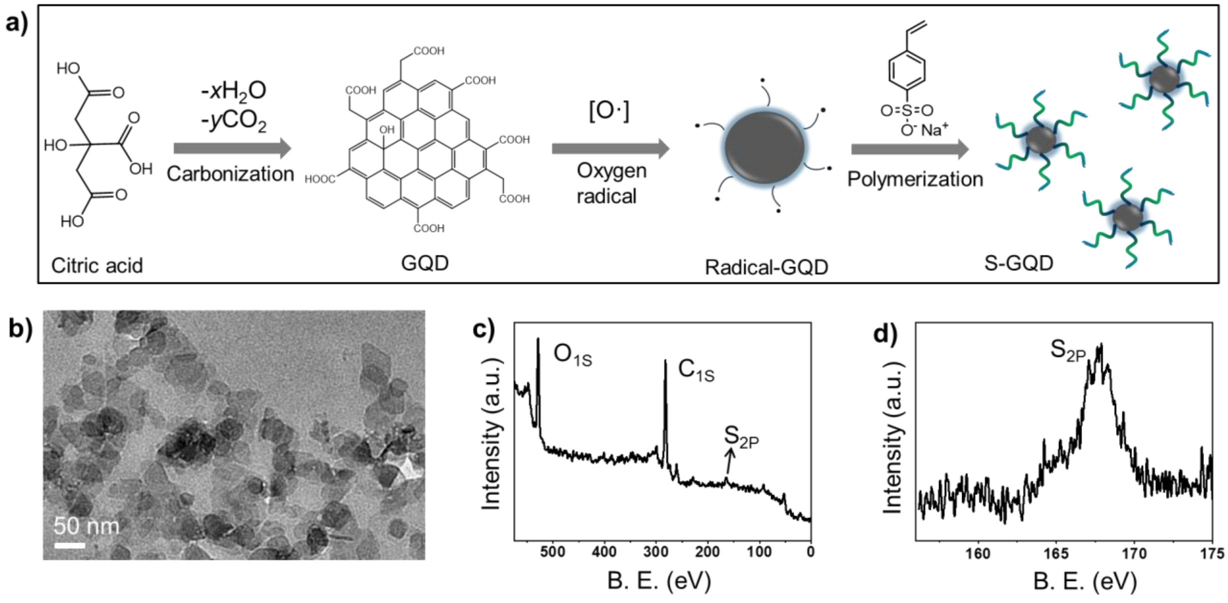

Figure 12. Fabrication of sulfonyl-grafted graphene quantum dots.

The morphology of S-GQDs was studied by transmission electron microscopy (TEM). Figure 12b shows a typical TEM image of S-GQDs, showing the size of the as-prepared S-GQDs distributed in the range of 15-55 nm with an average diameter of 28.7 ± 5.4 nm. This size distribution is similar to that of other types of GQDs prepared by different methods reported in literature.[57, 59] The surface chemistry of S-GQDs was next characterized by X-ray photoelectron spectroscopy (XPS) and Fourier transform infrared spectroscopy (FTIR). According to the survey XPS spectrum of S-GQDs (Figure 12c), S-GQDs are mainly composed of carbon, oxygen, and small amount of sulfur with an atomic ratio of 26:10:1, which is further confirmed by elemental analysis. The existence of C-S bonding is further proved by S_{2P} XPS spectrum (Figure 12d), which show the presence of sulfonyl functional groups (SO_3^{-1}, 167.5 eV). In the FTIR spectrum of S-GQDs, several characteristic vibrational bands at 1175 cm^{-1}, 1405 cm^{-1}, 1610 cm^{-1}, 1730 cm^{-1}, 2930 cm^{-1}, 3460 cm^{-1} are found, which are assigned to the stretching vibrations of C-S/C-O, bending vibrations of C–H, vibrational bands of C=C, stretching vibrations of –C=O, stretching vibrations of C–H, and the stretching vibrations of C-OH respectively.[108, 114] These results confirm the successful grafting of sulfonyl groups onto GQDs.

We next investigate the photoluminescence (PL) spectra of this novel type of graphene quantum dots. As shown in Figure 13a, as excitation wavelength is increased from 360 to 420 nm, the PL peak position shifts to longer emission wavelength. This excitation-dependent PL behavior is common in fluorescent carbon materials, and is used to obtain desired PL colors by controlling the wavelength of excitation light.[61] The PL intensity distribution can be explained by the effect of GQD size distribution on the band-gaps.[116] In PL spectra, S-GQDs have optimal excitation and emission wavelengths at 380 nm and 458 nm, respectively. The optimal excitation peak is relatively red-shifted compared with that of reported small-sized GQDs due to the quantum confinement effect which governs the ultraviolet light that is absorbed.[135-137] In order to explore the potential of S-GQDs as an exfoliation agent and dispersant for graphene, its stability was examined under tip sonication, as sonication is a commonly used method to facilitate liquid-phase exfoliation of graphite into graphene.[27] Tip sonication uses high energy sound waves which are generated by a piezoelectric actuator. To prove that the sonication process will not cause fragmentation of S-GQDs, we compared the UV-Vis spectra of S-GQDs before and after sonication for 1 h. As shown in Figure 13b, a bright blue luminescence of the S-GQDs aqueous solution (0.2 mg·mL^{-1}) under the illumination of a UV (365 nm) light is shown without any visible change before/after sonication. Moreover, there is no observable difference in absorption peak positions, indicating that GQDs are not altered by sonication. These results show that GQDs can tolerate sonication conditions required for exfoliating graphite into graphene.

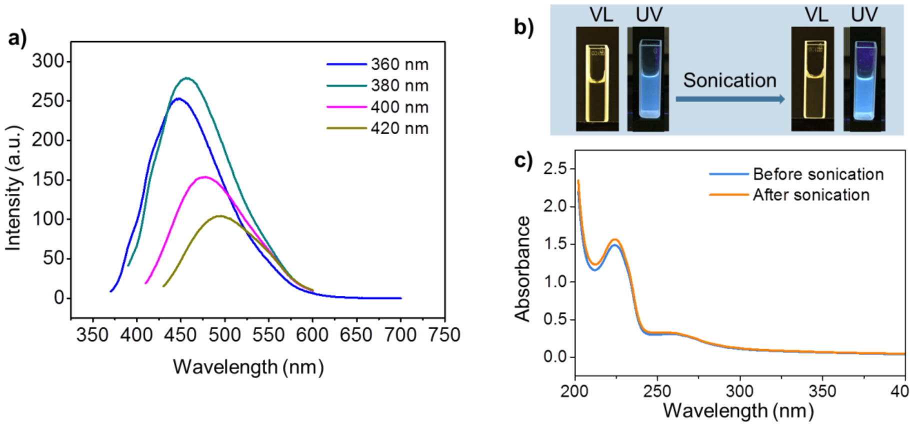

Figure 13. Spectroscopy of S-GQDs.

We then evaluated the capability of S-GQDs to stabilize pristine graphene exfoliated from graphite in aqueous solution. Tip sonication was used to achieve lab-scale liquid exfoliation of graphite to graphene, as shown in Figure 14a. For this study, we sonicated slurry of S-GQDs and graphite dispersed in water. As a result, graphite is exfoliated into a mixture of single- to few-layered graphene sheets (referred to as graphene nanosheets here onwards) and multilayered (layers > 5) graphitic flakes.[138] The resulting slurry was centrifuged at 500~3000 rpm causing the heavy graphitic fractions to sediment, and the supernatant was extracted. The concentration of graphene nanosheets in the supernatant was measured to be 0.16 mg.mL^{-1} using UV-Vis spectroscopy (see the methods section for more details). This graphene concentration of 0.16 mg.mL^{-1} is comparable to that reported for graphene sheets prepared by direct exfoliation with surfactants, polymers, and polyaromatic hydrocarbons at the similar concentrations of stabilizers.[26-27, 139] Such dispersions showed colloidal stability without any noticeable sedimentation and aggregation over a period of 30 days. The zeta potential (ξ) of this graphene dispersion was measured to be about -64.3 mV, indicating excellent colloidal stability.

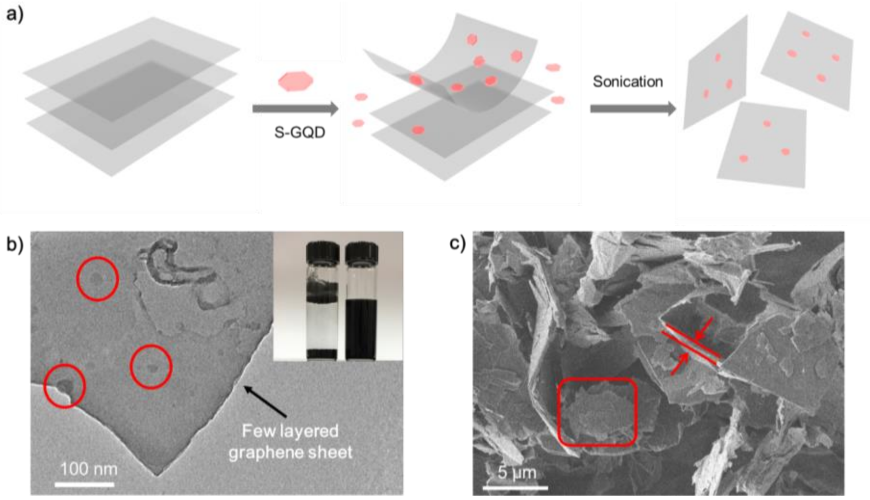

Figure 14. Exfoliation of graphite with S-GQDs.

To confirm the presence of single- to few-layer stabilized graphene in the dispersions, the S-GQDs-stabilized graphene samples were characterized using TEM. Counting the number of folds at the edge of a graphene sheet in TEM is a widely used technique for characterizing the number of layers. As shown in Figure 14b, the edge count of graphene sheets reveals that the S-GQDs-stabilized graphene is 2- to 5-layers thick, as commonly observed in sonicated and centrifuged samples.[27] Atomic force microscopy (AFM) was performed on these S-GQDs-stabilized graphene nanosheets. AFM height profiles were consistent with 2-3 layers thick graphene nanosheets, and the presence of S-GQDs on their surface. However, for starting material graphite, the SEM image shows a large lateral size around 5–20 μm with thickness of 0.5–1 μm (Figure 14c), indicating that the exfoliated graphene sheets have much smaller lateral size with reduced thickness.

2.2.4. Conclusions

In summary, we demonstrated that π–π stacking interactions with graphene are not limited to pyrene derivatives, but are also applicable to larger polyaromatic structures such as graphene quantum dots. We also showed that S-GQDs can stabilize solid/liquid interfaces for the graphene aqueous dispersion.

CHAPTER III

SURFACE-ACTIVE JANUS NANOPLATELETS AND ACTIVE SOFT MATTER

3.1 Janus nanoplatelets as nanogates

3.1.1 Background

In biology, membrane proteins assembling at the lipid bilayer interfaces execute various biological functions including ion conduction and channel gating.[140-141] Inspired by nature, the active assembly of nanoparticles (NPs) at interfaces has drawn significant interests in developing NP-stabilized heterophasic systems at multiple length scale, from the microscopic control of polymer morphologies,[57] to the macroscopic fabrication of interconnected bijels.[142] These NP-stablized structures enable superior properties for many applications such as design of high-efficient catalysts,[143] fabrication of electrodes,[144] and manufacture of scaffolds.[145] Furthermore, the ability of NPs to regulate the shapes of multiphasic systems and the possibility of nanomaterials to precisely manipulate surface properties of emulsions may also promote novel synthetic techniques, *e.g.*, shape memory organohydrogel materials.[146]

In contrast to molecular surfactants that freely diffuse and dynamically exchange between the oil/water interface and the continuous phase, particle surfactants can tightly assemble on the fluid-fluid interfaces to stabilize nonequilibrium emulsion shapes due to the interfacial jamming effect. Such close-packing behaviours of NPs have showed unique advantages for interfacial

---

Parts of this section are reprinted with the permission from John Wiley and Sons publishing: Luo, J.; Zeng, M.; Peng, B.; Tang, Y.; zhang, l.; Wang, P.; He, L.; Huang, D.; Wang, L.; Wang, X.; Chen, M.; Lei, S.; Lin, P.; Chen, Y.; Cheng, Z., Electrostatic‐driven Dynamic Jamming of 2D Nanoparticles at Interfaces for Controlled Molecular Diffusion *Angewandte Chemie International Edition* **2018**, *130* (36), 11926-11931. Copyright (2018) John Wiley and Sons.

applications in chemical barriers and controlled release.[147] Recently, an asymmetrically modified two-dimensional (2D) nanoparticle system was developed by exfoliation of layered zirconium phosphate, enabling a temperature-triggered release of liquid crystals.[148] In addition to the "one-way" release, the imitation of the dynamic gating function of biological ion channels appears to be highly valuable, particularly for long-term applications such as controlled release of corrosion inhibitors in oil pipelines.[149] To achieve such switchable releasing feature, an ideal NP surfactant should form a robust multilayer film at the interfaces to prevent the escape of encapsulated substances, while becoming repulsive upon introducing the stimuli in a quick and possibly adjustable manner. Meanwhile, the NPs should be compatible and stable with a wide range of liquids for broad application purposes. Despite considerable theoretical and experimental advances in interfacial nanoparticles,[150-155] however, a smart NP that can lock and unlock the interface to precisely and dynamically manipulate molecular diffusion has rarely been reported.

3.1.2 Characterizations of SJPs

In this study, we propose novel smart jamming platelets (SJPs) based on disk-like kaolinite NPs to dynamically jam at the oil/water interfaces with "lock" or "unlock" states. To achieve reversible jamming at interfaces, two factors have to been considered in designing the surface chemistry of NPs. On one hand, an intermolecular attractive interaction of NPs should be robust to form jamming to lock the interfaces. On the other hand, a functional group of NPs, which generates strong repulsive force to overcome the intermolecular attraction upon introducing stimuli, is required to unlock the interfacial jamming of NPs. Based on the above principle, we designed a pH-responsive nanoplate with zwitterionic feature by covalently functionalizing negatively charged platelets with cationic polymer, poly[2-(dimethylamino)ethyl methacrylate] (PDMAEMA). Hydrophobic poly (lauryl methacrylate) (PLMA) was simultaneously grafted on kaolinite platelets to enhance the affinity of NPs with oils. Such strategy enables the robust intermolecular attraction of oppositely charged groups on SJPs at lock state, while a strong electrostatic repulsion would arise upon fully protonated PDMAEMA polymers at low pH value, referring to unlock state. As shown in Figure 15a, the pristine kaolinite was first treated with a synthetic bromo-organosilane, prepared by a controlled bromination reaction of 3-(trimethoxysilyl) propylmethacrylate, forming multiple bromine functional groups on the platelet surface for the initiation of polymerization. Next, the surface-modified kaolinite platelets were transferred to the oil/water interface where surface-initiated atom-transfer radical polymerization (SI-ATRP) occurs,[156] leading to a "Janus" functionalization of kaolinite platelets.

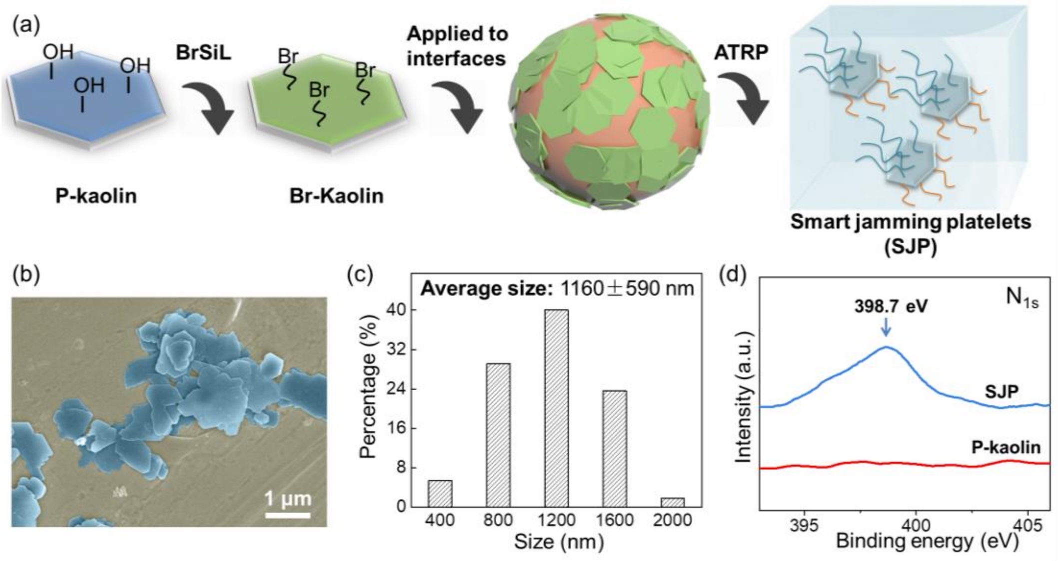

Figure 15. Synthesis and characterizations of smart jamming platelets.

The morphology of SJPs was examined by field-emission scanning electron microscope (FE-SEM). The SJP showed a smooth surface with size mostly between 1.0 to 1.8 μm, where the average size was 1.16 ± 0.59 μm (Figure 15b-c). To investigate the surface chemistry of SJPs, high resolution C^{1s}, O^{1s}, and N^{1s} XPS spectra were collected. N^{1s} XPS spectra of SJP showed a strong peak at 398.7 eV while no observable peaks are found for pristine kaolinite (Figure 1d).

XPS elemental analysis of the SJPs was also carried out, revealing a C:O:N atomic ratio of 14:8:1. The surface chemistry of kaolinite particles was further confirmed by Fourier transform infrared spectroscopy. We found the characteristic vibrational bands at 1005, 1450, and 1730 cm^{-1}, corresponding to the overlapped stretching vibrations of Si-O and Al-O, the bending vibration of C-H, and the vibrational band of ester group -(C = O)-O, respectively. In addition, we characterized the Janus feature through a side-selective adsorption strategy.[157-158] Upon mixing with other hydrophilic NPs, we can clearly differentiate the PDMAEMA side and PLMA side by comparing the surface morphology.

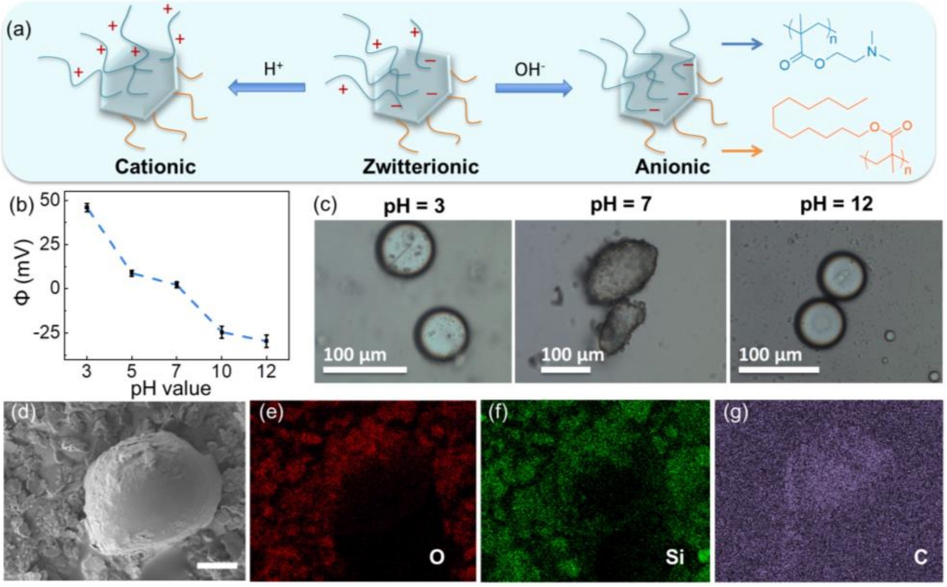

Figure 16. The pH-responsive SJPs.

In designing NPs to achieve electrostatic-driven switchable interfacial jamming, we hypothesized that the PDMAEMA chains of SJPs underwent a protonation of the tertiary amine groups at low pH and hence became highly cationic, while a deprotonation of silicate groups of NPs occurred at high pH, as shown in Figure 16a. We investigated the surface charge behaviours of SJPs using zeta potential measurements, which confirmed the heavy dependency of the SJP's charge states on solution pH values (Figure 16b**)**. Upon increasing pH from 3 to 7, the initial zeta potential of kaolinite (48 mV) changed to ~zero due to the partial deprotonation of charged PDMAEMA chains, forming a zwitterionic state. The zeta potential value became negative when further increasing pH from 7 to 12, likely due to the deprotonation of surface silicate Si-OH to Si-O$^-$.[159-160] Interestingly, past studies have revealed that pristine kaolinite showed exclusively negative zeta potential over various pH values (pH = 1~14),[160] indicating that the graft of PDMAEMA induced a remarkable change in platelet surface charge.

We expected such change of surface charge on SJP would actively affect their accumulation, assembly and jamming at the oil/water interfaces. To examine this idea, we used SJP surfactants to generate emulsions under different pH values while keeping the volume ratio of oil and aqueous phases at 1:9, to avoid the influences of dominant fluid phase on the final emulsion geometries.[161] After the emulsification process, water settled to the bottom of the vials with excess oil phase remaining on top of the settled emulsions, indicating formation of oil-in-water emulsions under all pH values. However, as shown in Figure 16c, microscopic images showed remarkable difference of emulsion shapes under pH = 3, pH = 7, and pH = 12, indicating the change of interfacial jamming of SJPs. The emulsion droplets were exclusively spherical when platelet surfactants were highly charged at either low pH or high pH, whereas jammed nonspherical droplets were observed at pH = 7 (low zeta potential). At pH = 7, various geometries of emulsions, *e.g.*, ellipsoids and cylinders, existed together with spherical drops in the same suspension.

It is worth noting that the SJPs remained at oil/water interfaces during unlock state (pH = 3), instead of completely diffusing into aqueous phase. To study the SJP distribution at unlock state, we solidified the liquid droplets by replacing dodecane with polymerizable oil (styrene).

After polymerizing styrene droplets stabilized by SJPs at pH = 3, we used SEM to analyze the surface of solidified polystyrene (PS) emulsions. Figure 16d showed disk-like particles loosely scattered on PS surface. We observed that the solid PS ball was not as spherical as its precursor styrene, probably due to the synergetic effect of uneven polymerization and partial phase separation during thermal polymerization.[162-163] To ensure that the observed platelets were SJPs, we applied energy-dispersive X-ray spectroscopy (EDX, Figure 16e-g), which showed the consistent distribution of Si and O on platelets. These results confirmed that loose distribution of SJPs on liquid droplets at unlock state. SEM images of polystyrene drops during locked state have also been performed and showed a close-packing behaviour of SJPs on PS surface. We also found that the unlocking of jammed shapes can be achieved by mild adjustment to pH = 5 or pH = 9, though the shape relaxation is much slower.

To explore the SJP as a universal jamming agent, we studied the interfacial jamming of SJPs using different oils, from to light oil heptane (0.68 g/mL) to dense oil carbon tetrachloride (CCl_4, 1.59 g/mL). In addition to dodecane, heptane, toluene and CCl_4 droplets exclusively showed a tunable interfacial jamming of SJPs. Upon tuning the solution pH values, the oil droplets with lock state underwent a quick transition into unlock state, despite a wide range of viscosity of oil phases (heptane 0.42 cP, toluene 0.59 cP, CCl_4 0.97 cP, and dodecane 1.37 cP). To visualize the pH effect on emulsion shape, we recorded the shape transformation of emulsion stabilized by SJPs. In the presence of SJPs, the dodecane was first emulsified into oil-in-water emulsions, which were then filled into a capillary. The pH change in capillary was achieved by an H^+ gradient technique. Introducing a small amount of acid or base at one end of capillary allowed H^+/OH^- to diffuse toward emulsion surface without strong shearing effect. After introducing ~2 μL of 0.01 M HCl solution, the interfacial jamming of NPs disappeared, leading to a structural transition from nonequilibrium shape into spherical configuration. A similar trend was seen upon adding 2 μL NaOH solution, though the unlocking process was slower due to less surface charges according to zeta potential measurement. However, when 2 μL NaCl solution was added into emulsion suspension, there was no observable change in the shape, and more importantly the jamming state of oil drops. To ensure that the dynamic jamming of SJPs was not influenced by ionic strength, 2 μL of DI water was introduced and no shape change was observed. These results confirmed the role of solution pH of the continuous fluid in governing the jamming of SJPs at oil/water interfaces.

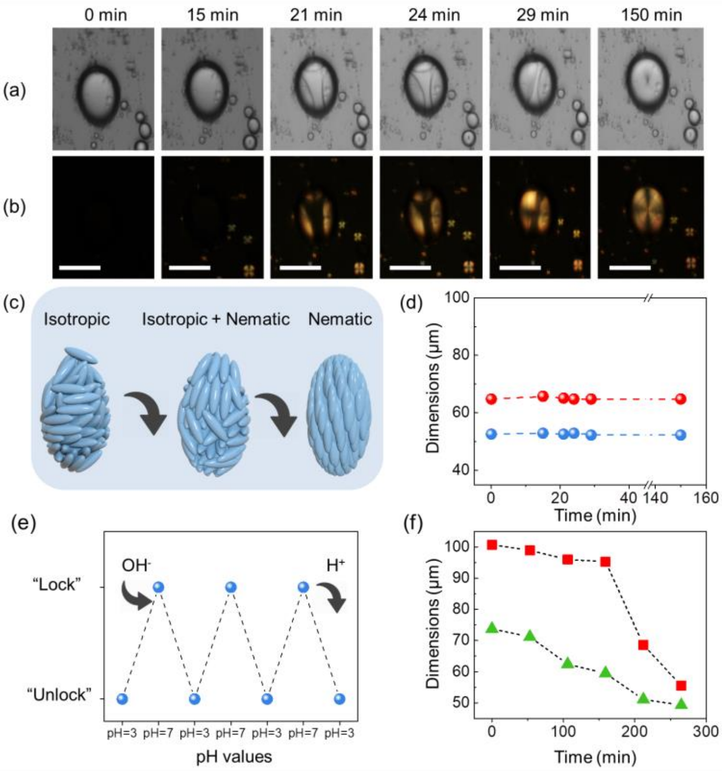

Figure 17. I-N transition of 5CB droplets stabilized by SJPs (0.5 wt%) at pH=7.

As a prominent type of emulsion droplets, liquid crystal (LC) droplets have been investigated extensively as stimuli-responsive soft materials in which the LC configuration inside the droplets can be altered by temperature,[164] chemicals,[165] and biological species.[166-167]

However, little is known on the phase behaviour of LC droplets in a jammed shape. In this study, we explored the potential of SJPs to stabilize LC droplets on their nonequilibrium shape. 4-cyano-4'-pentylbiphenyl (5CB), a hydrophobic material with birefringence property under polarized optical microscopy (POM), was used as the oil phase. After introducing 0.5 wt% of SJP surfactant, the 5CB was readily emulsified into emulsion droplets by using a vortex mixer. At pH=7, the POM images of 5CB droplets clearly revealed a mixture of spherical and nonspherical LC droplets with cross-like birefringence. By contrast, 5CB-in-water emulsions stabilized by sodium dodecyl sulfate (SDS, 0.5 wt%) exclusively showed the spherical emulsions without other shape at pH=7. The distinctive behaviour of the SJPs highlights the difference from molecular surfactants which do not jam at the interface due to a much shorter relaxation time and a dynamic exchange between the adsorbed molecules and freely diffusing species in suspension.[168]

In addition, the thermotropic feature of 5CB droplets allows us to investigate the thermal stability of dynamic jamming of NPs upon heating or cooling. Upon switching temperature to 42 ^{o}C, a transition from the nematic phase to isotropic configuration was observed, where luminous droplets begin to disappear in the dark field. The phase transition took about 10 minutes, longer than that of pure 5CB liquid crystal, probably due to thermal convection and conduction in aqueous solution.[169-170] It was interesting to note that the size and shape of non-spherical droplets remained almost unchanged, despite significant alteration in 5CB LC configuration. This can be explained by strong interfacial jamming of SJPs at water/5CB interface, providing robust energy barrier preventing 5CB drop relax into a perfectly spherical shape. As shown in Figure 17a, an oval shape of LC droplet was chosen and isotropic-to-nematic phase transition was also investigated. After setting up a temperature controller to 20 ^{o}C, a bright LC birefringence was developed from the edge, as the temperature was lower from outside of 5CB droplets. As the temperature gradually decreased, the luminous birefringence parts slowly fused, and finally formed a cross-like texture of nematic phase, as shown in Figure 17b-c. To quantitatively evaluate the shape and size of 5CB droplets during annealing, we calculated the length of long axis and short axis of this oval-shape drop, showing that there is almost no noticeable change, as shown in Figure 17d. Despite the exceptional stability against the change of temperature, the shape transition of 5CB-in-water emulsion remained feasible by introducing H^+.

In addition to the one-way transition, we found that the interfacial lock and unlock could be reversible. After neutralizing the suspension pH value close to 7, we observed that the jamming of NPs at oil/water interfaces recurred, leading to the regeneration of nonspherical oil droplets by simply re-shaking the suspension. As the jamming of our NPs was relatively insensitive to salinity, we were able to achieve reversible interfacial jamming for multiple times, despite the accumulation of salts during neutralization process (Figure 17e). We recorded the horizontal and vertical lengths of a nonspherical drop over time, revealing a clear deformation in shape as shown in Figure 17f.

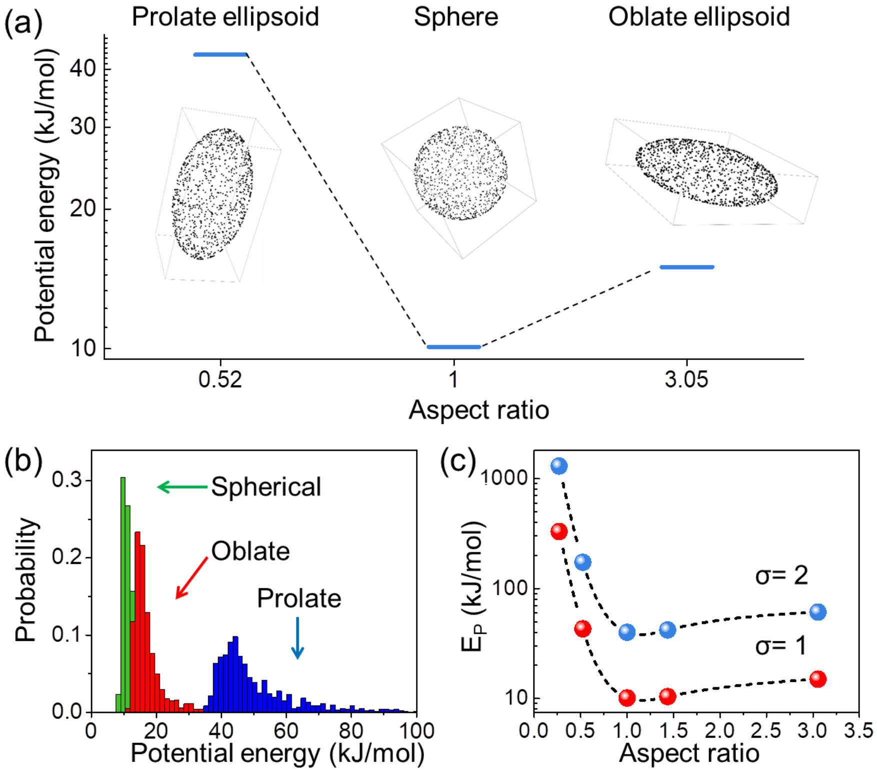

Figure 18. Monte Carlo calculation of electric potential energy (E_P).

Another goal of our work was to provide a better understanding on the dominating driving force that regulates the shape transition of droplets and dynamic jamming of SJPs. Here we considered that two main interactions were changing during shape transition: surface energy and electrostatic energy. During shape relaxation induced by H^+, the surface energy was reduced owing to the decreased surface area; however, given that shape-changing only occurs by H^+ or OH^-, we hypothesized that the electrostatic interaction should play a major role in the shape relaxation. To validate the proposed dynamic mechanism, we used the Monte Carlo method to calculate the relative potential energy of electrostatic interaction. By assuming that the charge density of individual droplets was constant, we evaluated the electric potential enery (E_P) of three different shapes: sphere, prolate ellipsoid, and oblate ellipsoid (Figure 18a**)**. Here, we defined a parameter, aspect ratio ξ = z-axis length (Z) / x-axis length (X), to describe the tendency of drop deformation. Upon keeping the normalized volume of droplets $V_{drop} = 1$, we found that the spherical drop has the lowest potential enery E_P in comparison with prolate ellipsoid and oblate ellipsoid. Figure 18b showed statistic distribution of E_P for 1000 random NPs on a drop. It is obvious that the charged particles on spherical shape hold not only the statistically minimal energy, but also the narrowest energy distribution among three shapes. This well explains the observation that the charged ellipsoid drops readily undergo a shape transition into spherical as such process is much more energetically favorable. Additionally, we studied the effect of charge density (σ) on E_P which represented the stability of jamming shapes under different surface charge intensity (Figure 18c**)**. Upon increasing the σ, the potential energy of all different jamming shapes, particularly with prolate ellipsoid, rose up significantly. As discussed previously, an increment in the concentration of H^+ will increase the surface charge, leading to a much shorter time of shape transition. Such observation is exceptional consistent with simulation results, which showed a dramatic increase in E_P upon doubling the charge density.

3.1.3 SJPs nanogates at interfaces

The ability of SJPs to switch on and off the interfacial jamming is a reminiscent of the protein-based ion channels that can be open and shut to control molecular transport.[171] In principle, the behaviours of SJPs to closely assemble or disassemble at oil/water interfaces were expected to regulate the interfacial molecular diffusion, *e.g.* solvent evaporation (Figure 19a**)**. First, the release of hexane from hexane-in-water emulsions was investigated. Allowing hexane droplets to evaporate for 24h at room temperature (please see Supporting Information), we measured the amount of hexane retained by using a dye tracer technique. At pH = 7, the retained percentages of hexane increased (up to 98%), upon increasing the concentration of SJPs. Sodium dodecyl sulphate solution (0.2 wt%) was also used as stabilizer, whereas the retained ratio was much lower than that of SJPs (0.2 wt%).

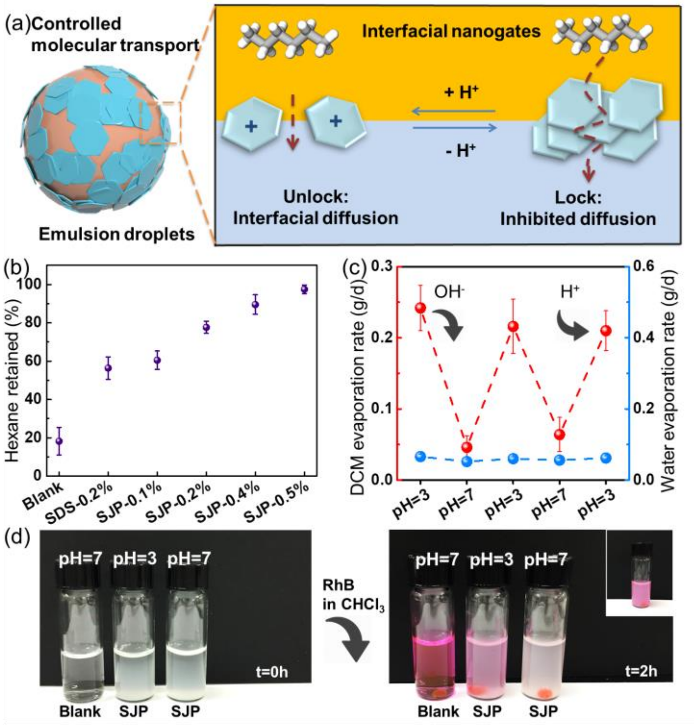

Figure 19. The demonstration of SJPs to control molecular transport at interfaces.

The evaporation of another solvent, dichloromethane (DCM), was also studied. By performing pH switching cycles from 3 to 7, we observed a more than 5 folds of decrease in DCM evaporation rate, while the water evaporation rate remained almost unchanged. More importantly, despite the accumulation of solution salts during "acidizing" and "neutralizing" processes, the SJPs maintained the ability to automatically assemble and disassemble at interfaces, allowing molecular diffusion in a controlled and repeatedly manner. To the best of our knowledge, this is the first example that the interfacial diffusion can be dynamically and repeatedly regulated using the dynamic jamming of pH-responsive 2D nanoparticles. As a proof of concept for controlled drug release, we investigated the diffusion behaviours of rhodamine B

(RhB) at interfaces. After introducing RhB (0.3 wt% in chloroform), we observed that RhB diffused quickly in DI water, whereas little diffusion was observed 0.5 wt% SJP solution after 2h. This was confirmed by using UV-Vis spectra, showing RhB concentrations >2000% higher in the unlocked SJP solution than in the locked SJP solution.

Additionally, the fluorescent microscopy of $CHCl_3/H_2O$ interface confirmed the gating behaviour of SJPs. To evaluate the RhB releasing behaviour of SJPs, we performed time-dependent UV-vis spectroscopy on aqueous phase in which the releasing of encapsulated RhB can be detected. At early stage (0~200s), the RhB concentration grew dramatically in DI water (red), while only slight increase in RhB was observed in 0.1 wt% SJP solution (purple). Upon adding 30 μL of 0.1 M HCl aqueous solution, the RhB concentration rose up considerably which indicated the fast release of RhB from to water due to the unlock of interfacial jamming of SJPs. These results confirm our hypothesis that smart jamming of NPs at liquid–liquid interfaces is able to control molecular transport, leading to a controlled release of species into continuous phases, a unique feature not achievable by small molecular surfactants.[172]

3.1.4 Conclusions

In conclusion, we demonstrate the ability of judiciously designed Janus kaolinite nanoplates to dynamically assemble, accumulate, and pack at oil/water interfaces. The nonequilibrium shapes of resulting microemulsions are stable against change of temperature or addition of salt, while droplet morphological transitions can be achieved effectively and repeatedly by adjusting pH values. An electrostatic model has been proposed to understand the dynamic jamming of SJPs and reversible shape transition of droplets, which was further verified by Monte Carlo calculation. The electrostatic-driven reversible interfacial jamming of NP-surfactants disclosed herein is expected to open a brand-new door for their promising applications in areas of controlled drug delivery, functional intelligent nanoplatforms, and many other biomedical-related fields.

3.2 Active nanoplatelets as nanocleaners

3.2.1 Background

Nanoparticles (NPs) that mimic the functions and behaviors of their natural counterparts have drawn significant research interest.[173-174] Particularly, the ability of active NPs to respond to chemicals, light, ultrasound, and electric/magnetic fields have led to diverse applications including cargo delivery,[175] wastewater treatment,[176] and DNA detectors.[177] Recently, a bowl-shaped micromotor, resembling the shape of jellyfish, has been developed with the ability to dynamically control the velocity upon the temperature change.[178] In addition, the design of a unique nanomotor shape and the possibility of particle shapes to regulate the fluidic dynamics may allow novel nanoswimmer systems, for example, the super-diffusive nanobottle motors.[179]

As a crucial factor, the velocity of micro/nanomotor, especially at low fuel concentration (H_2O_2 <8 wt%), can strongly affect the performance of active nanomaterials in applications such as motional lithography and heavy metal recovery.[180-181] Theoretic efforts have been made to predict the factors that determine the translational velocity including size, geometry, and solution viscosity.[182] For example, the experimental and theoretical studies on Janus particles half-coated with platinum (Pt) showed the velocity with an inverse size dependence.[183] A recent study on the geometrical factors suggested that two-dimensional (2D) nanoparticles may possess unique advantage over other shapes, *e.g.* sphere and rod, as the discotic designs can be more efficient at converting chemical energy into speed.[184] However, reusable nanomotor with 2D shape has not yet been experimentally realized, and the incoporation of magnetic character in 2D nanomotors may enable additional advantage of facile separation and recovery, facilitating the practical applications.

Here, we report a 2D magnetic nanomotor that functions as nanocleaners to efficiently and repeatedly decontaminate organic pollutants and particle stains. In contrast to conventional magnetic nanomotors enabled by electrodeposition of Ni or Co,[180, 185] our magnetic nanoplatelets were built on the controlled synthesis of ferromagnetic barium ferrite (BF) nanoplates. By sputter coating with Pt, a series of Pt-coated BF (PtBF) nanoswimmers were prepared. Although the bubbles formed by H_2O_2 decomposition posed an imaging challenge for studying active colloidal physics, we took advantage of the formed nano-bubbles to effectively promote the microconvection during the decontamination process.

3.2.2. Synthesis and characterization of PtBF

We fabricated the PtBF by a two-step strategy involving physical vapor deposition of Pt on BF platelets followed by the template removal using ultrasonication (Figure 20a**)**. In the first step, the hydrothermally synthesized BF nanoplatelets were coated on a pre-cleaned Si wafer, after which a thin layer of Pt was deposited. In the second step, as the BF nanoplatelets formed no chemical bonds with Si wafer such that the PtBF nanoparticles can be readily removed from the wafer by ultrasound. Using a magnet, the Pt-coated BF were purified and separated from the possible byproducts. Such process of synthesizing 2D magnetic nanomotors is simple, straightforward, and highly flexible, which may allow for fabricating other 2D nano-/micromotors, *e.g.* graphene oxide nanosheet or Ag nanoplates.[186-187] As shown in Figure 20b, the transmission electron microscopy (TEM) revealed a polydispersed hexagonal structure of PtBF with average size of 23.1 nm (size analysis in Figure 20c). Such result showed that PtBF nanoparticles shared the similar 2D characteristics with pristine BF nanoplatelets (inset of Figure

20b). The atomic force microscopy (AFM) exhibited that the pristine BF nanoparticle with thickness of 1.70 ± 0.52 nm. However, AFM analysis presented a thickness of XX nm of PtBF in contrast to the ~2-nm thickness of pristine BF. It is worth mentioning that such thickness is much thinner than most Ni-based nanomotor.[180]

To investigate the surface chemistry of PtBF nanoplates, the high resolution Pt_{4f} and Fe_{2p} XPS spectra were collected. As shown in Figure 20d, the strong signals of PtBF with binding energies of 72.1 and 75.6 eV can be assigned to $Pt_{4f7/2}$ and $Pt_{4f5/2}$, respectively. However, no observable Pt_{4f} peak was found for pristine BF nanoparticles (red line). As shown in Fe_{2p} XPS spectra of the PtBF specimen, the presence of $Fe_{2p3/2}$ peaks at 710.9 eV indicated the Fe^{3+} with no significant existence of Fe^{2+}, confirming that there was no reduction occurring during the deposition of Pt. These results indicated the successful deposition of Pt on BF nanoparticles without destroying the BF structures.

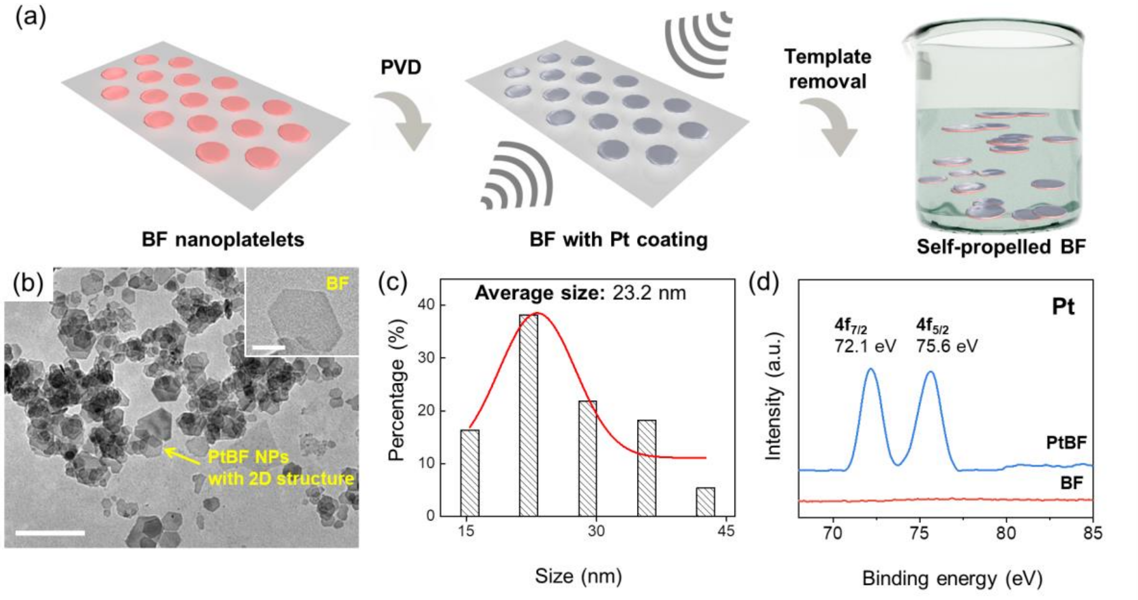

Figure 20. Preparation and characterization of PtBF platelets.

3.2.3. Self-propelled PtBF

For nanomotors fueled by H_2O_2, the self-propelled velocity (V) is closely related with the apparent diffusion coefficient (D_{app}) where a substantial increase in D_{app} would be expected upon adding hydrogen peroxide. The swimming speed of PtBF can be obtained from the equations: (1) $D_{app} = D_0 + L^2/4\tau$ and (2) $V=L/\tau$, where D_0 is the intrinsic diffusion constant without H_2O_2, τ is the relaxation time for a specific H_2O_2 concentration, L is the average ballistic swimming length during the τ. To optimize the self-propelled speed of PtBF under strong Brownian forces, we prepared and evaluated three types of PtBF nanoplates with different amounts of Pt: small (PtBF-S), medium (PtBF-M), and large (PtBF-L). First, we measured the intrinsic diffusion constants of PtBFs in the absence of H_2O_2. Upon increasing the deposition thickness of Pt, we observed a clear decreasing trend of diffusion constant of PtBF (Figure 21a). This was well consistent with the fact that a nanoparticle with smaller size would undergo a strong Brownian motion.[188] As a control, we also synthesized iron (III) based nanoparticles, Fe_2O_3, with much large size (750 ± 220 nm), which verified the trend of diffusion constant. However, the apparent diffusion increased dramatically even though a highly diluted H_2O_2 (aq) was introduced into PtBF solutions. As shown in Figure 21b, the apparent diffusion constant of PtBF increased more than 200% by simply introducing 0.1% H_2O_2 whereas no observable change was found in diffusion rate for pristine BF nanoparticles. The absence of diffusion enhancement of pristine BF NPs indicates that the deposition of Pt on BF is a crucial factor for the active motion of nanomotors. This was also consistent with the observation that no bubble was formed when only pristine BF NPs was mixed with H_2O_2. It is worthnoting that free Fe^{3+} ions can also catalyze the decomposition of H_2O_2, known as Fenton's reaction, whereas some reported works suggested that iron-catalyzed alkaline-earth ions, Mg^{2+} or Ba^{2+}, can retard such reaction.[189] A comparison of the enhanced diffusion among different PtBFs showed that the PtBF-L possesses the highest diffusion improvement whereas the least diffusion enhancement was seen for PtBF-S. These results suggested that in the range of our experimental conditions, a large coating amount of Pt would have higher self-propelled speed in diluted H_2O_2 solution.

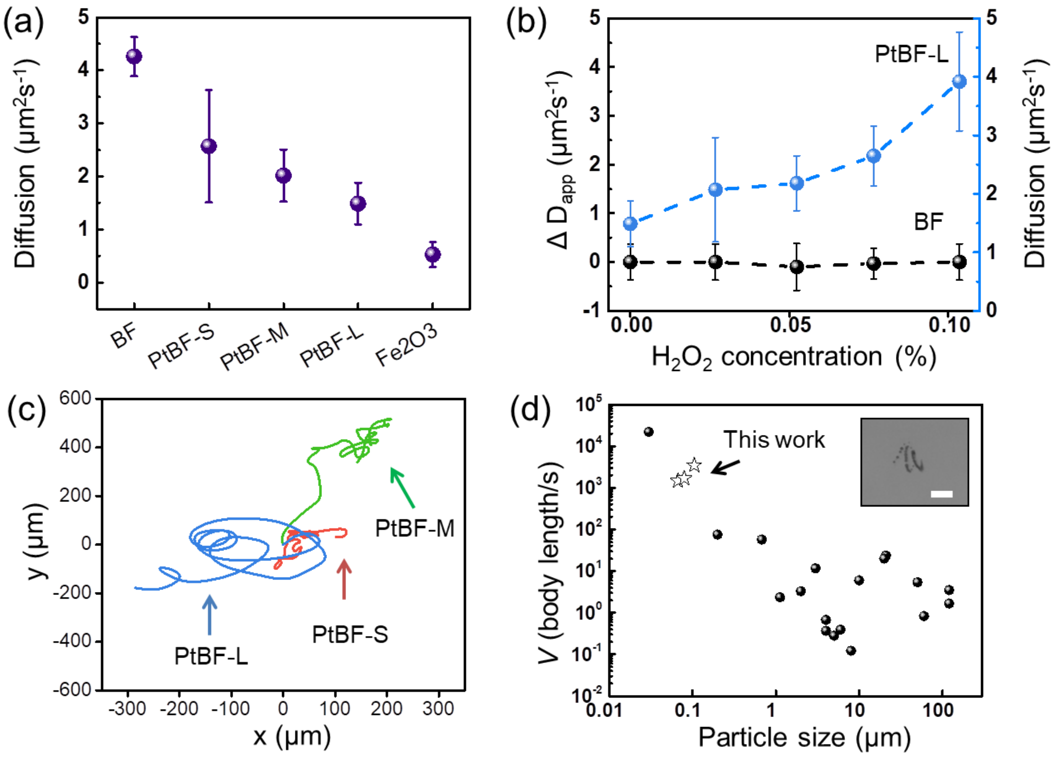

Figure 21. Self-propelled behaviors of PtBF platelets.

We found this trend even applied at relatively high concentration of H_2O_2. Upon increasing H_2O_2 to higher concentration (4 wt%), we employed optical microscopy to track the bubble path to estimate the trajectories of nanomotors. As shown in Figure 21c, the optical tracking of self-propelled nanoparticles (t = 22 s) revealed the highest ballistic trajectory for the PtBF-L. The average speed of PtBF-S, PtBF-M, and large PtBF-L were estimated to be 5700, 5800, 11500 body length/s, respectively. In addition, we compared our results with the reported works, as shown in Figure 21d (The inset showed a typical motion of PtBF-L in H_2O_2). These results suggested that the conventional self-propulsion with enhanced diffusion can also be effective for two-dimensional motors at the nanoscale, and such catalytically active behaviors of PtBFs, particularly PtBF-L, might be useful for environmental clean-up of organic pollutants.

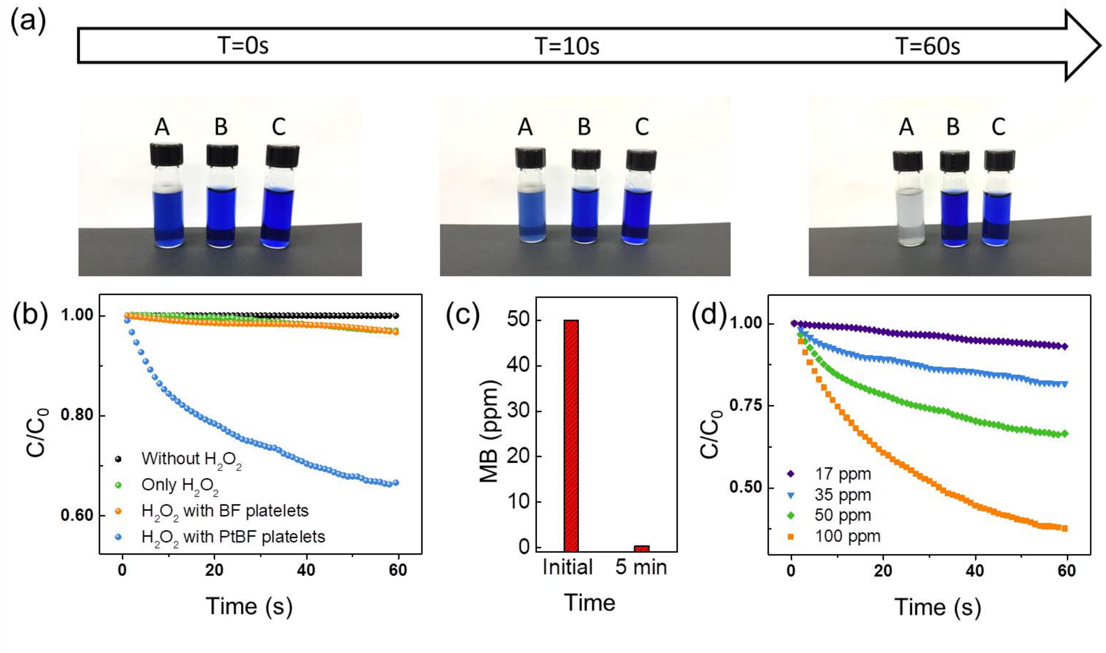

Figure 22. Catalytically active behaviors of PtBF-L to remove MB in water.

As a proof-of-concept example of self-propelled nanomotors for environmental applications, the catalytic performance of PtBF was demonstrated. Studies have shown that both Fe^{3+} and noble metal can promote the oxidative decomposition of organic dyes in presence of H_2O_2, leading to the clean-up of wastewater.[176, 190] Here, we use methyl blue (MB) as a model system for polyromantic contaminators due to its wide existence in dye industry. Compared with non-active BF (Figure 22a, sample B) and H_2O_2 solution (Figure 22a, sample C), the self-propelled PtBF demonstrated a more efficient capability in catalytically oxidizing MB. To quantitatively demonstrate that PtBF can accelerate the decomposition of MB, time-collapse UV-vis spectra of control experiments were performed. As shown in Figure 22b, the MB concentration remained relatively high when H_2O_2 or BF was used. In presence of 4% H_2O_2, the MB decomposes slowly with time (green dots), while the pristine BF nanoparticles could slightly catalyse this process in 0-30s, and then shows a similar decomposition rate as pure H_2O_2. Upon adding PtBF, a clear decreasing trend of MB concentration was observed. In 60s, the PtBF NPs can significantly reduce the concentration of MB by 34%, which is more than 1000% larger than pure H_2O_2 (2.99%) and BF (3.28%). After 5 min, 99.4% of MB was removed from the solution. The enhanced microconvection by PtBF at high speed may contribute such excellent decontamination efficiency by increasing the chance of contact between oxidative species and MB. In addition, we found our nanorobots can perform effectively under a wide range of contaminant concentration without showing inhibition from high concentration of MB. The percentage of MB removed from solution increased significantly with initial dye concentration, which was consistent with Fenton's reaction of other dye systems,[191] indicating high stability of PtBF nanorobots.

3.2.4. Conclusion

In summary, a two-dimensional catalytic nanomotor based on magnetic BF nanoparticles was prepared. We demonstrated that self-propulsion behaviors are not limited to 0D nanospheres and 1D nanorods, but are also applicable to 2D nanoplatelets. The enhanced diffusion of BF-based nanomotors with different Pt thicknesses were also evaluated, and the large amount of Pt showed more efficient in converting chemical into speed. The surface chemistry of PtBF was investigated by XPS and the 2D structure was confirmed by TEM and AFM analysis. In consequence of the 2D nanoscale structure of PtBF, the nanomotor not only catalyzes the decomposition of free organic dye in solution over a wide range of pollutant concentrations, but also shows excellent catalytic performance in removing adsorbed pollutants with good recyclability due to the magnetic nature of BF. The present approach is straightforward and possibly applicable to other 2D materials, indicating strong potential for a wide range of applications such as water treatment, nanoscale cleanup, and catalytic chemical reaction.

CHAPTER IV

ISOTROPIC-SMECTIC PHASE TRANSITION OF ZRP NANOPLATES

4.1 Background

In nature, many animals use periodical microstructures in scales, dermis or feathers to demonstrate brilliant iridescent colours, which allow adaptive camouflage, warning signal, and sexual selection[192-194]. For examples, Japanese jewel beetles display various structural colours by precisely controlling the interlayer distance of plate-shaped particles. Inspired by nature, structural colors have been realized from ordered architecture of 0D nanospheres[195], 1D nanorods/nanotubes,[196] 2D nanodisks[197], and 3D nanoparticles[198]. The control of such remarkable structural colors plays a crucial role in many practical applications, including responsive film in sensoring[199], photonic paint in solar cells[200], and anticounterfeiting techniques in inkjet printing[201]. A comprehensive control over structural coloration, especially in complex geometry, is of great importance. In contrast to 0D nanospheres, 2D nanosheets have size distribution in particle diameter as well as particle thickness, which makes the formation of structural ordering challenging. Recent advances in self-assembly of nonspherical colloids have been made by controlling concentration, salinity, and external fields, leading to a fascinating variety of photonic crystals[14, 202-205]. However, the size effect on colours of colloidal suspension has rarely been discussed under this context, and an approach that manipulates photonic colors using geometrical factors, *i.e.*, size, is missing. Our previous works have shown the ability of TBA exfoliated ZrP undergoing I-N transition which could be strongly influenced by the size and polydispersity.[206-207] It will be interesting to determine whether the size can also play a significant role in defining the colourations of photonic crystals, considering the similar nature of colloidal self-assembly of ZrP nanosheets.

In this work, we used modified one-pot strategy to exfoliate layered α-ZrP in acetonitrile[208] to study the size effect on colouration of discotic photonic crystals. We studied the phase diagrams of Jeffamine exfoliated ZrP (ZrP) which undergoes a disordered isotropic phase to ordered smectic phase transition. Taking advantage of size segregation driven by gravity sedimentation, we achieved different size of ZrP which clearly indicates the size-dependent structural colours. As is demonstrated later, we thus employed striking colours of charged nanosheets as unique fingerprints to follow the Kirkwood - Alder transition in the evolving systems and unravel their complex dynamics in real time.

4.2 Synthesis of ZrP nanosheets

In a typical procedure, α-Zirconium phosphate (ZrP) was prepared by the hydrothermal method. Specifically, 6.0 g of zirconyl chloride octahydrate ($ZrOCl2 \cdot 8H2O$) was mixed with 50 mL of 12 M phosphate acid. The gel-like mixture was then loaded in a 100-mL PTFE container followed by heating for 30 hours at 200 ℃. The product was washed with deionized water three times, dried in the oven, and stocked for later use. Scanning electron microscopic (FEI Quanta 600 FE-SEM) and transmission electron microscopic (JEOL JEM-2010 TEM) characterizations were used to observe the morphology of the ZrP. Larger ZrP platelets (L-ZrP) were prepared using 50 mL of 15 M phosphate acid to react with $ZrOCl_2 \cdot 8H_2O$ (6g), while hydrothermal condition is 24 hours at 200 ℃. For comparison, smaller ZrP platelets (S-ZrP) were synthesized using 12 M phosphate acid (50 mL) to react with $ZrOCl_2 \cdot 8H_2O$ (6g) for 24 hours at 200 ℃. Purification procedures remain the same for L-ZrP and S-ZrP.

During exfoliation step, 2.0 g α-zirconium phosphate was dispersed in 80 mL acetonitrile followed by dropwise addition of 13.3 ml Jeffamine M-1000 solution (0.5 g/mL in acetonitrile). The mixture was exfoliated under stirring for 5 days, then centrifuged for 30 min at 4000 rpm to remove unexfoliated ZrP. The final product was obtained by further washing with extra acetonitrile to remove excess Jeffamine. Different sizes of exfoliated ZrP nanosheets were achieved using controlled ultrasonication (VWR Ultrasonic Cleaner, MODEL 50T). Upon using different sonication time (10 min, 1h, 2h, and 4h), the average lateral size of the nanosheets was controlled over a very wide range (0.583–1.024 µm).

The volume fraction for the ZrP suspension was calculated as follows: First, a certain volume (V1) of ZrP suspension with mass of M1 is weight out. Second, the dried ZrP is obtained as M2 by evaporating the solvent at 65 ℃. Next, we estimate the volume of solvent V2 being equal to M/ρ, where the mass of solvent M is equal to (M1-M2) and ρ is the density of acetonitrile. Finally we obtained the ZrP volume fraction ϕ which is equal to (V1-V2)/V1.

4.3 Soft photonic crystals of ZrP

When the elytra of jewel beetle are observed under different viewing angles, the body possesses various metallic appearances (Figure 23a). Such angle-dependent color is crucial to the survival of beetles, helping them to hide from predators by mimicking tree leaves while being visible to other beetles for mating purpose. Studies suggest that the iridescent colors originate from the multilayered structure of jewel beetles.[209] According to modified Bragg's law, the multilayered structure of jewel beetles allows the maximal scattering colour at wavelength of $\lambda_{max}= 2(d/m)(n^2-\sin^2\theta)^{1/2}$, where d is the lattice spacing, m is the order of the Bragg reflection, n is the average refractive index of the suspension, and θ is the viewing angle.[14, 203] With an increasing angle of illumination, a shift of scattering wavelength λ_{max} to short wavelength can be expected. As shown in Figure 23b, an analogous colour change is seen in nanosheet colloidal suspension which exhibits a rainbow of colours from red to green to blue by simply adjusting angle of incidence θ and nanosheet concentration ϕ. Given that amorphous photonic crystals exhibit a rather weak dependency on the viewing angle[210], a good layer-to-layer periodicity in ZrP suspension was expected. Owing to its multilayered superstructure, the photonic nanosheet suspension not only mimics the brilliant appearance of jewel beetles at multiple regions, but also simulates the unique behavior, *i.e.*, the angle dependency of structural colors.

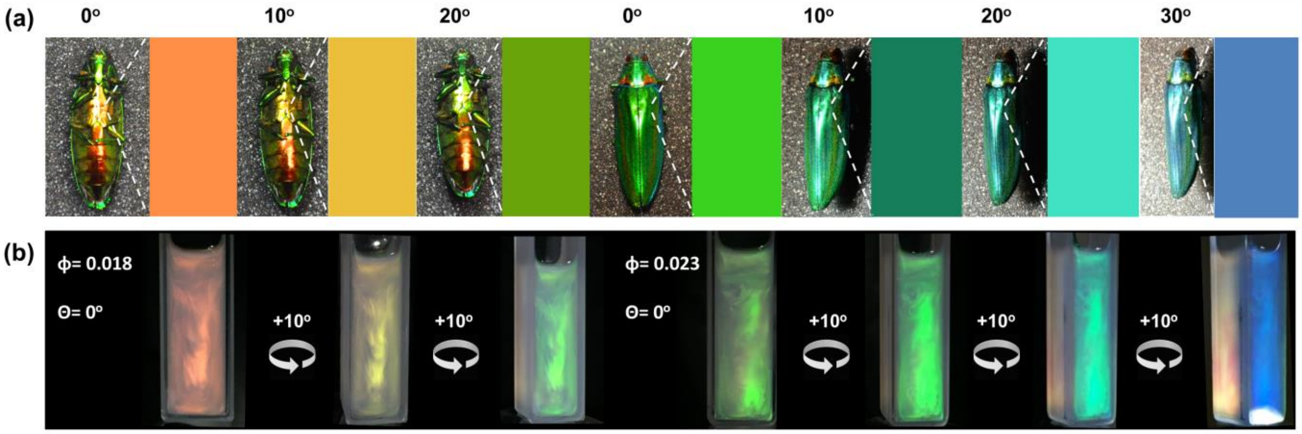

Figure 23. Colloidal nanosheets resembling the colours of jewel beetles *Buprestidae*.

We next investigated the microscale structure of nanosheet system by using the small-angle X-ray scattering (SAXS) techniques. As shown in **Figure 24a**, 2D SAXS images of samples with various vol% ZrP nanosheets present strong anisotropic patterns, indicating a well-ordered structure. In general, the iridescent colours of liquid crystalline materials come from periodical structure of ordered phases such as columnar[205], smectic[208], and chiral nematic phases[204]. **Figure 24b** shows the Kratky plot in which scattering curves demonstrate highly sharp peaks at large volume fraction, excluding the existence of nematic phase.[211] In addition, a number of clear and well-defined peaks of higher order are found, having a 1:2:3:4 relation in q value, indicative of lamellar and smectic ordering. By contrast, for a hexagonal columnar liquid crystal, peak positions with a $1:\sqrt{3}:\sqrt{4}:\sqrt{7}$ q-ratio would be expected.[211-212] Thus, these results indicates that ZrP nanosheet belongs to smectic phase which has large two-dimensional layers periodically stacked after each other. The layers are orientated over the whole crystal domain, as can be concluded from the very anisotropic 2D-scattering pattern and the appearance of several sharp higher order peaks. The interlayer distance, d, calculated from the q(001) value as $d = 2\pi/q(001)$, is 73 nm at volume fraction of 0.072, which is significantly larger than the thickness of the nanosheet (L = 8.8 nm) due to the long-ranged electrostatic repulsion.

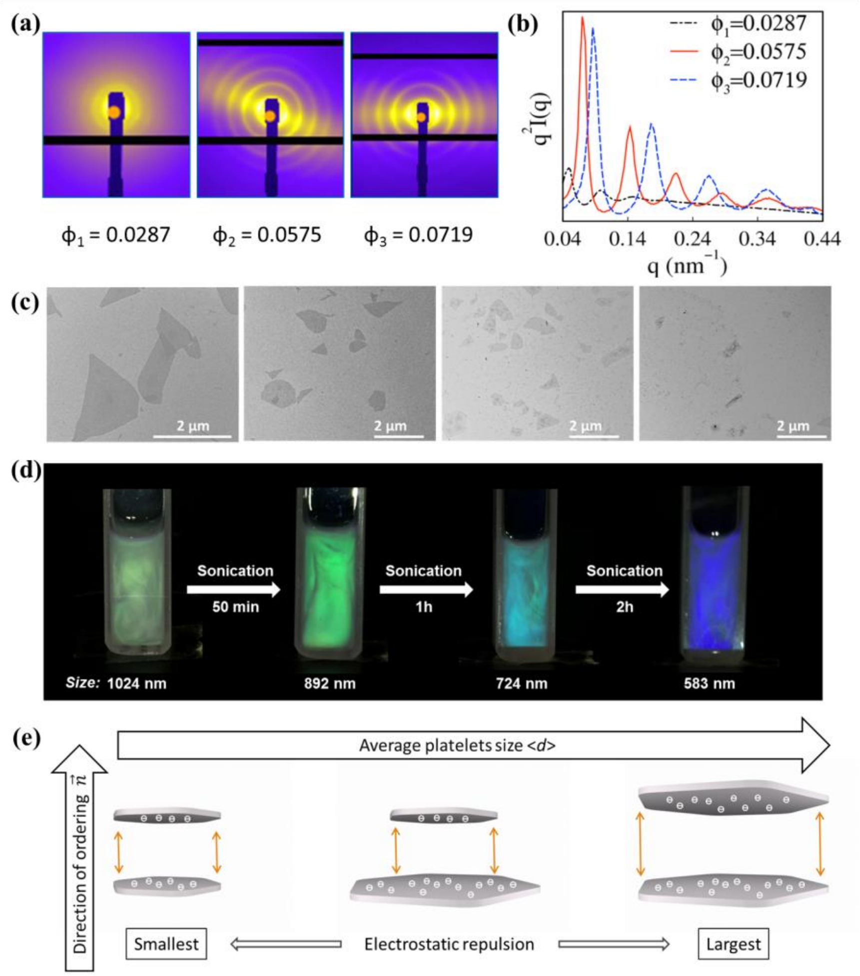

Figure 24. Size-dependent photonic colours of colloidal platelets.

The brilliant structural colour of 2D ZrP nanosheets is reminiscent of photonic colors of 0D materials, *e.g.*, SiO_2 nanospheres and polystyrene nanoparticles, commonly known to be highly depend on the particle sizes.[213-214] Upon increasing the particle size, a wide variety of colours can be achieved. Therefore, two open questions arise: (1) Would the 2D nanosheet, *i.e.*, ZrP monolayer, follows the same trend that particle size dictates the structural colours? (2) If so, given that lateral size is not in the direction of smectic ordering, why does the structural colour depend on ZrP lateral size? To investigate the size effect on structural colour, we took a "paper cutting" strategy to prepare colloidal nanosheets with different lateral sizes. Taking advantage of strong shear forces induced by controlled ultrasonication, a wide range of nanosheet sizes were achieved (Figure 24c). As the exfoliated ZrP monolayer share the identical thickness, we assume that only lateral size changes during sonication. Upon increasing the sonication time, nanosheet suspension underwent a clear blue shift from yellowish green to dark blue (Figure 24d). UV-Vis spectra further confirm the colour shift of ZrP suspension measured at normal incidence, presenting characteristic peaks of 559 nm, 524 nm, 493 nm, and 460 nm upon decreasing nanosheet sizes. The size and polydispersity (σ) of the nanosheets were determined using dynamic light scattering (DLS). As there are no salts or extra nanosheets introduced during ultrasonication, the connection between the size change and the color shift is obvious. In our system, electrostatic repulsive interaction is favored, and plays a crucial role in determining the d-spacing of nanosheets as Debye screening is suppressed in polar aprotic solvents.[211] Given that the charge density is almost constant, the surface charge per particle dramatically decreases when nanosheets were breaking down into small pieces. This is the first observation that the size-dependent coloration of 0D photonic spheres can be generalized for 2D photonic platelets, though throughout a new mechanism.

Although both 0D photonic spheres and 2D photonic platelets share similarities, *i.e.*, size-dependent colours, differences do exist. Despite the high polydispersity ($\sigma > 0.24$), our photonic nanosheets show brilliant structural colors whereas it is very rare to see structural colors for 0D photonic spheres even if moderate polydispersity occurs. Such wide size distribution was also observed in photonic suspension of graphene oxide and TiO_2,[14, 203] while few discussion has been made with regard of dimensional factors. Therefore, we study the size distribution effect on nanosheet smectic color by a vertical fractionation method, widely used to separate particles with different size from a polydispersed sample.[205, 215] Specifically, a concentrated mother suspension of ZrP nanosheets was diluted with dry acetonitrile into borosilicate glass, followed by gravity-driven phase separation for a few days to several months. It is worth noting that the concentrations of ZrP should be in the range of approximately isotropic-to-smectic coexisting phases to ensure the successful fractionation. During the fractionation, the larger nanosheets would have tendency to settle at the bottom, while the nanosheets with smaller size would remain in the fluid phase[207]. In addition to size segregation, liquid crystalline phase separation occurred simultaneously: a colorful smectic phase would settle at the bottom driven by gravity sedimentation, while the transparent isotropic phase would move to the top, as it is less dense than the smectic phase (Figure 25b). In addition, we employed freeze-drying scanning electron microscopy (FD-SEM) to monitor phase separation process. FD-SEM images of fractionated sample reveal that porous sponge-like structures in fluid phase which are almost perfectly random. This is in complete contrast to the lamellar structure of smectic phase with clear periodicity, which well explained the colour only existing in liquid crystal phases. Interestingly, we observed that the colors of smectic crystals vary when a metastable suspension phase-separates into coexisting crystalline and fluid phases. Surprisingly, such changes of colors in coexisting samples is in contrast to 0D photonic spheres which exclusively show identical color in coexisting concentrations in multiple systems, from near hard spheres PMMA to charged spheres SiO_2.[214, 216]

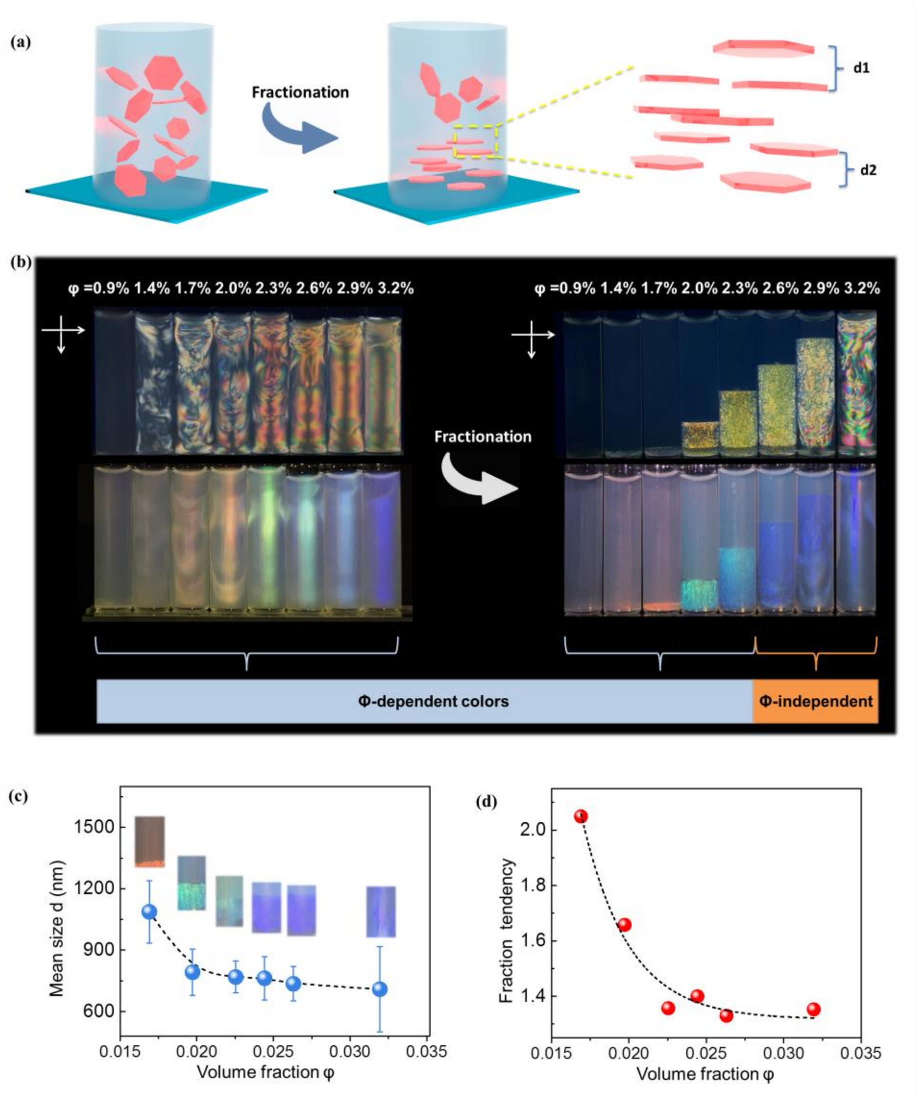

Figure 25. **Distinguishing colour driven by controlling size distribution.**

Although the colloidal crystals reflected light at a frequency that varies in the range of $\phi=0.017$ to $\phi=0.026$, the reflected colour remains almost unchanged at higher volume fraction ($\phi>0.026$). As a result, we proposed a charged nanosheet model that accounts for the various colours observed in coexisting phases. In a coexisting sample with red colour, the relatively low volume fraction only renders large nanosheets nucleate and form smectic crystal in the bottom, while small and middle size ZrP nanosheets still remain in the isotropic phase. Due to surface electrostatic interaction, charged nanosheets with large diameter tend to build higher layer-to-layer distance in comparison with small nanosheets, in agreement with the recent theoretical and experimental studies.[14, 213, 217-218] By increasing the volume fraction of ZrP nanosheets, there will be decreasing number of small and middle size nanosheets, as the mother suspension is dominant by large size nanosheets. Thus, the packing fraction also increases, leading to lower d-spacing smectic crystal with a "blue-shift" colour. It was found that there is a clear decreasing trend of average size when rising up volume fraction (Figure 25c). This is likely due to fractionation tendency which highly depends on nanosheet concentration, as shown in Figure 25d. The fractionation tendency is defined as the segregation extent of size, i.e. the plate-size ratio of smectic to isotropic (see further discussion on fractionation in Supporting Information). As the volume fraction of ZrP increases, the tendency of nanosheet fractionation was suppressed, and thus the size of fractionated ZrP nanosheet plateau at volume fraction $\phi=0.026\sim0.032$, leading to the almost identical colours in smectic crystals even at different volume fraction. This unique behaviour of our fractionated ZrP particles highlights the difference from unfractionated ZrP which highly depends on the concentration.[208] These results confirm that the size-dependent colouring mechanisms are not limited to spherical photonic crystals, but are also applicable to 2D particles, even at high polydispersity.

In conclusion, we demonstrated the ability to engineer the molecular interaction of 2D colloids by manipulating the first order transition of isotropic to lamellar phase such that an on-demand control of photonic bandgap of polydispersed nanosheet suspensions can be readily achieved. The novelty of our results lies in several reasons. First, the method for assembly of 2D colloids using phase transitions was established as a promising model strategy to manipulate the structural properties of soft materials. This is complementary to existing methods of assembling anisotropic colloidal systems. Second, we have demonstrated that particle dimensional factors and electrostatic interaction play essential roles in phase evolutions of colloidal nanosheet, as has been proposed by theories[207]. Tuning aspect ratio and electrostatic interaction of 2D colloids enables the manipulation of phase diagrams with positional order. Finally, we were able to tailor the phase behaviours of colloidal nanosheets and achieved a wide range of photonic colours, which in turn help to understand the phase diagram of ZrP nanosheets. For the first time, the synergetic effects of phase transition and size manipulation was employed to precisely control the highly ordered self-assembly of 2D nanosheets in dispersions, and we expect that our research heralds the fabrication of the hierarchical structure of 2D materials in soft polymer matrix that might exhibit intriguing optical and mechanical properties[219].

CHAPTER V

SURFACE-ENGINEERED 2D MEMBRANES

5.1 High-flux separating membrane

5.1.1 Background

Oil contaminated wastewater from petrochemical industries and oil spills has been plaguing the earth for decades by causing serious environmental issues.[220-221] For example, polycyclic aromatic hydrocarbons and other oily chemicals in wastewater pose a potential risk to aquatic ecosystems as their decomposition causes excessive oxygen consumption, which leads to an increased mortality rate in fish populations.[78] Therefore, the challenge of effective oil–water separation has been highlighted. Conventional oil-water separation methods, including gravity separation, air flotation, coagulation, and de-emulsification, have inherent disadvantages such as low efficiency, high energy consumption, and recontamination problems.[79-82] Separation of oil and water is essentially an interfacial science problem, and thus new strategies based on unique wettability materials have shown to be effective and advantageous.[83-84]

Materials with surface-active features, such as superhydrophilic or hydrophobic coating, have attracted great attention.[67, 83-84, 153, 222-228] By carefully controlling surface chemistry and

---

Parts of this section are reprinted with the permission from ACS publishing and RSC publishing: 1) Zeng, M.; Wang, P.; Luo, J.; Peng, B.; Ding, B.; Zhang, L.; Wang, L.; Huang, D.; Echols, I.; Abo Deeb, E.; Bordovsky, E.; Choi, C.-H.; Ybanez, C.; Meras, P.; Situ, E.; Mannan, M. S.; Cheng, Z., Hierarchical, Self-Healing and Superhydrophobic Zirconium Phosphate Hybrid Membrane Based on the Interfacial Crystal Growth of Lyotropic 2D Nanoplatelets *ACS Applied Materials & Interfaces* **2018**, *10* (26), 22793–22800. Copyright (2018) American Chemical Society. 2) Zeng, M.; Echols, I.; Wang, P.; Lei, S.; Luo, J.; Peng, B.; He, L.; Zhang, L.; Huang, D.; Mejia, C.; Wang, L.; Mannan, M. S.; Cheng, Z., Highly Biocompatible, Underwater Superhydrophilic and Multifunctional Biopolymer Membrane for Efficient Oil–Water Separation and Aqueous Pollutant Removal *ACS Sustainable Chemistry & Engineering* **2018,** *6* (3), 3879-3887. Copyright (2018) American Chemical Society. 3) Zeng, M.; Peng, B.; Ybanez, C.; Tan, N. W.; Deeb, E. A.; Bordovsky, E.; Choi, C.-H.; Echols, I.; Nguyen, A.; Ye, A.; Dendumrongsup, N.; Zhang, L.; Huang, D.; Wang, P.; Luo, J.; Situ, Y.; Cheng, Z., High-flux underwater superoleophobic hybrid membranes for effective oil–water separation from oil-contaminated water *RSC Advances* **2017,** *7* (15), 9051-9056.

morphology, fabric,[229-232] mesh,[233-236] foam,[237] and polymeric membrane[238-241] have been fabricated with special wettabilities that enable successful separation of oil and water from oil-water mixture. Recently, Shang and co-workers reported the fabrication of superhydrophobic nanofibrous membranes by electrospinning cellulose acetate nanofibers with an *in situ* polymerization approach. The as-prepared membranes can selectively and effectively separate oil from oil-water mixtures with good stability over a wide pH range. In addition to electrospinning, superwetting materials have also been fabricated by etching,[242] nanoimprint lithography,[243] sol-gel process,[244] phase separation[245], and dip-coating.[83-84, 246] In particular, dip-coating of filter paper has attracted interest due to good processability, low cost, and eco-friendly features. In 2016, Fragouli *et al.* developed a superoleophobic filter paper by a two-step dip adsorption process.[84] The modified filter papers are mechanically reinforced, exhibiting good oil-water separation efficiency for non-stabilized emulsions. Despite some reported studies on coating filter papers, however a comprehensive study of separation behaviors under harsh conditions, such as extreme temperature, is absent, and new surface modification strategies are still desirable.

Herein, we propose a hydrogel-coated superoleophobic filter paper for efficient oil-water separation in complex environments. Taking advantage of the high reactivity of crosslinker tolylene diisocyanate (TDI) with hydroxyl group,[247] we demonstrate that poly vinyl alcohol (PVA) and filter paper can be covalently bonded into a superoleophobic network. For the first time, TDI-based polymer-modified filter paper (PMFP) was proven to separate oil and water successfully, and exhibited excellent oil-water separation efficiency up to 99.2%. Meanwhile, the PMFP also reveals good tolerance to highly acidic, alkaline, and salty environments and a wide range of temperature, making it applicable to practical applications.

5.1.2 Preparation of 2D membranes

The polymer-modified filter paper was fabricated by a crosslinking reaction between PVA and the cellulose network of filter papers where TDI was used as a cross-linker, as shown in Figure 26. In a typical procedure, the pristine filter papers were first immersed in 4 wt% PVA aqueous solution for 0.5 h at ambient temperature. Then, the PVA-treated filter papers were dried thoroughly in an oven at 65 ℃ for 12 h to remove potential surface moisture. Next, 1 mL of TDI solution (0.1 v/v % in anhydrous acetone) was applied on the dried PVA-treated filter paper, allowing the crosslinking process for 24 h at room temperature. Finally, the obtained PVA-coated filter paper was washed with deionized water and acetone several times to remove potential excess PVA or byproducts before use.

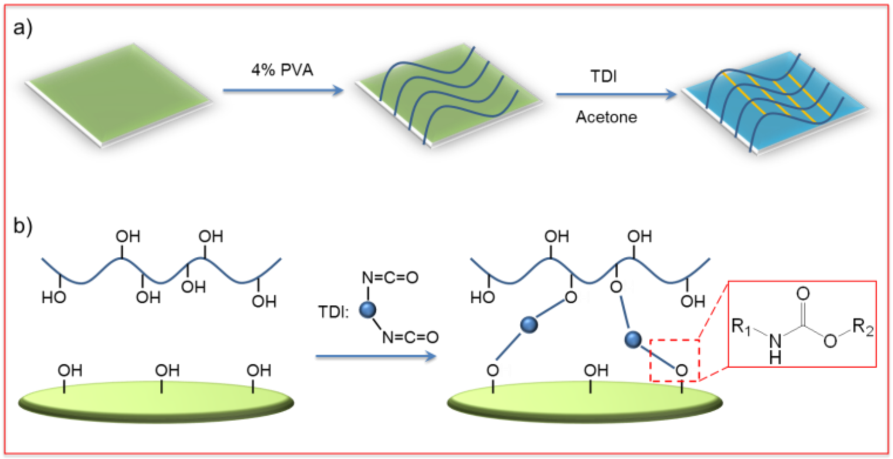

Figure 26. Preparation of 2D membranes.

Oil droplets (dichloromethane dyed with Sudan IV, approximately 5μL) were dropped onto the polymer-modified filter paper under water and allowed to equilibrate for 20 s before making any measurement. To evaluate underwater contact angles under acidic, alkaline, and saline conditions, we used 0.1 M HCl solution, 0.1 M NaOH solution, and 0.1 M NaCl solution as the aqueous phase respectively. A digital camera was used to record the images which were then analyzed by the software package, *ImageJ*. The mean values of three measurements performed on the same sample were adopted as the contact angles.

The separation efficiency was examined by measuring the oil concentration in separated aqueous phase. The oil-water mixtures were carefully poured onto polymer-modified membranes under different conditions where the volume fraction of oil in mixture was fixed at 20 v/v %. A series of oils/organic solvents, including heptane, toluene, ethyl acetate, and crude oil, were used in this experiment. For experiments under different temperature, the oil, water, and separation setup were precooled or preheated to desired temperature before measurements. After the completion of separation, the oil content of the collected water was measured by an infrared spectrometer. Specifically, carbon tetrachloride (CCl_4) was used to extract oils from water, followed by a measurement of absorbance at 2930 cm^{-1}. The oil content of each sample was acquired by calculating the absorbance and the correction coefficient.

The fluxes were calculated by measuring the time for flowing constant volume of feed solutions from the known area of the PMFP. The height of the feed solution was fixed at 7 cm by using a glass tube with an outlet to drain excess solution. 0.1 M HCl solution, 0.1 M NaOH solution, 0.1 M NaCl solution, and deionized water were used to simulate acidic, alkaline, saline, and neutral conditions, in which we measured 20 mL of collected solution for each condition.

The surface chemistry of PMFP was determined by X-ray photoelectron spectroscopy (XPS) analysis on an Omicron's DAR 400 using Mg Kα radiation as the excitation source. The binding energies were referenced to C^{1s} at 284.80 eV. Fourier transform infrared spectroscopy (FTIR) was recorded on a Thermo Nicolet 380 FTIR spectrometer to evaluate oil content. Scanning electron microscopy (SEM) images of pristine filter paper and PMFP were obtained using a field emission scanning electron microscope (JEOL JSM-7500F, Japan). Samples were coated with 5 nm palladium/platinum (20% Pd and 80% Pt) prior to SEM imaging.

5.1.3 The surface characterization of membranes

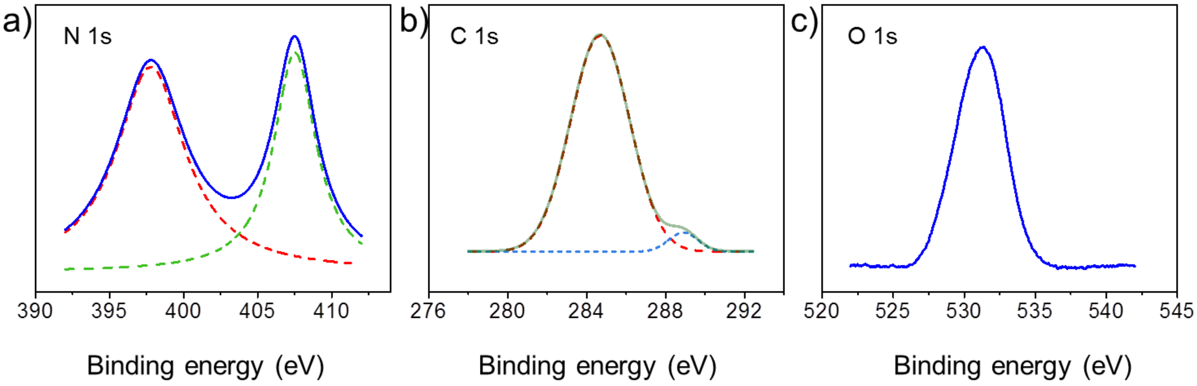

Figure 27. XPS of PMFP.

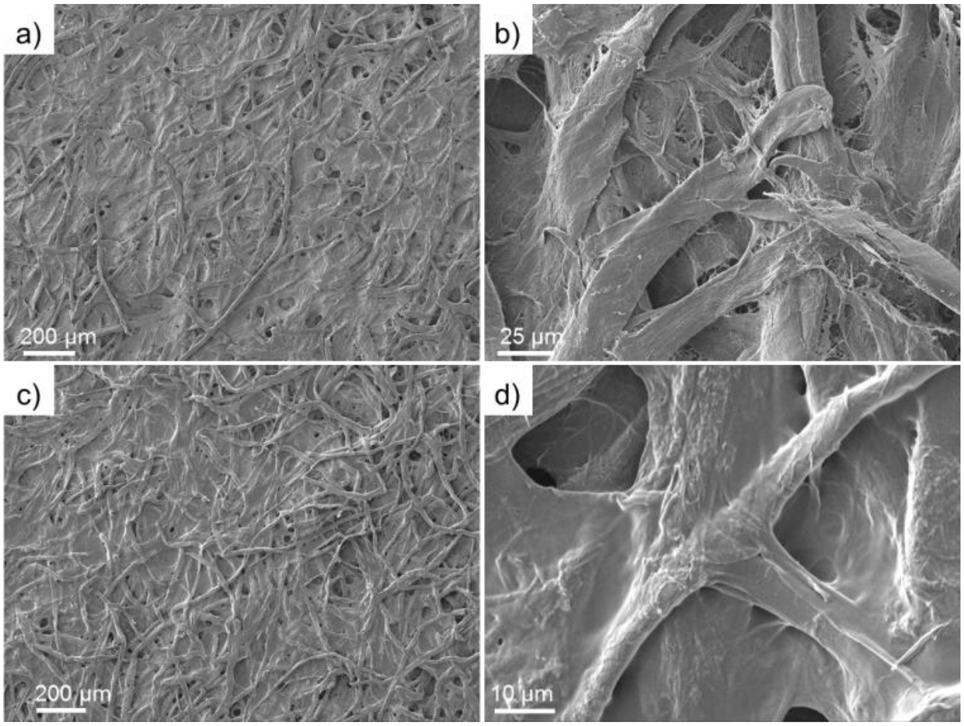

Figure 28. The morphologies of filter papers.

The polymer-modified filter papers were fabricated by a crosslinking reaction between PVA and the cellulose network of filter papers using TDI as a cross-linker. As shown in Figure 26, the pristine filter paper was first treated with PVA, followed by the addition of the TDI solution in acetone. In the first step, the hydroxyl groups of cellulose interacted with PVA only through physical adsorption, such as hydrogen bonding, while a chemically covalent bond had yet to be formed. After adding TDI as the crosslinker, the cellulose network was able to connect with PVA covalently by reacting -OH with the isocyanate groups. This procedure of fabricating polymer-modified filter paper is straightforward and economically efficient, allowing for scale-up production.

To investigate the surface chemistry of modified filter papers, high resolution C^{1s}, O^{1s} and N^{1s} XPS spectra were collected. As shown in Figure 27, the characteristic peaks of binding energy at 284.7, 288.9, 397.8, 407.5, and 531.3 eV were found, which can be assigned to the C^{1s} of C-C bonds, the C^{1s} of O=C-O bonds, the N^{1s} of C-N-H bonds, the N^{1s} of C-N-O bonds, and the O^{1s} of C-O bonds in ethers and hydroxyls, respectively. Elemental analysis of the polymer-modified filter paper was also carried out, revealing a C:O:N atomic ratio of 90:26:1. These results indicated the solid crosslink between PVA and filter paper by TDI.[248-249]

The morphologies of pristine and polymer-modified filter papers were examined by FE-SEM. As displayed in Figure 28, the pristine filter paper shows a porous surface with average pore size around 25 μm. The high magnification of the SEM image reveals a coarse surface with randomly aligned cellulose fibers. Figure 28 reflects the morphologies of filter papers after the crosslinking processes with PVA and TDI. The porous structure still remains with a similar average pore size. After the crosslinking process, however, the original cellulose fiber becomes completely covered by a dense and uniform layer of polymer at the microscale. The as-prepared polymer-modified filter paper reveals a smoother structure, indicating that functionalization of PVA induces a significant change in morphologies. The decrease in surface roughness of polymer-modified filter paper further demonstrates that PVA is successfully coated on the cellulose fiber of the filter paper.

To demonstrate the oil-water separation capacity of PMFP, we studied the wettability of as-prepared filter paper by measuring underwater contact angles of oil droplets. Generally, the more oleophobic a surface is, the larger a contact angle with oil we could expect. In particular, surfaces are called superoleophobic if showing a contact angle θ greater than 150° for organic liquids.[250] As shown in Figure 29, nearly no loss of the oil droplet was observed upon contacting with polymer-modified filter paper, indicating low affinity of PMFP for oil. According to the contact angle measurements, the PMFP presented underwater superoleophobicity with an oil contact angle of $160.3 \pm 2.1°$. Acidic, alkaline, and saline conditions were also examined, exclusively showing large contact angles. These results suggested that the affinity of PMFP for oil droplets is negligible. This can be explained by water molecules becoming trapped in the porous hydrophilic structures so that the oil droplets are repelled from the surface of hydrogel-coated filter paper when the polymer modified filter paper is immersed in water.[83]

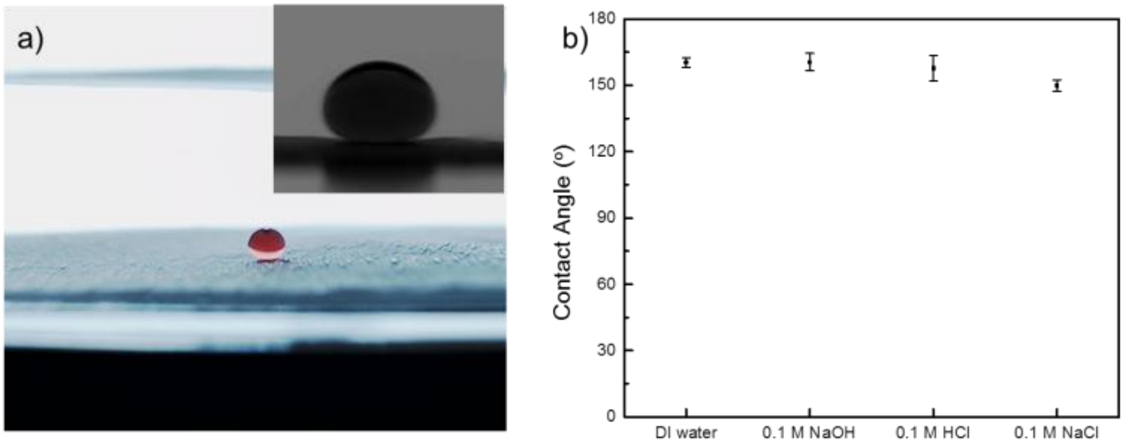

Figure 29. Wettability and contact angles of polymer-modified filter papers.

Separation of oil and water was carried out by directly pouring the oil-water mixture into the filter paper supported by a glass funnel. Heptane was used as the oil phase and the volume fraction of heptane in mixture was fixed at 20 v/v %. The temperature effect on oil-water separation efficiency of PMFP was first examined. At low temperature (2 ℃), room temperature (20^{o}C), and high temperature (65 ℃), water permeated easily, while the heptane was retained above the modified filter paper. No visible oil was observed in the separated water, suggesting good oil-water separation capacity of PMFP. As shown in Figure 30, the separation efficiency of all cases was measured to be >98%, which is comparable to those reported in literature.[224-225, 227] This indicates that the oil-water separation capacity of PMFP will not be strongly influenced by the temperature in the range of 2 ℃ to 65 ℃.

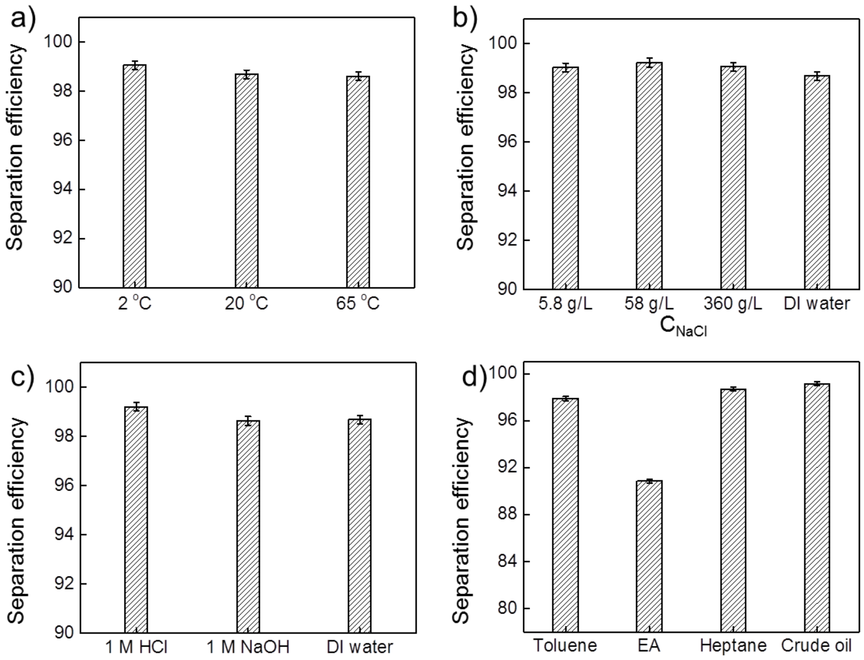

Figure 30. Oil-water separation efficiencies of PMFP under different conditions.

To investigate the performance of filter paper under saline conditions, we used brine solutions as aqueous phases to test oil-water separation efficiency. Under different salinity, polymer-modified filter paper show high efficiency (>98%) as shown in Figure 30b, indicating strong resistance of modified filter paper to high-salinity environments. It is worth noting that polymer-modified filter papers show good tolerance with a high NaCl concentration of 360 g/L which is greater than ten times higher than the salinity of seawater (~35 g/L),[251] suggesting great potential of PMFP for application in oil-seawater separation under typical conditions of offshore locations. The oil-water separation capacity under extreme pH was also investigated. We used 1 M HCl solution and 1 M NaOH solution as aqueous phases while deionized water was used for reference. The oil-water mixtures were successfully separated with high efficiency (>98%), indicating good tolerance of filter paper for acidic and alkaline environments. This high stability of filter paper in acid, alkali and salty water can be attributed to the formation of multiple robust covalent bonds among a crosslinked cellulose network.

Given that wastewater often contains a rich variety of hydrophobic compounds, we examined the capacity of polymer-modified filter paper with different type of oils, including heptane, toluene, ethyl acetate, and crude oil. Those four types of oils are representative: heptane is a hydrophobic long-chain alkane; toluene is aromatic; ethyl acetate is very polar with slight solubility in water whereas crude oil is a very complex mixture of hydrophobic molecules. Owing to the common existence of surfactants in waste water, we simulate oil-water separation by using aqueous phases in presence of 0.5 wt% sodium dodecyl sulfonate (SDS). To ensure the formation of stable emulsions, the samples were emulsified by mixing 0.5 wt% SDS solution and different types of oils using a homogenizer at 1000 rpm. The separation efficiencies of SDS/heptane/H_2O, SDS/toluene/H_2O, SDS/ethyl acetate/H_2O, and SDS/crude oil/H_2O were obtained. It is worth noting that the separation efficiencies are excellent for heptane, toluene, and crude oil emulsions but moderate separation (91%) is observed in ethyl acetate emulsions. Although no visible oil was observed to permeate from the upper emulsions to the collected water phase, the separation efficiency was measured to be just above 90%. This suggests that there is around 10% ethyl acetate remaining in the collected water phase, probably as a solute form instead of an immiscible droplet form. The solubility of ethyl acetate is 8.42g in 100g water at 20 ^{o}C, which is quite consistent with our observation (~9% ethyl acetate in collected water).[252]

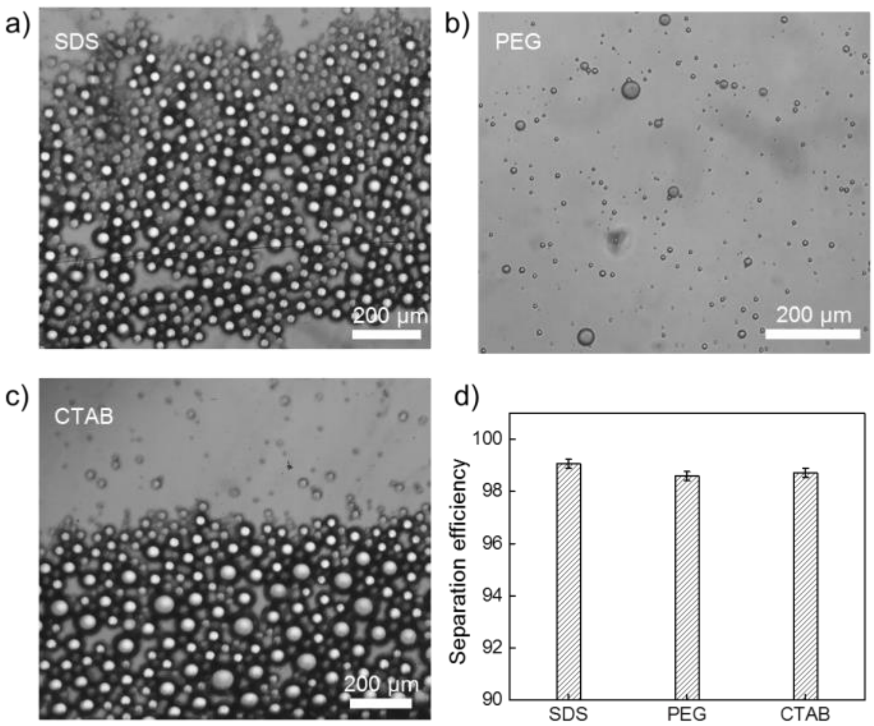

Figure 31. Oil-water separation efficiencies of PMFP with various oils.

To further explore the separation capacity of polymer-modified filter paper, three types of surfactant-stabilized heptane-in-water emulsions were employed. Those surfactants include anionic sodium dodecyl sulfonate, cationic cetyltrimethylammonium bromide (CTAB), and nonionic polyethylene glycol (PEG). As shown in Figure 31, the microscopic images demonstrated the size distribution of heptane droplets in various surfactant-stabilized aqueous solutions, showing that the droplet diameters varied from 2 μm to 50 μm. The PMFP was then used to separate water from surfactant-stabilized oil-in-water emulsions, as shown in Figure 31. Despite the huge difference of droplet sizes among different surfactant-stabilized emulsions, the oil-water separation efficiency are consistently high (>98%) with no visible oil droplets remaining in the collected water. The results indicate strong potential of PMFP for practical application in complex environments.

As a very important parameter for oil-in-water emulsion separation, the flux of various aqueous phases that permeate through the PMFP was also measured. The fluxes were obtained by calculating the time for flowing constant volume of feed solutions from the valid area of the membrane while keeping the height of the feed solution constantly at 7 cm, as shown in Figure 32. We used a glass tube with an outlet to ensure the constant height of tested solutions. In general, all permeates exhibit high fluxes and deionized water possesses higher fluxes than 0.1 M HCl solution, 0.1 M NaOH solution, and 0.1 M NaCl solution. To be specific, fluxes of 4380 ± 184, 3898 ± 48, 3091 ± 235, and 3020 ± 50 L $m^{-2}h^{-1}$ are obtained for deionized, 0.1 M HCl solution, 0.1 M NaOH solution, and 0.1 M NaCl solution, respectively. Those fluxes of polymer-modified filter papers are comparable to that of high flux poly(vinylidene fluoride) (PVDF) membrane.[253] The flux difference among various aqueous samples can be contributed to the viscosity difference as the flux is inversely proportional to the liquid viscosity, and potential swelling effect on the polymer network of PVA under different pH which induces a change in pore size.[247, 254] For acidic, alkaline, saline solutions, the volumetric flux is in the range of 3000–3900 L $m^{-2}h^{-1}$. Although these values are smaller than that of deionized water, they are still considerably high compared to those of commercial filtration membranes, such as an ultrafiltration membrane with similar permeation properties, and which usually gives a flux of less than 300 L $m^{-2}h^{-1}bar^{-1}$.[253, 255-257] Moreover, given that no external pressure was employed in our experiment and the permeation was driven solely by gravity, it is possible that further improvement on volumetric flux of PMFP can be achieved.

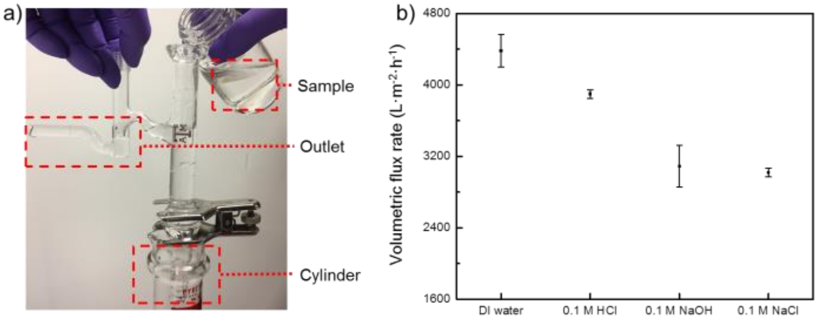

Figure 32. Volumetric fluxes of PMFP under different environments.

5.1.4 Conclusions

The overall results indicate that polymer-modified filter papers not only demonstrate strong potential in oil-water separation for a wide range of conditions, such as high salt concentrations, extreme pH, different temperatures, and oil-water emulsions stabilized by a variety of surfactants, but also show high flux in acidic, alkaline, saline environments. Further research is still desirable to design and build surface-active filter systems to sophisticatedly control the oil-water separation process.

5.2 Bifunctional separating membrane

5.2.1 Background

In contrast to the skin of mammals, there is a layer of epithelial cells on fish skin which produces biopolymers, typically referred to as mucus, in direct contact with aqueous medium.[258-259] Such biopolymer-based superhydrophilic membranes behave as a first line of immune defense against bacteria, high salinities, and temperature changes, allowing fish to survive in a wide range of habitats.[260-261] Inspired by fish skins, artificial functional membranes made from biopolymers have been investigated in recent decades and show great potential for applications such as water purification,[262-263] sensing,[264-265] organ regeneration,[266-268] and food coating or packaging.[269-271] Specifically, synthetic biopolymer membranes with unique wettability have drawn considerable research interests for addressing challenges of oil spills due to the biopolymer's biocompatibility and biodegradability so that re-contamination can be avoided.[272-274] As the cleanup of oil spills is essentially a problem of effective oil-water separation, many efforts have been made to separate oil from oil/water mixtures by using biodegradable biopolymers, including cotton sponges,[275] filter papers,[223, 276] and bacterial cellulose hydrogels.[277] Additionally, crosslinking process has been employed to improve the stability of biopolymer membranes which allows high oil-water separation efficiency at harsh conditions (extreme temperature/pH).[83, 278] Despite the good oil-water separation efficiency of reported membranes, past methods merely based on wettability are not optimized to remove water-soluble pollutants (WSP).[278-279]

In general, WSP (*e.g.*, organic acids) often coexist with oil contaminants (*e.g.*, polyaromatic hydrocarbons) in wastewater.[280-282] Although numerous efforts have been devoted for removing both types of pollutants simultaneously from wastewaters, however, these processes typically involve multiple steps and complex procedures.[280] As shown in **Scheme 1**, the conventional wastewater treatment can be summarized and divided into two main processes: (1) oil-water separation and (2) water-soluble pollutant removal. A successful design of primary filter mainly focuses on oil-water separation efficiency whereas adsorption sites of secondary filter plays a crucial role in the performance of removing water-soluble pollutants. A material that directly unites two processes remains highly challenging, as the oil pollutants could cover and block the adsorption site of the secondary filter, resulting in a declining performance on heavy metal removal. In order to overcome such technical dilemma, a design of membrane with unique interfacial property that shows minimal oil adhesion, *e.g.*, superoleophobic is required. In addition to a superoleophobic surface, a membrane should also form physical/chemical interactions with WSP to adsorb and remove pollutants from aqueous phase.[283] Therefore, developing a novel filtration platform based on new surface-engineering strategies that can effectively remove both types of pollutants is highly desirable.

Konjac glucomannan (KGM) forms part of a family of edible polysaccharides, isolated from the tubers of konjac (*Amorphophallus konjac*), a plant native to eastern and southern Asia.[284-285] Such glucomannan has received tremendous interest owing to its low toxicity, cost effectiveness, and high biocompatibility.[284, 286] More importantly, KGM-based materials have shown interesting binding properties with various types of water-soluble pollutants, including heavy metals,[287] polyphenols,[288] and polyaromatic dyes.[289] It was found that the fascinating adsorption behaviors of KGM originate from the synergistic effects from the hydrogen bonding and the chelating effect of hydroxyl groups. Given that the hydroxyl groups of KGM are hydrophilic in nature, it was anticipated that a surface coated with KGM could be engineered to possess unique wettability, and thus would offer great promise in removing oil-soluble pollutants. Nevertheless, a KGM-based membrane that can eliminate hydrophobic and hydrophilic pollutants simultaneously from wastewater has not been reported. Herein, we aim to demonstrate that the concepts of hydrophilic pollutant removal and oil-water separation can be combined by developing a unique hydrophilic KGM-based membrane.

In this study, we report a bifunctional KGM-modified fabric (KGMF) for effective oil/water separation and aqueous pollutant removal (**Scheme 1**). By using tolylene-2,4-diisocyanate (TDI) as crosslinkers, the KGM-coated hybrid membrane was fabricated by directly coating KGM onto fabrics. We showed that the polysaccharide structure of KGM and the cellulose of fabrics can be covalently bonded into a crosslinked network owing to the high reactivity of TDI with hydroxyl groups. For the first time, KGM-based materials were demonstrated to be underwater superoleophobic, and exhibited excellent oil-water separation efficiency up to 99.9%. After being purified with KGMF, the separated water was used to cultivate and irrigate pinto beans (*Phaseolus vulgaris L.*), whose healthy growth pattern visually confirmed the biocompatibility and effectiveness of our KGM-coated hybrid membrane. Furthermore, the as-prepared KGMF revealed good adsorption of water-soluble pollutants, *i.e.*, polyaromatic dyes and heavy metals, suggesting encouraging potential for treatment of oil-contaminated wastewater in practical world.

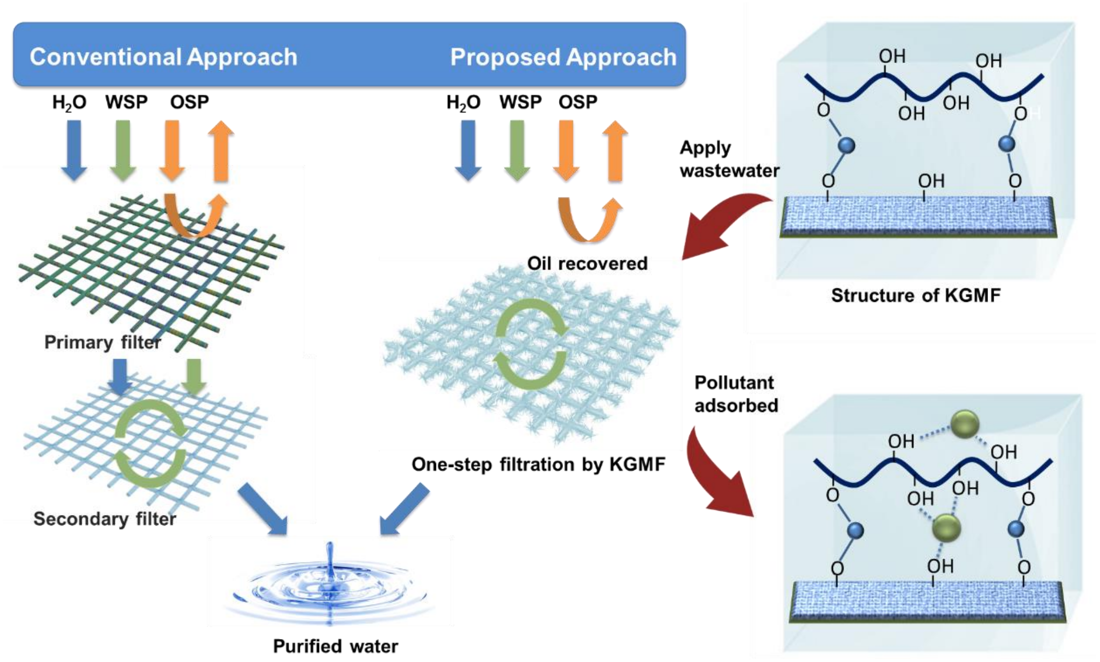

Figure 33. Schematic illustration of wastewater treatment by KGMF.

5.2.2 Preparation of KGMF

The KGMF were prepared by crosslinking konjac glucomannan with fabrics using TDI (toxic!) as a crosslinker. In a typical procedure, 6 ml of 0.5 wt% konjac aqueous solution was applied on both sides of pristine fabrics (2 × 2 inches). After the fabric was dried at ambient condition, it was then coated with 4-ml TDI solution (0.1 v/v% in ethyl acetate), allowing the crosslinking reaction to occur at room temperature overnight. Finally, the resulting fabrics were vigorously washed with DI water to remove excess konjac glucomannan prior to use.

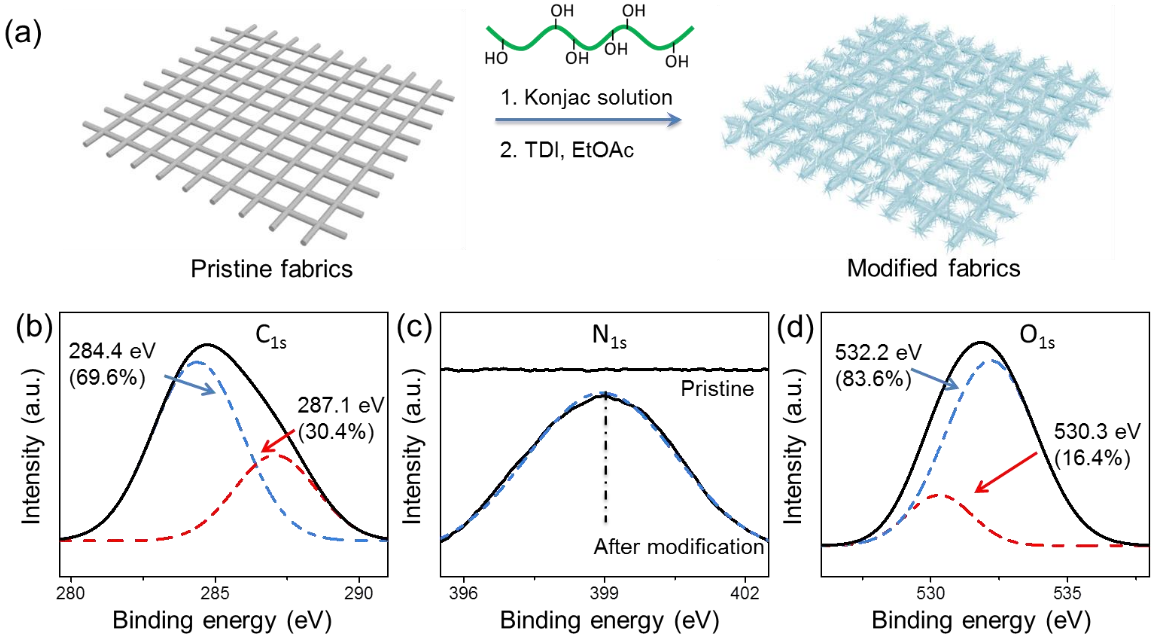

Figure 34. Preparation and characterization of KGMF.

In light of the hybrid structure of fish skins, we synthesized novel biopolymer-coated fabrics in this study. As shown in Figure 33, functionalized membranes were prepared by a direct crosslinking reaction between glucomannan of konjac powder and cellulose of fabrics. In the presence of TDI as the crosslinker, the cellulose structure of fabrics was able to link with glucomannan covalently by reacting -OH with the isocyanate groups. Such structure forms a hydrophilic network for purifying oil-contaminated water. Although the starting material TDI is arguably toxic, the quasi-polyurethane structure of the final product was reported to be innocuous and environment-friendly.[290-291] In addition, the biocompatibility of KGMF was evaluated by bean germination and growth. This method of fabricating biopolymer-modified membranes is facile, straightforward, and economically efficient, making it possible for scale-up production.

To examine the surface chemistry of KGMF, we characterized the samples by X-ray photoelectron spectroscopy (XPS) and FTIR spectroscopy. Figure 34 present the high-resolution C_{1s}, N_{1s}, and O_{1s} XPS spectra of modified membranes, the characteristic peaks of binding energy at 284.4 eV, 287.1 eV, 399.0 eV, 530.3 eV, and 532.2 eV were found, which can be assigned to the C_{1s} of C-C bonds, the C_{1s} of C-O bonds, the N_{1s} of C-N groups, the O_{1s} of C-O bonds in hydroxyls, and the O_{1s} of C=O bonds, respectively. It is clear that the N_{1s} XPS spectra of KGMF show a strong peak at 399.0 eV, whereas there is no noticeable signal for pristine fabrics. According to the XPS spectra, KGMF are composed mainly of carbon, oxygen, and a small amount of nitrogen. In addition, the elemental analysis revealed that the C:O:N showed a molar ratio of 126:40:1. In the FTIR spectrum of KGMF, several characteristic vibrational bands were observed at 1249 cm^{-1}, 1406 cm^{-1}, 1660 cm^{-1}, 2925 cm^{-1}, 3346 cm^{-1}, matching the stretching vibrations of C–O, bending vibrations of C–H, stretching signals of –C=O from amide groups, stretching peaks of C–H of alkane groups, and the stretching vibrations of O–H of hydroxyl groups, respectively.[108, 114] We also performed FTIR of pristine fabrics, whereas the amide peak at 1660 cm^{-1} was missing, indicating that the addition of TDI allowed the formation of quasi-polyurethane structure. Both pristine fabrics and KGMF revealed a broad peak at ~3350 cm^{-1}, confirming the presence of large amounts of O-H groups which are crucial for developing underwater superoleophobic surface. These results verified the successful grafting of biopolymer glucomannan onto fabrics.

We next investigated the morphology of KGMF by field-emission scanning electron microscopy (SEM). Figure 35 present typical SEM images of pristine fabrics, showing individual fibers with diameters in the range of 10–13 μm. In contrast to the “net” structure of KGMF, the konjac powder was observed to be individual particles, which are mostly irregular in shape. Figure 35 reflects the morphologies of membranes after the crosslinking processes with biopolymer and TDI. After the crosslinking process, the surface of fibers becomes covered by a dense and uniform layer of polymer, indicating that functionalization of konjac powder induces a significant change in morphologies. The change in surface morphology of KGMF further demonstrates that biopolymer glucomannan is successfully crosslinked with the fabric network.

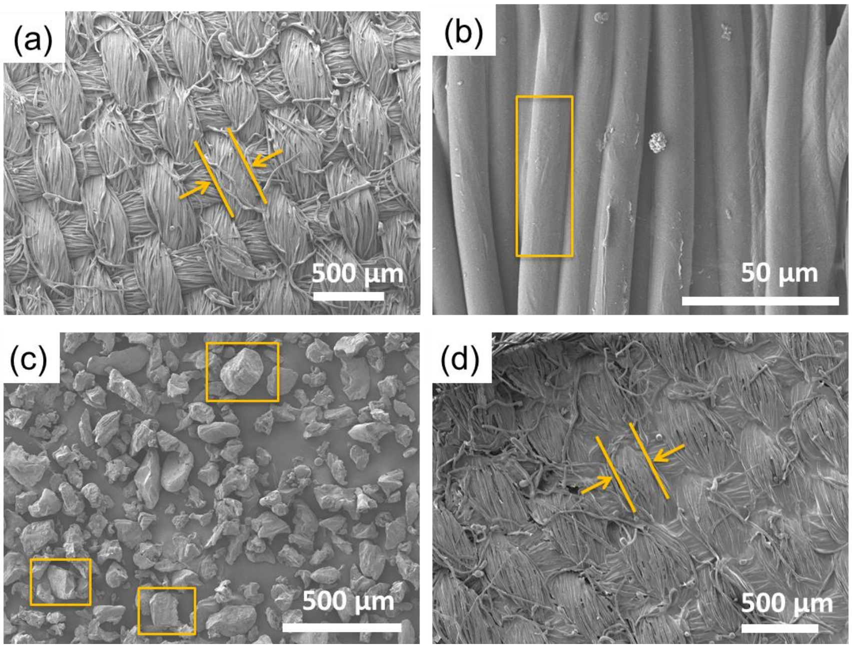

Figure 35. The morphologies of pristine fabrics and KGMF.

5.2.3 Evaluation of oil-water separation efficiency

Oil-water separation efficiency is defined by the weight percent of remaining oil in separated aqueous phase. Specifically, a 5-mL mixture of dodecane (20 v/v%) and aqueous phase (80 v/v%) was directly poured onto the modified fabric supported on a glass funnel. After the immiscible phases separated completely, the aqueous phase was collected and extracted with carbon tetrachloride which was characterized by Fourier transform infrared spectroscopy (FTIR) to quantify the remaining oil concentration. This procedure was carried out using various aqueous solutions to simulate different environments. In addition to DI water, 0.1 M NaCl, 1 M NaCl, saturated NaCl, 0.1 M NaOH, and 0.1 M HCl solutions were used as aqueous phases to evaluate separation efficiency, where the volume fraction of dodecane in oil-water mixtures was fixed at 20 v/v%. Surfactant solution containing 0.25 wt% sodium dodecyl sulfate (SDS) in water was also examined, where the dodecane:water ratio is 1:1.

To demonstrate the potential of hybrid membranes for effective oil-water separation, we studied the wettability of the as-prepared modified fabrics by measuring contact angles (CA) of water and oil droplets. Figure 36 present the wettability of fabrics with deionized (DI) water. When a drop of DI water was placed onto fabric surface, the water drop quickly spreads over the surface with contact angle ≈ 0^o, indicating a superhydrophilic structure of KGMF. On the contrary, a high contact angle was observed when we applied oil drops (dyed red) onto fabric surface under water, showing negligible affinity of KGMF with oil. As the oil contact angle exceeds 150°, the surface can be classified as superoleophobic.[222] According to the contact angles of dichloromethane (DCM), the KGMF exhibits underwater superoleophobicity with an oil contact angle of $161.1 \pm 0.6°$. Such superoleophobic feature of KGMF continues when applied a large drop of oil. To investigate the stability of the modified fabric at ambient environment, we measured the underwater contact angles of oil droplets over two weeks, recording the angle values weekly. As biodegradable materials, KGMF showed a slightly decreasing trend in oil contact angles. It is worth mentioning, however, that the average contact angle remained above 150° throughout the two-week period, which indicates the stability and consistent oleophobicity of the modified fabrics. Such stability of oleophobicity is attributed to the robust crosslinking of cellulose network where isocyanate groups of TDI reacted covalently with hydroxyl groups of KGM.

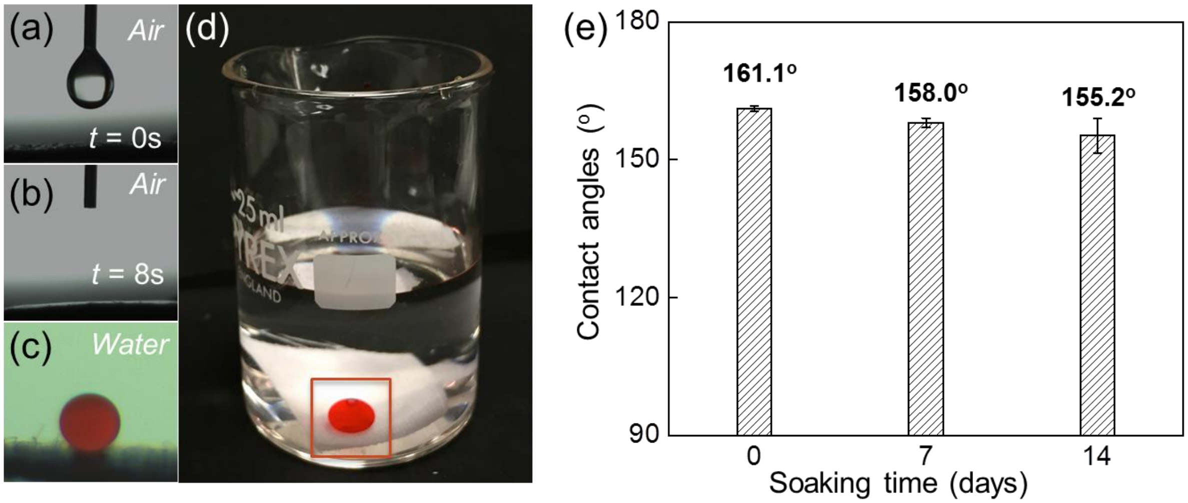

Figure 36. Wettability and contact angles of KGMF.

We conducted the separation of oil-water mixture by directly pouring the mixture onto the KGMF, which was supported on a glass funnel. We used dodecane as the oil phase and various aqueous solutions as the water phase, in which the volume fraction of dodecane was prepared at 20%. During the separation process, the KGMF allowed water to permeate easily, whereas the oil (dyed red) remained on top of the fabrics. As shown in Figure 37, no oil was visible in the collected water, which was then quantitatively analyzed for any oil content by FTIR spectroscopy (see Experimental Section). Given that wastewater often contains a rich variety of compounds, we examined the oil separation performance of polymer-modified fabrics under different conditions, including extreme pH values, high salinities, and exposure to various types of pollutants. We first investigated the oil-water separation capability under extreme pH values. Solutions of 0.5 M HCl and 0.5 M NaOH were used as aqueous phases, while DI water was used for reference. As shown in Figure 38, the oil-water mixtures were successfully separated with high efficiency (>99%), indicating good tolerance of KGMF against acidic and alkaline environments. Similarly, the multiple covalent bonds among a crosslinked polysaccharide network contribute to the excellent stability of KGMF at extreme pH values.

We next studied the performance of KGMF under complex environments, where sodium chloride, sodium dodecyl sulfate, and methyl blue were individually used to simulate aqueous phase in oil-contaminated wastewater. These three types of compounds are representative: NaCl is an ionic salt present in vast quantities in nature; SDS is an anionic surfactant widely used in many cleaning and hygiene products; and MB is a water-soluble dye with multiple aromatic rings, making it a good candidate for studying water-soluble aromatic pollutants. In addition, the blue color of MB can facilitate the visualization of the oil-water separation behavior. Overall, the KGMF demonstrated good oil-water separation efficiency. Due to the emulsification effect of surfactant SDS,[153, 292-293] there were some oil droplets with size too small for KGMF to interact with or withhold, though such tiny oil droplets comprised small volume percentage of overall oil in water. This does lead to a slight decrease in separation efficiency. Although the KGMF did not perform as effectively in the presence of SDS as it did with DI water, the separation efficiency was still considerably high (98.2%) in comparison with previously reported methods.[227, 294]

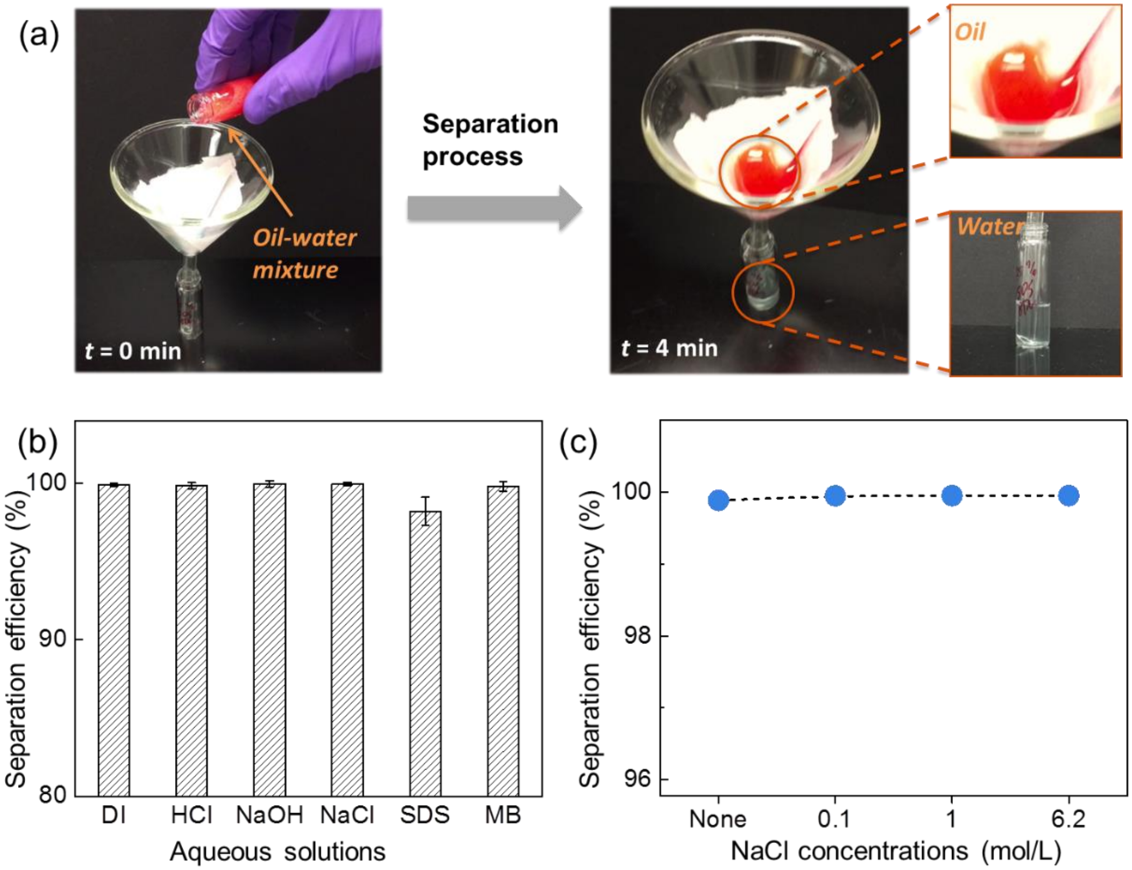

Figure 37. Evaluation of oil-water separation efficiencies of KGMF.

To further explore the separation capability of biopolymer-modified fabrics for treating oil-contaminated seawater, we used multiple concentrations of brine solutions as aqueous phases to test oil-water separation efficiency. Under salinity from 0 mol/L to 6.2 mol/L, KGMF exclusively showed high separation efficiency (>98.5%), indicating strong resistance of KGMF to high-salinity environments (up to a saturated NaCl solution, 6.2 mol/L). This salt-resistant behavior of KGMF is reminiscent of xanthan gum that was specialized for heavy oil recovery in high-salinity reservoir conditions.[295] Both KGM and xanthan gum share a polysaccharide structure, in which salts induce only conformational transitions without introducing aggregation or damaging the hydrophilic network.[295-296] The tolerance of KGMF against a wide range of salinity suggests great potential for applications in oil-seawater separation under typical offshore conditions.

5.2.4 Evaluation of separation efficiency of water-soluble pollutants

The removal efficiency was determined by measuring the pollutant concentration before and after the filtration process. Approximately 5 mL of methyl blue or Rhodamine B (RhB) aqueous solution (60 ppm) was poured directly onto the KGMF, where the filtered aqueous phase was collected. The ultraviolet–visible (UV-Vis) spectroscopy was performed to calculate the concentration difference between mother dye solution and purified water, which was then used to determine the removal efficiency. Similar procedures were used to determine the removal efficiency of dyes for pristine fabrics. For heavy metal ions, 5 mL of Cr^{3+} or Cu^{2+} aqueous solution (10 mM) was poured directly onto the modified fabric, where the filtered aqueous phase was collected. The filtered aqueous samples were then analyzed by UV-Vis spectroscopy to determine the removal efficiency of heavy metal ions. For Cu^{2+} solution, a small amount of ammonium hydroxide solution (28%) was added before the filtration with KGMF to enhance the blue color for better observation. The exact concentrations of Cr^{3+} or Cu^{2+} aqueous solution after filtration through KGMF were determined by inductively coupled plasma mass (ICP-MS) spectrometry.

In recent decades, bioassay, including analysis of seed germination and early growth, has become one of the most popular strategies for monitoring toxic effects of polymers,[297] nanoparticles,[298] and contaminants.[180, 299] An early study conducted by Maila *et al.* showed that the polyaromatic species, such as pyrene, can seriously affect seed germination.[300] Here, we aim to (1) determine the effectiveness of the modified fabric in removing oil-soluble toxins by analyzing the bean germination and growth with purified wastewater *in vitro*; (2) evaluate the biocompatibility of KGMF for plant seeds. During experiments, pinto bean seeds (*Phaseolus vulgaris L.*) were treated with three different water samples: DI water, purified wastewater, and unpurified wastewater. The purified wastewater was prepared by filtering synthetic wastewater through KGMF (see details in Experimental Section), while the synthetic wastewater was directly used as unpurified wastewater. We evaluated the germination of pinto beans by seedling count as well as by the weight of the seedlings over time. The germination was defined as a visible cracking of the seed coat with a measurable root or shoot production.[301-302] The beans were watered and monitored closely for six days. As shown in Figure 38, we observed that the beans treated with purified and DI water both germinated (~100%), whereas only 10% of beans watered by wastewater germinated. These results indicated that the synthetic wastewater had a negative effect on bean germination, and more importantly, the KGMF showed considerable capability for purification of the wastewater.

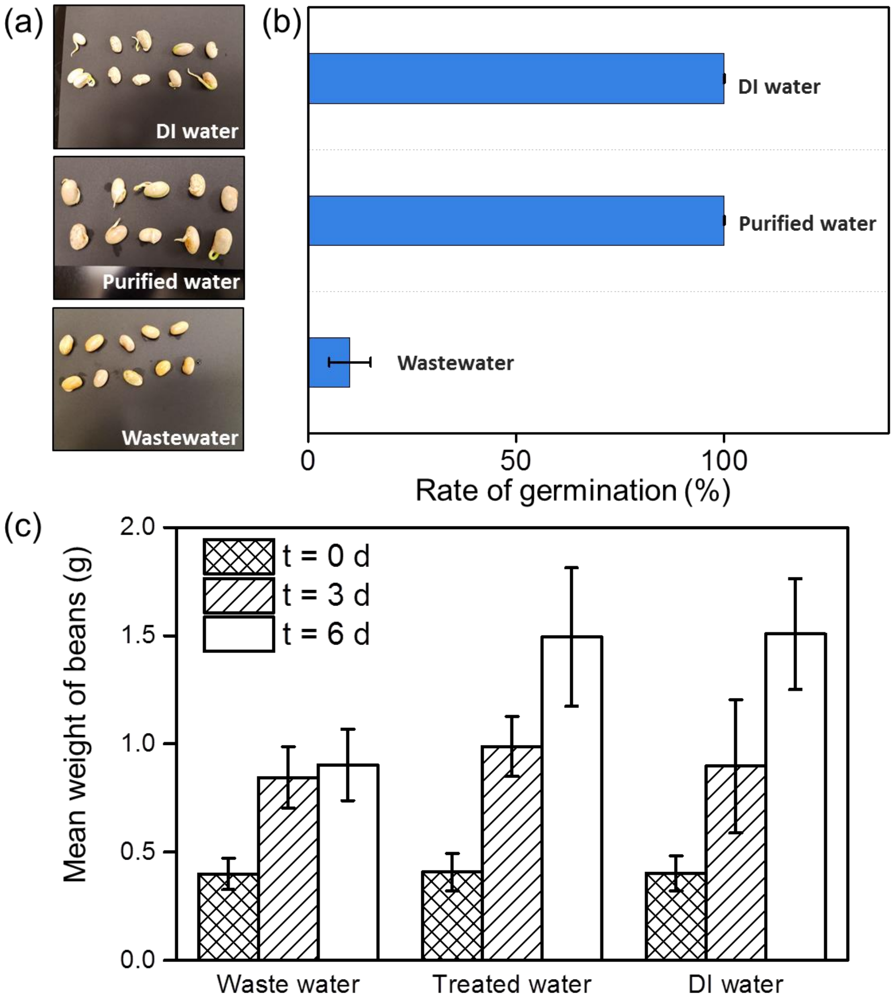

Figure 38. The bioassays of KGMF-purified wastewater using pinto beans.

The measurements of seed weights during the seedling phase can also reveal and quantify the health of pinto beans. Thus, we monitored the average weight of pinto beans every three days, during which the beans were treated daily with DI water, purified wastewater, and unpurified wastewater, respectively. The beans with similar average weight were chosen and studied for their growth. There is a clearly increasing trend of bean weights for DI and purified water groups. Beans irrigated with purified wastewater showed an average weight of 0.99 g with a standard deviation of 0.14 g by day three and grew to 1.49 ± 0.32 g by day six. Meanwhile, beans treated with DI water presented an average weight of 0.90 ± 0.31 g on day three and 1.51 ±

0.26 g by day six. The values of average weights between these two groups of beans are fairly close in the range of sample standard deviations. By contrast, the group of beans treated with wastewater exhibited an average weight of 0.85 g on day three, which is considerably similar to the average weight on day six (0.90 g). It is worth mentioning that although beans treated with wastewater gained weight during the 6-day period, the increase of weight can be attributed to the hydration and swelling of protein and starch inside the beans.[303-305] As very few beans germinated, beans treated with wastewater underwent a much slower growth as compared to the DI/purified water groups.

By comparing these results, it is possible to quantify the effectiveness and environmental friendliness of the KGMF. Since beans treated with KGMF-purified water and DI water have similar trends in germination and growth, it is reasonable to conclude that the fabric was successful in removing oil-soluble contaminants from the synthetic wastewater.

To demonstrate the potential of KGMF for removing water-soluble pollutants, we investigated adsorption behavior of modified fabrics with polyaromatic dyes and heavy metal ions in water. Anionic dye (methyl blue, MB), cationic dye (rhodamine B, RhB), divalent copper (Cu^{2+}), and trivalent chromium (Cr^{3+}) were used due to their high solubility in water and strong colors which allow direct observation of their concentration changes. After applying dye solutions onto KGMF, we compared the dye concentrations before and after filtration using UV-Vis spectroscopy. As shown in Figure 39, it is clear that the MB concentration was significantly reduced due to the adsorption by KGMF. The inset shows photographic images of KGMF after filtration, where substantial dyes were adsorbed on the filter surface. For comparison, cationic dye RhB was also tested and showed a decrease in concentration after filtration with KGMF. The adsorption discrepancy between MB and RhB is determined by their chemical nature, the acid and base character, and the accessibility of dyes to the inner surface of the adsorbent (related to the molecular size of dyes).[306-308] For references, the pristine fabrics were also used and showed only minimal removal efficiency for MB- and RhB-contaminated water.

Figure 39 shows adsorption performance of KGMF in dye-contaminated water at different pH values. Interestingly, we found that the adsorptive behavior of KGMF was highly pH-dependent. For MB, the KGMF exhibited high removal efficiency at pH higher than 7, whereas the optimal adsorption of RhB was observed at pH = 5~7. Past studies have shown that this pH-dependent adsorption behavior is due to the synergistic effect from electrostatic interaction between pollutants and adsorbents, and structure transformation in porosity of adsorbents.[309-310] As pH value increases, the electrostatic repulsion among neighboring ionized hydroxyl groups is enhanced, leading to an increase in porosity of the KGMF structure, which would benefit the adsorptive process.[311-312] A further increase in pH value, however, would also deprotonate the carboxylic group of RhB, resulting in a strong repulsive force to the adsorbent. Despite that the adsorption of MB decreases dramatically at pH=3.0, the removal efficiency, however, remains relatively high: more than 500% than that of the pristine fabrics at pH=7. Additionally, we were able to further increase the removal efficiency of KGMF by increasing the layers of filter. At constant pH value, the increasing layers of filter could slow down the filtration flux rate, allowing additional time for KGMF to interact with dye solution, and thus adsorbing extra dye. The removal efficiency increased upon the addition of a second layer, and then leveled off with any additional layers after the second layer of KGMF.

In addition to the water-soluble dyes, KGMF also demonstrated intriguing adsorptive behavior for heavy metal ions. After applying Cr^{3+} solutions onto KGMF, we analyzed the change in Cr^{3+} concentrations before and after filtration using UV-Vis spectroscopy. UV-Vis spectra showed a sharp decrease at 575 nm for Cr^{3+}, indicating the adsorption of Cr^{3+} onto KGMF. Studies on Cu^{2+} revealed a similar decreasing trend in concentration after filtration with KGMF, suggesting the removal Cu^{2+} from water. As a common quantitative method, ICP-MS spectrometry was also used to determine the removal performance for heavy metal ions. After filtration with KGMF, the concentrations of Cu^{2+} (10 mM) and Cr^{3+} (10 mM) decreased sharply to 3.05±0.64 mM and 4.30±0.43 mM. Since only one layer of KGMF was employed in our experiment and initial heavy metal concentrations are relatively high, it is possible that further increase in removal performance of KGMF can be achieved. Figure 39e showed the proposed mechanism of KGM-based materials' interaction with water-soluble pollutants. For water soluble dyes, the characteristic absorption behaviors of konjac glucomannan originated mainly from the hydrogen bonding of hydroxyl groups of KGM with O atoms of sulfonic groups and with N atoms of tertiary amine groups in pollutants. For Cu^{2+} and Cr^{3+}, the KGMF behaves as a chelating resin or ion exchanger on which hydroxyl groups form chelating interaction with heavy metal ions.[313-314] The 4*s*/3*d* empty orbitals of heavy metal cations accept the free electron pair of oxygen, leading to the formation of chelate bonds. This interaction becomes more favored in the presence of multiple neighboring -OH groups inside the KGMF cellulose network. The overall results confirm the capability of the modified fabrics for the purification of dye contaminated water by interfacial adsorption. The demonstrated strategy of incorporating biopolymer into the textile offers a new path to prepare multifunctional, cost-efficient, and environment-friendly membranes for a wide range of applications, including wastewater treatment, enhanced oil recovery, and clean-up of oil spills.

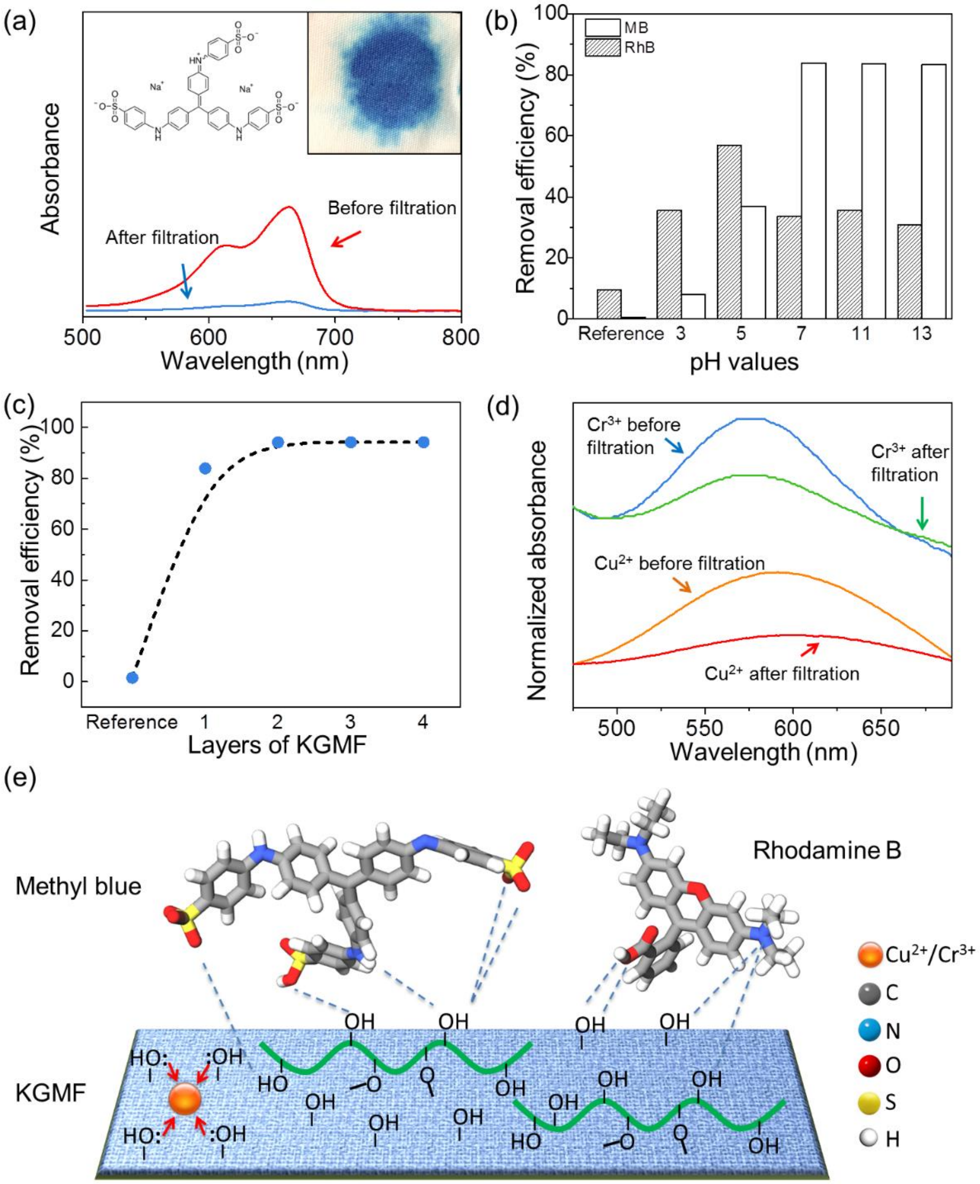

Figure 39. The capability of KGM-modified fabrics to remove water-soluble pollutants..

5.2.5 Conclusions

In summary, by applying biopolymer KGM on fabrics, we demonstrated that the concept of pollutant removal and the principle of oil-water separation could be combined. Owing to the formation of multiple covalent bonds among a crosslinked polysaccharide network, KGMF exhibited excellent oil-water separation efficiency (up to 99.9%), even at conditions of extreme pH values (1 and 13) or high salinity. Furthermore, the purified wastewater, when used to cultivate and irrigate pinto beans, showed no observable influence on bean seedling and growth. Finally, the as-prepared KGMF reveals an intriguing behavior of removing water-soluble pollutants such as polyaromatic MB. The mechanism could be explained by the rich absorptive sites of konjac glucomannan that facilitate the removal of pollutants. These results further confirm the biocompatibility and effectiveness of our KGM-coated hybrid membrane, indicating strong potential for practical applications.

5.3 Self-healing separating membranes

5.3.1 Background

In light of natural nanocomposites such as teeth and bones in which mineral particles assemble with proteins into periodic superstructures,[315] researchers have devoted extensive efforts on designing and developing materials with hierarchical structures at multiple length scale, from the molecular to the macroscopic.[316-317] Such sophisticated architectures of materials enable superior properties for diverse applications such as tissue engineering,[318] high-performance catalysts,[319] and lithium-ion battaries.[320] Furthermore, the hierarchical structure at interfaces plays a crucial role in determining interfacial properties, sparking much of research interest in design of superwetting materials, *i.e.*, superhydrophilic or superhydrophobic.[83, 278] Recently, a biopolymer-functionalized textile was designed and fabricated with unique structure, enabling the modified textile to be underwater superoleophobic with high efficiency of oil-water separation as well as the ability of heavy metal removal.[321] In addition, synthetic strategies, including silicon micropatterning,[322] interfacial assembly,[323-324] and metal-catalyzed coupling reaction,[325] have also been reported for bottom-up fabrication of superwetting structures toward effective oil-water separation. Despite the substantial progress in multifunctional structured materials,[108, 148, 154] however, the development of superstructures that can perform efficiently under extreme conditions and simultaneously heal its damage caused by highly reactive chemical species remains a formidable task. Here, we propose that the self-healing ability can be integrated into hierarchical materials for applications in harsh environments.

Self-healing hybrid composites are materials that can partially or entirely heal inflicted damage. Such materials have drawn tremendous interest for applications including artificial skins,[326] solar cells,[327] and corrosion protections.[328] Experimentally, encapsulation strategy has been extensively studied for fabricating self-healing composites where an encapsulated healing reagent is released upon the external trigger.[329] A dual-capsule approach has also been proposed for the encapsulation of highly reactive core materials.[330] In contrast to significant advances in encapsulation methods, autonomously recurrent healing of composites remains challenging due to rigorous processing and limited recyclability.[331-333] One key factor to achieve consecutive healing lies in the advanced loading of healing agent that is able to replenish its consumption during healing process.[334] Recently, fluoro functional groups have been introduced in polyurethane membrane to achieve self-healing ability because of the minimized surface energy of fluorinated groups.[335] Studies have also shown that a superamphiphobic surface can be readily achieved by directly coating a solution of poly(vinylidene fluoride-cohexafluoropropylene) and organofluorine silane.[336] However, due to the high cost and environmental concerns of organofluorine compounds,[337] strategies based on nonfluorinated nanoparticles for recurrent healing appear to be attractive alternatives.

Motivated by the increasing entropy of excluded volume, the colloidal suspensions of anisotropic particles form microscale mesogen, leading to a fascinating variety of liquid crystalline phases (LC).[205] As a striking example of anisotropic particles, 2D platelets can form multiple lyotropic LCs, resulting in pseudo-3D structures with controllable orderings.[12, 205, 338-339] It was expected that the long-range orientational orderings of lyotropic LC structures may prevent the penetration of highly reactive species, meanwhile allowing a facile loading of sufficient healing agent to form a multi-cycle self-repairing structure. Studies in our research group have shown that such ordering of platelets, *i.e.*, zirconium phosphate (ZrP), can be manipulated by volume fraction, aspect ratio, and Debye length.[207, 339-340] Here, we report the ability of lyotropic ZrP platelets to assemble into a superhydrophobic hierarchical architecture on fabrics that autonomously and recurrently heal damage of chemical oxidation at room temperature.

Our approach was predicated on the structural orientations of ZrP which generate robust layers to protect and separate the healing agent, in prevent of the penetration of oxidative species. 2D platelets were produced by *in situ* growth of lyotropic ZrP on 1D textile fibers governed by structural orientation. Taking advantage of the strong bonding of ZrP with amine species, we introduced the healing agent octadecylamine (ODA) into the layered architecture of ZrP. Therefore, the ZrP functionalized hybrid membrane (ZrPM) revealed a complex, graded structure consisting of hydrophobic ODA, supported in the layered architecture, lyotropic ZrP platelets, aligned parallel to the fiber surface, and textile platform (Figure 40). The robust layers of ZrP platelets prevented the permeation and penetration of oxidative species, protecting healing reagents from chemical oxidation. During repairing, the healing reagent was able to transport to the hybrid membrane surface, restoring the wettability. Meanwhile, the ZrP-coated superhydrophobic fabric demonstrated efficient oil-water separation with good durability, making it applicable to practical applications.

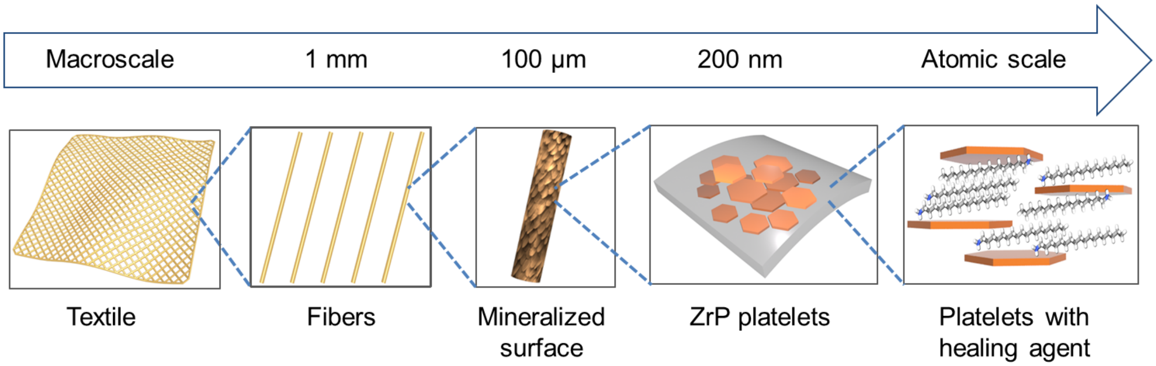

Figure 40. Schematic demonstration of hierarchical structure in ZrPM.

5.3.2 Synthesis and surface chemistry of ZrPM

In light of lamellar structure of tooth enamel, we fabricated the ZrPM by a method involving *in situ* growth of lyotropic ZrP platelets followed by reacting with hydrophobic species ODA (Figure 41**)**. In the first step, the ZrP crystals grew parallel to the microfiber of the fabrics *in situ*, forming a lamellar layer of nanoplatelets. Simulation studies have predicted that a higher anisotropy, *i.e.*, stronger deviation from spherical shape, can facilitate the formation of ordered superstructure from self-assembly of nanoparticles.[205] The nanoplates with thickness/diamerter (T/D) ≤ 0.12 can assemble into orientationally ordered nematic phase at low volume fraction, while an aligned crystal phase is preferred upon high volume fraction ($\varphi \approx 1$).**[338]** Studies in our group have showed that such hydrothermal condition can produce strongly anisotropic ZrP, and this type of 2D nanoplates can bond strongly with amine species.[206-207] In the second step, ZrP bonded with $-NH_2$ of ODA by an acid-base reaction, which enabled a robust hydrophobic surface of the membranes. The preparation method does not involve toxic reagents or expensive catalysts, allowing the potential large-scale manufacturing for practical applications.

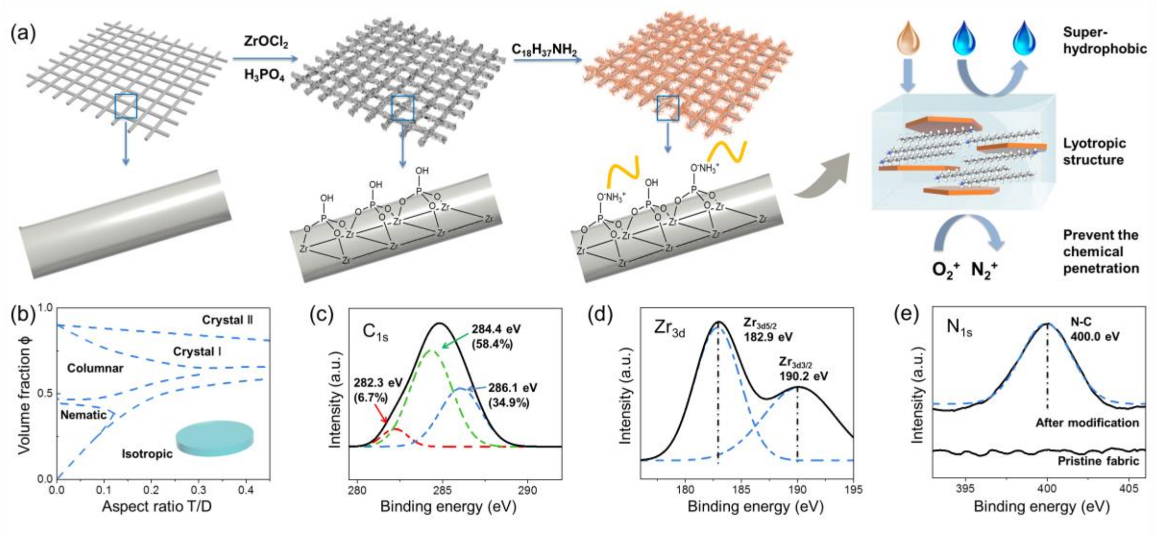

Figure 41. The synthesis and analysis of ZrPM.

The high-resolution C_{1s}, N_{1s}, and Zr_{3d} XPS spectra were collected to understand the chemical environment of hybrid membranes. In Figure 41c, the C_{1s} signals of ZrPM comprise three binding energies at 286.1, 284.4, and 282.3 eV. The first signal can be attributed to C-N bonds by octadecylamine; the second one is due to the carbons (C−C) in textile fibers, whereas the weak signal at 282.3 eV indicates carbide-like carbons in ZrPM.[341] Figure 41 presents the characteristic peaks of ZrPM's binding energy at 190.2, 182.9, and 400.0 eV, corresponding to the $Zr_{3d3/2}$ and $Zr_{3d5/2}$ of the surface ZrP nanoplatelets, and the N_{1s} of C-NH_2 bonds, respectively. It is worth noting here that no significant N signal was observed in pristine textile fibers, indicating that the nitrogen element of ZrPM was likely introduced during the amination of ZrP with ODA. Elemental analysis of the ZrPM showed an atomic ratio of C:O:P:N to be 37:5:1.5:1. The surface coverage of octadecylamine can be estimated by N/P atomic ratio, suggesting approximately 65~67% P-OH being replaced by P-ONH_3^+-$(CH_2)_{17}CH_3$, which is higher than the coverage of ZrP with other amine species, such as tetrabutylammonium hydroxide (around

50%).[153, 342] These results indicated the strong bonding between ZrP and hydrophobic species with good surface coverage.

The morphologies of pristine fabrics and ZrPM were characterized using scanning electron microscopy (SEM). Figure 42a showed the pristine fabric with well-ordered mesh structure (average domain size around 200 μm). After coating with ZrP and octadecylamine, the domain sizes of the fabrics remained almost unchanged. In contrast to the smooth texture of pristine fibers, however, a coarse surface of ZrP-coated fibers was clearly seen. The high magnification of the SEM image revealed a layer of ZrP with polydispersed discotic shape. The cross-sectional image of ZrP-coated fiber showed a pseudo-lamellar structure of ZrP platelets. Figure 42f reflected the morphologies of fabrics after the functionalization with ZrP and octadecylamine. The as-prepared ZrPM revealed a coarser structure, manifesting that the introduced octadecylamine leads to a morphological variation. By comparing diameter differences between pristine fibers and ZrPM fibers, we could roughly estimate the coating thickness, which was calculated to be 0.73 ± 0.23 μm. The increase in surface roughness of ZrPM further demonstrates that ZrP and octadecylamine are successfully coated on the fabrics. Energy-dispersive X-ray spectroscopy (EDS) was used to study the way that ZrP nanoplates assemble on fibers. EDS mapping of a typical ZrP-coated fiber showed the distribution of C, Zr, and P (Figure 42h−j). The areas of marked signals exist almost identical in the Zr and P maps, confirming the consistent distribution of ZrP nanoplatelets on fiber surfaces.

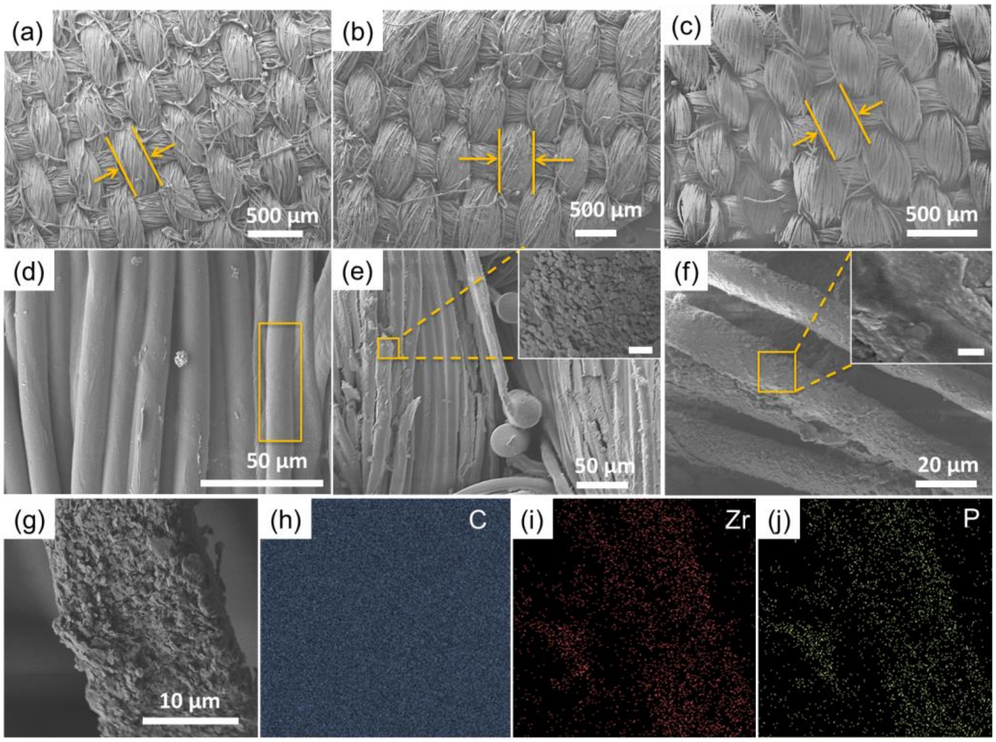

Figure 42. The morphological analysis of membranes.

5.3.3 Oil–water separation and flux performance

We next investigated the wettability of ZrPM by measuring water contact angle (CA). In general, a large water CA would be expected for a highly hydrophobic surface. As shown in Figure 43a, when we applied a H_2O droplet on the ZrPM, there is virtually no change in the size or shape of the water drop, indicating low affinity of ZrPM with H_2O. Upon introducing oil drops (dodecane) on the ZrPM, these oil droplets instantly spread and were absorbed by the membranes, showing the oil contact angles of ZrPM equal to ~0 ° (Figure 43a inset). The ZrPM presented superhydrophobicity with a H_2O CA of $153.9 \pm 1.7°$. CA measurements under a wide range of salinity exclusively revealed high contact angles (> 140 °, Figure 43b), indicating the negligible affinity of ZrPM with aqueous phase. This can be explained by the rich presence of hydrophobic molecule ODA in hierarchical architectures of ZrP so that the H_2O was repelled from the ZrPM surface.

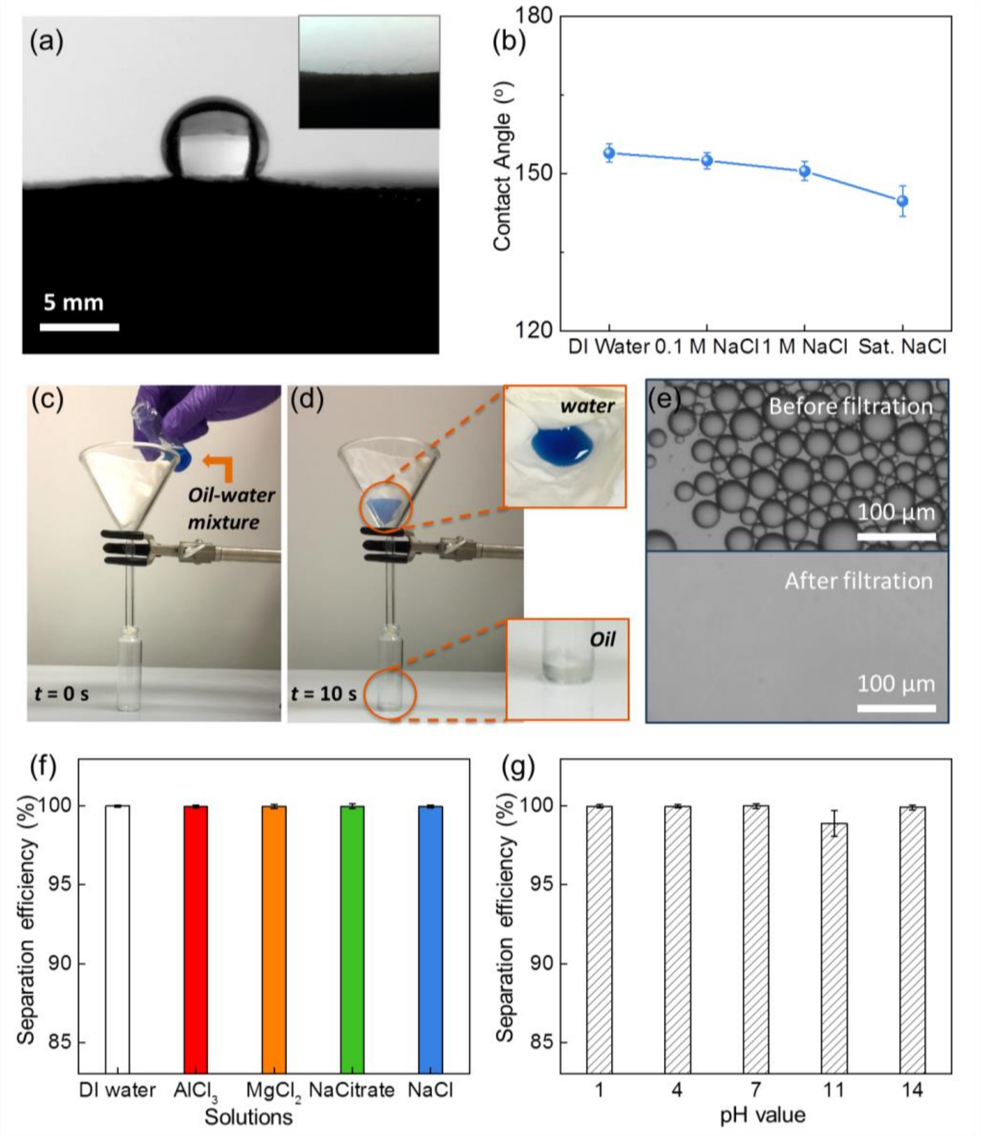

Figure 43. Wettability and separating efficiencies of the ZrPM.

Oil-water separation was performed by introducing the biphasic mixture onto ZrPM. As a classic type of oil, dodecane was mixed with different aqueous phases, while the volumetric percentage of dodecane was fixed at 50 %. To explore the potential of our ZrPM for applications such as purification of oil contaminated seawater, the salt influence on ZrPM was first studied. As ocean water consists of multiple salts,[251] we employed $AlCl_3$, $MgCl_2$, NaCl, and sodium citrate (NaCitrate) solution for studying oil-water separation ability of ZrPM. During the separation process, the dodecane went through ZrPM while aqueous phase was separated (Figure 43c-d). There was no observable oil in collected aqueous phase, which was confirmed by microscopic analysis of aqueous phase (Figure 43e). Figure 43f revealed high separating efficiencies of ZrPM >99.9%, similar to the results published in literatures.[224-225, 227] These results showed that the hybrid membranes wouldn't be dramatically influenced by monovalent cation Na^+, divalent cation Mg^{2+}, trivalent cation Al^{3+}, inorganic anion Cl^-, or organic citrate anion, indicating potential application of ZrPM under typical offshore conditions.

To evaluate the effectiveness of ZrPM under extreme pH values, a range of pH values were tested (Figure 43g). 1 M HCl/NaOH solutions were applied to adjust the solution pH values. The ZrPM demonstrated high oil-water separation efficiency (>99%), showing excellent tolerance of hybrid membranes for extreme pH environments. The excellent stability of ZrPM against pH variations could be a consequence of lamellar self-assembling of ZrP nanoplates following by solid functionalization with octadecylamine, leading to the formation of robust and superhydrophobic coatings against acids/bases from hydrophilic aqueous phase.

To investigate the durability of ZrPM, we performed multiple oil-water separation experiments on one hybrid membrane. Quantitatively, upon increasing the separation experiments up to 25 cycles, the efficiency remained steadily high (>99.9%), as shown in Figure 44a. The CA measurements were also carried out, confirming that the superhydrophobicity was conserved for up to 50 cycles (Figure 44b). The oil-water separation capability of hydrophobic hybrid membrane would not be reduced or damaged by a number of separation cycles, indicating that this type of inorganic-organic hybrid (IOH) membrane shares characteristics with some highly stable polymer-based membranes.[278, 343]

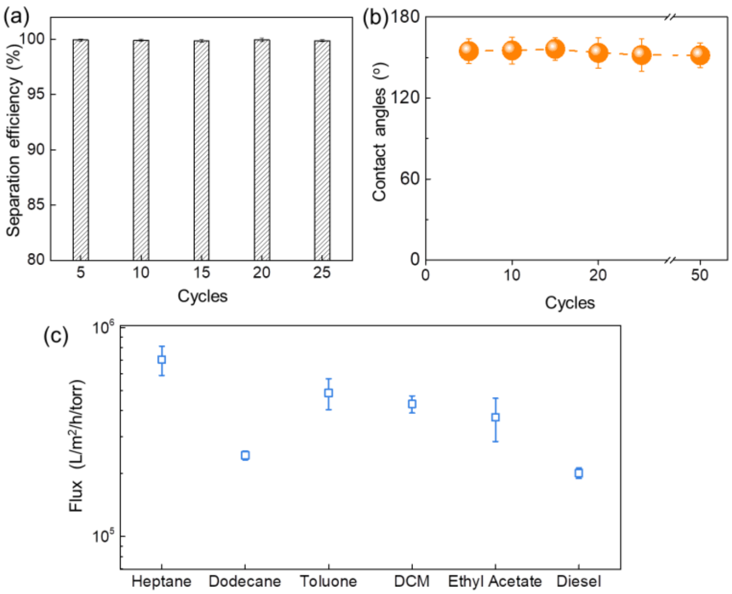

Figure 44. Durability and flux test of the ZrPM.

To evaluate the separation rate of ZrPM, the fluxes of different oils that permeated ZrPM were assessed. In general, all oils permeated the hybrid membranes with high fluxes simply by gravity, though less viscous oils, such as heptane, possessed higher fluxes than more viscous oils such as dodecane. To be specific, as shown in Figure 44c, high fluxes were achieved for heptane, toluene, dichloromethane (DCM), and ethyl acetate, while the flux rate for dodecane and diesel were relatively low. The penetration rates of different oils on hybrid membranes were comparable to that of commercial membranes.[253] The flux variance among several organic oils were attributed to the fluid viscosity differences, as the flux was contrariwise related to viscosity, and possible swelling of ZrPM by different polarity of the organic species which affected membrane pore size.[247, 254] Since the permeation of different oils was driven solely with gravity, we expected a further improved flux performance of hybrid membranes upon introducing external pressure in our future work.

5.3.4 Self-healing performance

The hydrophobic hybrid membranes were treated with air plasma to examine their self-healing capability, as plasma process can damage the hydrophobicity of organic molecules on the outermost surface of the hybrid membranes.[343-344] As shown in Figure 45a-b, the as-prepared superhydrophobic ZrPM became hydrophilic with a CA of around 0 ° after oxidation treatment (air plasma, 350 W for 30 s). This dramatic transformation of wetting behaviors revealed the degradation of the hydrophobic alkyl surface due to the oxidation reaction with gaseous free radicals, leading to the formation of polar functional groups, such as –OH and -COOH.[344] Interestingly, despite the presence of polar hydrophilic groups, it was found that the oil contact angle remained zero (Figure 45h), and when water was dropped on the plasma-treated ZrPM, water drops spread in an anisotropic manner (Figure 45e). These results indicated that the decomposition of the whole hydrophobic layer is neither complete nor homogeneous, signifying the possibilities of future recovery in hydrophobicity.[345-346] After exposing the air-plasma-oxidized ZrPM to air for 48 h at room temperature, the surface hydrophobicity was repaired, as shown in Figure 45c,f. This indicates that the damaged surface was recovered with the hydrophobic alkyl chains.

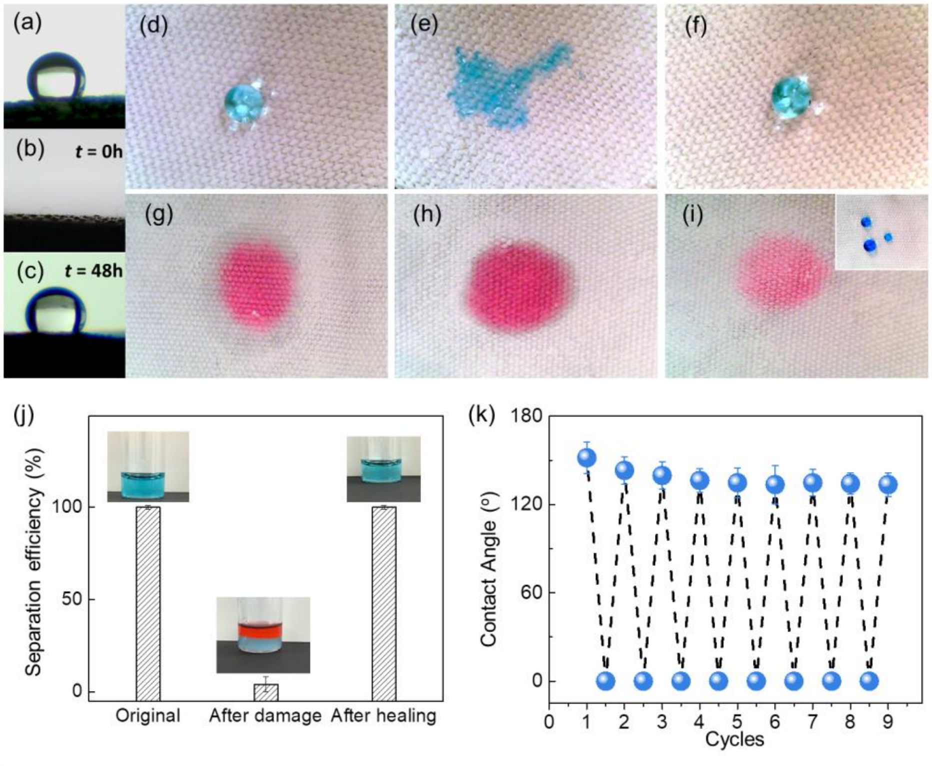

Figure 45. Self-healing ability of the ZrPM.

It is noteworthy that the healing behaviors of hydrophobic ZrPM is heavily dependent on temperature: a higher temperature of 65 °C leads to an accelerated self-healing process in comparison with room temperature conditions (20 °C). As demonstrated in Figure 45i inset, hydrophobicity was reestablished when the oxidized ZrPM was heated at 65 °C for 0.5 h. This can be explained by the thermal migration of the hydrophobic ODA to reduce the surface energy.[347-348]

Separation efficiency tests of the above membranes were also performed, as described in Figure 45j. During separation process, the dodecane permeated easily and the aqueous phase was separated and collected, showing no visible oil in the separated water (Figure 45j inset). When the plasma-treated fabric was used, both oil and water penetrated without any resistance, resulting in poor separation. However, after restoring the hydrophobicity by heating plasma-treated fabric at 65 °C for 0.5 h, clean water was separated successfully with excellent oil-water separation efficiency (>99.9%). These results demonstrate that the ZrPM has a strong ability to heal the damaged hydrophobicity. To quantify the self-healing ability, we performed a number of oxidation-healing cycles with contact angle measurements. As shown in Figure 45k, the contact angle slightly decreased to around 140^{o} in first three cycles, then remained almost unchanged at 135^{o} in following six oxidation-healing cycles. Although the contact angles of healed membranes are not as high as the freshly prepared one, they remain substantially high in comparison with that of reported membranes for oil-water separation applications.[238, 349-350]

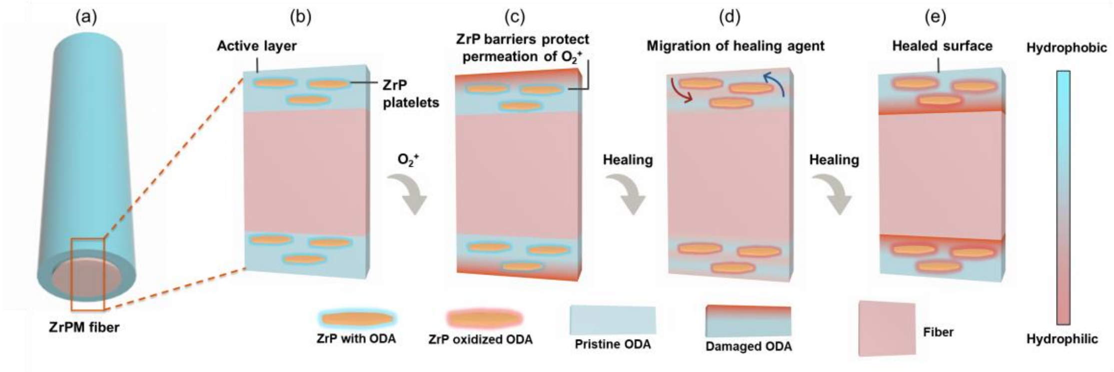

Figure 46. Proposed self-healing mechanism of ZrPM.

To understand the self-healing behavior of ZrPM, we proposed the self-healing mechanism in Figure 46. The self-repairing behaviors of ZrPM arose from protected healing reagent ODA embedded inside the hierarchical architecture of 2D nanoplates that generated robust layers to prevent the penetration of oxidative species. In the deposition step, the healing agent was not only distributed on ZrP platelet surface, also transported into the gap/pores between ZrP nanoplates (Figure 46a). Once the outmost layer of ODA was oxidized by the air plasma, a hydrophilic surface formed (Figure 46b). This hydrophilic surface was thermodynamically unstable due to high surface energy, leading the protected ODA to diffuse to surface to minimize the surface energy of ZrPM.[347-348] Consequently, the polar groups that were generated by air plasma tended to transport inside the coating layer and interacted with hydroxyl groups of ZrP/fabrics (Figure 46c). In the meantime, more hydrophobic alkyl chains were exposed to the surface, leading to a “self-healing” ability (Figure 46d).[343] Furthermore, a higher temperature was able to facilitate the migration process of healing agent, expediting the healing of hydrophobic ZrPM. This is consistent with our observation that the healing time was reduced from 48 h (20 °C) to 0.5 h (65 °C). Such heat-assisted healing effects were also seen in other self-healing systems.[351-352] The overall results indicated that ZrPM not only demonstrated good oil-water separating performance under harsh conditions, but also showed self-healing ability over a number of cycles.

5.3.5 Conclusions

In conclusion, we developed a hierarchical, self-healing and superhydrophobic hybrid membrane via an *in situ* growth of lyotropic ZrP nanoplates on fabrics. We demonstrated that the concept of hierarchical assembly of anisotropic nanoparticles can be generalized to design structural materials with recurrent self-healing behavior. The surface chemistry of ZrPM was confirmed by XPS and the graded structure was confirmed by SEM analysis. In consequence of the lamellar arrangement structure of ZrP, the ZrPM not only separated oil and water in harsh environments, but also showed good durability with high separation efficiencies. Furthermore, we demonstrated that the ZrPM, after damaged by air-plasma, can restore its hydrophobicity automatically and repeatedly. This unique self-healing behaviour suggested strong potential for significantly prolonging the duration of hydrophobic membranes against possible oxidation or strong UV light. The present approach is facile without involving highly toxic reagents or expensive catalysts, indicating strong potential for a wide range of applications such as water treatment, fuel purification, and the cleanup of oil spills.

CHAPTER VI

SUMMARY AND CONCLUSIONS

Through surface engineering and dimension-controlled methods, various 2D materials including 2D graphene quantum dots, ZrP nanosheets, barium ferrite, and kaolinite platelets were synthesized and their collective behaviors at solid-liquid, liquid-liquid, and solid-liquid interfaces were investigated. Understanding the unique role of dimensionality in determining the 2D materials' intrinsic properties is crucial for their potential applications in optical, electronical, and environmental fields, which is the ultimate motivation behind this work.

Chapter II described how surface functional groups could regulate the interfacial behaviours of particle surfactant. As shown in Chapter II, the octadecyl grafted graphene quantum dots (C_{18}-GQDs) surfactants could be used as effective emulsifiers for stabilizing Picking emulsions as well as for mini-emulsion polymerization. Both the photoluminescent and excitation-dependent properties were characterized. Furthermore, by using functionalized graphene quantum dots, uniform Pickering emulsions of dodecane and water were formed with an average size of 263 ± 51 nm; in contrast, no stable Pickering emulsions were produced with solely addition of nonfunctionalized p-GQDs. Phase diagram of C_{18}-GQDs further confirmed the well-balanced amphiphilic property and suggested that water-in-oil emulsions could be created by C_{18}-GQDs. Moreover, C_{18}-GQDs exhibited the high efficiency as surfactants to synthesize uniform C_{18}-GQDs/PS nanocapsules via the mini-emulsion polymerization. In presence of C_{18}-GQDs, polymeric nanocapsules with an average size of 152±8 nm were achieved. This facile one-pot bottom-up synthesis of amphiphilic GQDs combined with their luminescent property provides a possible direction for multifunctional carbon-based quantum dots. In addition, we demonstrated that π–π stacking interactions with graphene are not limited to pyrene derivatives, but are also applicable to larger polyaromatic structures such as graphene quantum dots. We also showed that S-GQDs can stabilize solid/liquid interfaces for the graphene aqueous dispersion.

Chapter III shows the ability of judiciously designed Janus kaolinite nanoplates to dynamically assemble, accumulate, and pack at oil/water interfaces. The nonequilibrium shapes of resulting microemulsions are stable against change of temperature or addition of salt, while droplet morphological transitions can be achieved effectively and repeatedly by adjusting pH values. An electrostatic model has been proposed to understand the dynamic jamming of SJPs and reversible shape transition of droplets, which was further verified by Monte Carlo calculation. The electrostatic-driven reversible interfacial jamming of NP-surfactants disclosed herein is expected to open a brand-new door for their promising applications in areas of controlled drug delivery, functional intelligent nanoplatforms, and many other biomedical-related fields. In addition, a two-dimensional catalytic nanomotor based on magnetic BF nanoparticles was prepared. We demonstrated that self-propulsion behaviors are not limited to 0D nanospheres and 1D nanorods, but are also applicable to 2D nanoplatelets. The enhanced diffusion of BF-based nanomotors with different Pt thicknesses were also evaluated, and the large amount of Pt showed more efficient in converting chemical into speed. The surface chemistry of PtBF was investigated by XPS and the 2D structure was confirmed by TEM and AFM analysis. In consequence of the 2D nanoscale structure of PtBF, the nanomotor not only catalyzes the decomposition of free organic dye in solution over a wide range of pollutant concentrations, but also shows excellent catalytic performance in removing adsorbed pollutants with good recyclability due to the magnetic nature of BF. The present approach is straightforward and possibly applicable to other 2D materials, indicating strong potential for a wide range of applications such as water treatment, nanoscale cleanup, and catalytic chemical reaction.

Chapter IV describes the ability to engineer the molecular interaction of 2D colloids by manipulating the first order transition of isotropic to lamellar phase such that an on-demand control of photonic bandgap of polydispersed nanosheet suspensions can be readily achieved. The novelty of our results lies in several reasons. First, the method for assembly of 2D colloids using phase transitions was established as a promising model strategy to manipulate the structural properties of soft materials. This is complementary to existing methods of assembling anisotropic colloidal systems. Second, we have demonstrated that particle dimensional factors and electrostatic interaction play essential roles in phase evolutions of colloidal nanosheet, as has been proposed by theories[207]. Tuning aspect ratio and electrostatic interaction of 2D colloids enables the manipulation of phase diagrams with positional order. Finally, we were able to tailor the phase behaviours of colloidal nanosheets and achieved a wide range of photonic colours, which in turn help to understand the phase diagram of ZrP nanosheets. For the first time, the synergetic effects of phase transition and size manipulation was employed to precisely control the highly ordered self-assembly of 2D nanosheets in dispersions, and we expect that our research heralds the fabrication of the hierarchical structure of 2D materials in soft polymer matrix that might exhibit intriguing optical and mechanical properties.

Chapter III shows the ability of engineering the surface of 2D membranes allows various functional properties including fast separation, heavy metal removal, and self-healing feature. First, high-flux polymer-modified filter papers not only demonstrate strong potential in oil-water separation for a wide range of conditions, such as high salt concentrations, extreme pH, different temperatures, and oil-water emulsions stabilized by a variety of surfactants, but also show high flux in acidic, alkaline, saline environments. Second, by applying biopolymer KGM on fabrics, we demonstrated that the concept of pollutant removal and the principle of oil-water separation could be combined. Owing to the formation of multiple covalent bonds among a crosslinked polysaccharide network, KGMF exhibited excellent oil-water separation efficiency (up to 99.9%), even at conditions of extreme pH values (1 and 13) or high salinity. Furthermore, the purified wastewater, when used to cultivate and irrigate pinto beans, showed no observable influence on bean seedling and growth. Finally, the as-prepared KGMF reveals an intriguing behavior of removing water-soluble pollutants such as polyaromatic MB. The mechanism could be explained by the rich absorptive sites of konjac glucomannan that facilitate the removal of pollutants. Last but not the least, we developed a hierarchical, self-healing and superhydrophobic hybrid membrane via an *in situ* growth of lyotropic ZrP nanoplates on fabrics. We demonstrated that the concept of hierarchical assembly of anisotropic nanoparticles can be generalized to design structural materials with recurrent self-healing behavior. The surface chemistry of ZrPM was confirmed by XPS and the graded structure was confirmed by SEM analysis. In consequence of the lamellar arrangement structure of ZrP, the ZrPM not only separated oil and water in harsh environments, but also showed good durability with high separation efficiencies. Furthermore, we demonstrated that the ZrPM, after damaged by air-plasma, can restore its hydrophobicity automatically and repeatedly. This unique self-healing behaviour suggested strong potential for significantly prolonging the duration of hydrophobic membranes against possible oxidation or strong UV light. The present approach is facile without involving highly toxic reagents or expensive catalysts, indicating strong potential for a wide range of applications such as water treatment, fuel purification, and the cleanup of oil spills.

REFERENCES

1. Nasilowski, M.; Mahler, B.; Lhuillier, E.; Ithurria, S.; Dubertret, B., Two-dimensional colloidal nanocrystals. *Chemical Reviews* **2016,** *116* (18), 10934-10982.

2. Nicolosi, V.; Chhowalla, M.; Kanatzidis, M. G.; Strano, M. S.; Coleman, J. N., Liquid Exfoliation of Layered Materials. *Science* **2013,** *340* (6139), 1226419.

3. Novoselov, K. S.; Mishchenko, A.; Carvalho, A.; Neto, A. H. C., 2D Materials and van der Waals Heterostructures. *Science* **2016,** *353*, aac9439.

4. Dervin, S.; Dionysiou, D. D.; Pillai, S. C., 2D nanostructures for water purification: graphene and beyond. *Nanoscale* **2016,** *8* (33), 15115-15131.

5. Xia, Y.; Mathis, T. S.; Zhao, M.-Q.; Anasori, B.; Dang, A.; Zhou, Z.; Cho, H.; Gogotsi, Y.; Yang, S., Thickness-independent capacitance of vertically aligned liquid-crystalline MXenes. *Nature* **2018,** *557* (7705), 409-412.

6. Mi, B., Graphene Oxide Membranes for Ionic and Molecular Sieving. *Science* **2014,** *343* (6172), 740-742.

7. Nair, R. R.; Wu, H. A.; Jayaram, P. N.; Grigorieva, I. V.; Geim, A. K., Unimpeded Permeation of Water Through Helium-Leak–Tight Graphene-Based Membranes. *Science* **2012,** *335* (6067), 442-444.

8. Jin, H.; Guo, C.; Liu, X.; Liu, J.; Vasileff, A.; Jiao, Y.; Zheng, Y.; Qiao, S.-Z., Emerging Two-Dimensional Nanomaterials for Electrocatalysis. *Chemical Reviews* **2018,** *118* (13), 6337-6408.

9. Wang, X.; Xia, F., Van der Waals heterostructures: Stacked 2D materials shed light. *Nature Materials* **2015,** *14* (3), 264-265.

10. Balendhran, S.; Walia, S.; Nili, H.; Sriram, S.; Bhaskaran, M., Elemental Analogues of Graphene: Silicene, Germanene, Stanene, and Phosphorene. *Small* **2015,** *11* (6), 640-652.

11. Cai, Z.; Liu, B.; Zou, X.; Cheng, H.-M., Chemical Vapor Deposition Growth and Applications of Two-Dimensional Materials and Their Heterostructures. *Chemical Reviews* **2018**. *118* (13), 6091–6133

12. Wong, M.; Ishige, R.; White, K. L.; Li, P.; Kim, D.; Krishnamoorti, R.; Gunther, R.; Higuchi, T.; Jinnai, H.; Takahara, A.; Nishimura, R.; Sue, H.-J., Large-scale self-assembled zirconium phosphate smectic layers via a simple spray-coating process. *Nature Communications* **2014,** *5*, 3589.

13. Xu, Z.; Gao, C., Graphene chiral liquid crystals and macroscopic assembled fibres. *Nature Communications* **2011,** *2*, 571.

14. Sano, K.; Kim, Y. S.; Ishida, Y.; Ebina, Y.; Sasaki, T.; Hikima, T.; Aida, T., Photonic water dynamically responsive to external stimuli. *Nature Communications* **2016,** *7*, 12559

15. Chimene, D.; Alge, D. L.; Gaharwar, A. K., Two-dimensional nanomaterials for biomedical applications: emerging trends and future prospects. *Advanced Materials* **2015,** *27* (45), 7261-7284.

16. Novoselov, K. S.; Geim, A. K.; Morozov, S. V.; Jiang, D.; Zhang, Y.; Dubonos, S. V.; Grigorieva, I. V.; Firsov, A. A., Electric Field Effect in Atomically Thin Carbon Films. *Science* **2004,** *306*, 666.

17. Novoselov, K. S.; Geim, A. K.; Morozov, S. V.; Jiang, D.; Katsnelson, M. I.; Grigorieva, I. V.; Dubonos, S. V.; Firsov, A. A., Two-Dimensional Gas of Massless Dirac Fermions in Graphene. *Nature* **2005,** *438*, 197.

18. Novoselov, K. S.; Jiang, D.; Schedin, F.; Booth, T. J.; Khotkevich, V. V.; Morozov, S. V.; Geim, A. K., Two-Dimensional Atomic Crystals. *Proceedings of the National Academy of Sciences U. S. A.* **2005,** *102*, 10451.

19. Geim, A. K.; Novoselov, K. S., The Rising of Graphene. *Nature Materials* **2007,** *6*, 183.

20. Huang, Y.; Sutter, E.; Shi, N. N.; Zheng, J.; Yang, T.; Englund, D.; Gao, H. J.; Sutter, P., Reliable Exfoliation of Large-Area High-Quality Flakes of Graphene and Other Two-Dimensional Materials. *ACS Nano* **2015,** *9*, 10612.

21. Hernandez, Y.; Nicolosi, V.; Lotya, M.; Blighe, F. M.; Sun, Z.; De, S.; McGovern, I. T.; Holland, B.; Byrne, M.; Gun'Ko, Y. K., High-Yield Production of Graphene by Liquid-phase Exfoliation of Graphite. *Nature Nanotechnology* **2008,** *3*, 563.

22. Xu, L. X.; McGraw, J. W.; Gao, F.; Grundy, M.; Ye, Z. B.; Gu, Z. Y.; Shepherd, J. L., Production of High-Concentration Graphene Dispersions in Low-Boiling-Point Organic Solvents by Liquid-Phase Noncovalent Exfoliation of Graphite with a Hyperbranched Polyethylene and Formation of Graphene/Ethylene Copolymer Composites. *Journal of Physical Chemistry C* **2013,** *117*, 10730.

23. O'neill, A.; Khan, U.; Nirmalraj, P. N.; Boland, J.; Coleman, J. N., Graphene Dispersion and Exfoliation in Low Boiling Point Solvents. *Journal of Physical Chemistry C* **2011,** *115*, 5422.

24. Coleman, J. N.; Lotya, M.; O'Neill, A.; Bergin, S. D.; King, P. J.; Khan, U.; Young, K.; Gaucher, A.; De, S.; Smith, R. J., Two-Dimensional Nanosheets Produced by Liquid Exfoliation of Layered Materials. *Science* **2011,** *331*, 568.

25. Dong, X.; Shi, Y.; Zhao, Y.; Chen, D.; Ye, J.; Yao, Y.; Gao, F.; Ni, Z.; Yu, T.; Shen, Z.; Huang, Y.; Chen, P.; Li, L.-J., Symmetry Breaking of Graphene Monolayers by Molecular Decoration. *Physical Review Letters* **2009,** *102* (13), 135501.

26. Zhang, M.; Parajuli, R. R.; Mastrogiovanni, D.; Dai, B.; Lo, P.; Cheung, W.; Brukh, R.; Chiu, P. L.; Zhou, T.; Liu, Z., Production of graphene sheets by direct dispersion with aromatic healing agents. *Small* **2010,** *6* (10), 1100-1107.

27. Parviz, D.; Das, S.; Ahmed, H. S. T.; Irin, F.; Bhattacharia, S.; Green, M. J., Dispersions of Non-Covalently Functionalized Graphene with Minimal Stabilizer. *ACS Nano* **2012,** *6* (10), 8857-8867.

28. Ciesielski, A.; Samor ì P., Graphene via sonication assisted liquid-phase exfoliation. *Chemical Society Reviews* **2014,** *43* (1), 381-398.

29. Eigler, S.; Hirsch, A., Chemistry with graphene and graphene oxide—challenges for synthetic chemists. *Angewandte Chemie International Edition* **2014,** *53* (30), 7720-7738.

30. Liang, Y. T.; Hersam, M. C., Highly Concentrated Graphene Solutions via Polymer Enhanced Solvent Exfoliation and Iterative Solvent Exchange. *Journal of the American Chemical Society* **2010,** *132*, 17661.

31. Smith, R. J.; King, P. J.; Lotya, M.; Wirtz, C.; Khan, U.; De, S.; O'Neill, A.; Duesberg, G. S.; Grunlan, J. C.; Moriarty, G., Large-Scale Exfoliation of Inorganic Layered Compounds in Aqueous Surfactant Solutions. *Advanced Materials* **2011,** *23*, 3944.

32. Guan, G.; Zhang, S.; Liu, S.; Cai, Y.; Low, M.; Teng, C. P.; Phang, I. Y.; Cheng, Y.; Duei, K. L.; Srinivasan, B. M., Protein Induces Layer-by-Layer Exfoliation of Transition Metal Dichalcogenides. *Journal of the American Chemical Society* **2015,** *137*, 6152.

33. May, P.; Khan, U.; Hughes, J. M.; Coleman, J. N., Role of Solubility Parameters in Understanding the Steric Stabilization of Exfoliated Two-Dimensional Nanosheets by Adsorbed Polymers. *Journal of Physical Chemistry C* **2012,** *116*, 11393.

34. Paton, K. R.; Varrla, E.; Backes, C.; Smith, R. J.; Khan, U.; O'Neill, A.; Boland, C.; Lotya, M.; Istrate, O. M.; King, P., Scalable Production of Large Quantities of Defect-Free Few-Layer Graphene by Shear Exfoliation in Liquids. *Nature Materials* **2014,** *13*, 624.

35. Osada, M.; Sasaki, T., Nanosheet Architectonics: A Hierarchically Structured Assembly for Tailored Fusion Materials. *Polymer Journal* **2015,** *47*, 89.

36. Wang, Q.; O'Hare, D., Recent Advances in the Synthesis and Application oLayered Double Hydroxide (LDH) Nanosheets. *Chemical Reviews* **2012,** *112*, 4124.

37. Adachi-Pagano, M.; Forano, C.; Besse, J. P., Delamination of Layered Double Hydroxides by Use of Surfactants. *Chemical Communications* **2000,** *1*, 91.

38. Fan, X.; Peng, W.; Li, Y.; Li, X.; Wang, S.; Zhang, G.; Zhang, F., Deoxygenation of Exfoliated Graphite Oxide under Alkaline Conditions: A Green Route to Graphene Preparation. *Advanced Materials* **2008,** *20*, 4490.

39. Erickson, K.; Erni, R.; Lee, Z.; Alem, N.; Gannett, W.; Zettl, A., Determination of the Local Chemical Structure of Graphene Oxide and Reduced Graphene Oxide. *Advanced Materials* **2010,** *22*, 4467.

40. Naguib, M.; Mochalin, V. N.; Barsoum, M. W.; Gogotsi, Y., 25th Anniversary Article: MXenes: A New Family of Two-Dimensional Materials. *Advanced Materials* **2014,** *26*, 992.

41. Wang, X.; Kajiyama, S.; Iinuma, H.; Hosono, E.; Oro, S.; Moriguchi, I.; Okubo, M.; Yamada, A., Pseudocapacitance of MXene Nanosheets for High-Power Sodium-Ion Hybrid Capacitors. *Nature Communications* **2015,** *6*, 6544.

42. Halim, J.; Kota, S.; Lukatskaya, M. R.; Naguib, M.; Zhao, M. Q.; Moon, E. J.; Pitock, J.; Nanda, J.; May, S. J.; Gogotsi, Y.; Barsou, M. W., Synthesis and Characterization of 2D Molybdenum Carbide (MXene). *Advanced Functional Materials* **2016,** *26*, 3118.

43. Urbankowski, P.; Anasori, B.; Makaryan, T.; Er, D.; Kota, S.; Walsh, P. L.; Zhao, M.; Shenoy, V. B.; Barsouma, M. W.; Gogotsi, Y., Synthesis of Two-Dimensional Titanium Nitride Ti4N3 (MXene). *Nanoscale* **2016,** *8*, 11385.

44. Anasori, B.; Xie, Y.; Beidaghi, M.; Lu, J.; Hosler, B.; Hultman, L.; Kent, P.; Gogotsi, Y.; Barsoum, M. W., Two-Dimensional, Ordered, Double Transition Metals Carbides (MXenes). *ACS Nano* **2015,** *9*, 9507.

45. Manzeli, S.; Ovchinnikov, D.; Pasquier, D.; Yazyev, O. V.; Kis, A., 2D transition metal dichalcogenides. *Nature Reviews Materials* **2017,** *2* (8), 17033.

46. Gao, S.; Lin, Y.; Jiao, X.; Sun, Y.; Luo, Q.; Zhang, W.; Li, D.; Yang, J.; Xie, Y., Partially oxidized atomic cobalt layers for carbon dioxide electroreduction to liquid fuel. *Nature* **2016,** *529* (7584), 68.

47. Yu, T.; Lim, B.; Xia, Y. N., Aqueous-Phase Synthesis of Single-Crystal Ceria Nanosheets. *Angewandte Chemie International Edition* **2010,** *49*, 4484.

48. Simon, P.; Bahrig, L.; Baburin, I. A.; Formanek, P.; Roder, F.; Sickmann, J.; Hickey, S. G.; Eychmuller, A.; Lichte, H.; Kniep, R.; Rosseeva, E., Interconnection of Nanoparticles within 2D Superlattices of PbS/Oleic Acid Thin Films. *Advanced Materials* **2014,** *26*, 3042.

49. Niu, J.; Wang, D.; Qin, H.; Xiong, X.; Tan, P.; Li, Y.; Liu, R.; Lu, X.; Wu, J.; Zhang, T., Novel polymer-free iridescent lamellar hydrogel for two-dimensional confined growth of ultrathin gold membranes. *Nature Communications* **2014,** *5*, 3313.

50. Son, J. S.; Wen, X. D.; Joo, J.; Chae, J.; Baek, S. I.; Park, K.; Kim, J. H.; An, K.; Yu, J. H.; Kwon, S. G., Large-Scale Soft Colloidal Template Synthesis of 1.4 nm Thick CdSe Nanosheets. *Angewandte Chemie International Edition* **2009,** *48*, 6861.

51. Xu, L.; Zhou, X.; Tian, W. Q.; Gao, T.; Zhang, Y. F.; Lei, S.; Liu, Z., Surface-Confined Single-Layer Covalent Organic Framework on Single-Layer Graphene Grown on Copper Foil. *Angewandte Chemie International Edition* **2014,** *53*, 9564.

52. Boott, C. E.; Nazemi, A.; Manners, I., Synthetic Covalent and Non-Covalent 2D Materials. *Angewandte Chemie International Edition* **2015,** *54*, 13876.

53. Rodriguez-San-Miguel, D.; Amo-Ochoa, P.; Zamora, F., MasterChem: Cooking 2D-Polymers. *Chemical Communications.* **2016,** *52*, 4113.

54. Wang, J.; Chen, Z.; Chen, B., Adsorption of Polycyclic Aromatic Hydrocarbons by Graphene and Graphene Oxide Nanosheets. *Environmental Science & Technology* **2014,** *48* (9), 4817-4825.

55. Zhao, G.; Jiang, L.; He, Y.; Li, J.; Dong, H.; Wang, X.; Hu, W., Sulfonated graphene for persistent aromatic pollutant management. *Advanced Materials* **2011,** *23* (34), 3959-3963.

56. Thickett, S. C.; Zetterlund, P. B., Preparation of Composite Materials by Using Graphene Oxide as a Surfactant in Ab Initio Emulsion Polymerization Systems. *ACS Macro Letters* **2013,** *2* (7), 630-634.

57. Yang, H.; Kang, D. J.; Ku, K. H.; Cho, H. H.; Park, C. H.; Lee, J.; Lee, D. C.; Ajayan, P. M.; Kim, B. J., Highly Luminescent Polymer Particles Driven by Thermally Reduced Graphene Quantum Dot Surfactants. *ACS Macro Letters* **2014,** *3* (10), 985-990.

58. Zheng, X. T.; Ananthanarayanan, A.; Luo, K. Q.; Chen, P., Glowing graphene quantum dots and carbon dots: properties, syntheses, and biological applications. *Small* **2014**.

59. Gokhale, R.; Singh, P., Blue Luminescent Graphene Quantum Dots by Photochemical Stitching of Small Aromatic Molecules: Fluorescent Nanoprobes in Cellular Imaging. *Particle & Particle Systems Characterization* **2014,** *31* (4), 433-438.

60. Zhu, Z. L.; Ma, J. A.; Wang, Z. L.; Mu, C.; Fan, Z. T.; Du, L. L.; Bai, Y.; Fan, L. Z.; Yan, H.; Phillips, D. L.; Yang, S. H., Efficiency Enhancement of Perovskite Solar Cells through Fast Electron Extraction: The Role of Graphene Quantum Dots. *Journal of the American Chemical Society* **2014,** *136* (10), 3760-3763.

61. Zhu, S. J.; Zhang, J. H.; Tang, S. J.; Qiao, C. Y.; Wang, L.; Wang, H. Y.; Liu, X.; Li, B.; Li, Y. F.; Yu, W. L.; Wang, X. F.; Sun, H. C.; Yang, B., Surface Chemistry Routes to Modulate the Photoluminescence of Graphene Quantum Dots: From Fluorescence Mechanism to Up-Conversion Bioimaging Applications. *Advanced Functional Materials* **2012,** *22* (22), 4732-4740.

62. Yang, K. D.; Ha, Y.; Sim, U.; An, J.; Lee, C. W.; Jin, K.; Kim, Y.; Park, J.; Hong, J. S.; Lee, J. H.; Lee, H.-E.; Jeong, H.-Y.; Kim, H.; Nam, K. T., Graphene Quantum Sheet Catalyzed Silicon Photocathode for Selective CO2 Conversion to CO. *Advanced Functional Materials* **2015**, 233-242.

63. Liu, B.; Xie, J.; Ma, H.; Zhang, X.; Pan, Y.; Lv, J.; Ge, H.; Ren, N.; Su, H.; Xie, X., From Graphite to Graphene Oxide and Graphene Oxide Quantum Dots. *Small* **2017**, 1601001.

64. Liu, Q.; Guo, B. D.; Rao, Z. Y.; Zhang, B. H.; Gong, J. R., Strong Two-Photon-Induced Fluorescence from Photostable, Biocompatible Nitrogen-Doped Graphene Quantum Dots for Cellular and Deep-Tissue Imaging. *Nano letters* **2013,** *13* (6), 2436-2441.

65. Kim, J. K.; Park, M. J.; Kim, S. J.; Wang, D. H.; Cho, S. P.; Bae, S.; Park, J. H.; Hong, B. H., Balancing Light Absorptivity and Carrier Conductivity of Graphene Quantum Dots for High-Efficiency Bulk Heterojunction Solar Cells. *ACS Nano* **2013,** *7* (8), 7207-7212.

66. Cho, H. H.; Yang, H.; Kang, D. J.; Kim, B. J., Surface Engineering of Graphene Quantum Dots and Their Applications as Efficient Surfactants. *ACS Applied Materials & Interfaces* **2015,** *7* (16), 8615-8621.

67. Zeng, M.; Wang, X.; Yu, Y.-H.; Zhang, L.; Shafi, W.; Huang, X.; Cheng, Z., The Synthesis of Amphiphilic Luminescent Graphene Quantum Dot and Its Application in Mini-Emulsion Polymerization. *Journal of Nanomaterials*, **2016**, 1(1), 2016

68. Dong, Y.; Chen, C.; Zheng, X.; Gao, L.; Cui, Z.; Yang, H.; Guo, C.; Chi, Y.; Li, C. M., One-step and high yield simultaneous preparation of single-and multi-layer graphene quantum dots from CX-72 carbon black. *Journal of Material Chemistry* **2012,** *22* (18), 8764-8766.

69. Zhu, S.; Zhang, J.; Qiao, C.; Tang, S.; Li, Y.; Yuan, W.; Li, B.; Tian, L.; Liu, F.; Hu, R., Strongly green-photoluminescent graphene quantum dots for bioimaging applications. *Chemical Communications* **2011,** *47* (24), 6858-6860.

70. Li, H. T.; He, X. D.; Kang, Z. H.; Huang, H.; Liu, Y.; Liu, J. L.; Lian, S. Y.; Tsang, C. H. A.; Yang, X. B.; Lee, S. T., Water-Soluble Fluorescent Carbon Quantum Dots and Photocatalyst Design. *Angewandte Chemie International Edition* **2010,** *49* (26), 4430-4434.

71. Dong, Y. Q.; Shao, J. W.; Chen, C. Q.; Li, H.; Wang, R. X.; Chi, Y. W.; Lin, X. M.; Chen, G. N., Blue luminescent graphene quantum dots and graphene oxide prepared by tuning the carbonization degree of citric acid. *Carbon* **2012,** *50* (12), 4738-4743.

72. Zhu, S.; Meng, Q.; Wang, L.; Zhang, J.; Song, Y.; Jin, H.; Zhang, K.; Sun, H.; Wang, H.; Yang, B., Highly photoluminescent carbon dots for multicolor patterning, sensors, and bioimaging. *Angewandte Chemie* **2013,** *125* (14), 4045-4049.

73. Lu, J.; Yeo, P. S. E.; Gan, C. K.; Wu, P.; Loh, K. P., Transforming C60 molecules into graphene quantum dots. *Nature Nanotechnology* **2011,** *6* (4), 247-252.

74. Yan, X.; Cui, X.; Li, L.-s., Synthesis of large, stable colloidal graphene quantum dots with tunable size. *Journal of the American Chemical Society* **2010,** *132* (17), 5944-5945.

75. Sun, C.; Figge, F.; Ozfidan, I.; Korkusinski, M.; Yan, X.; Li, L.-s.; Hawrylak, P.; McGuire, J. A., Biexciton binding of Dirac fermions confined in colloidal graphene quantum dots. *Nano Letters* **2015,** *15* (8), 5472-5476.

76. Lisjak, D.; Drofenik, M., Chemical Substitution—An Alternative Strategy for Controlling the Particle Size of Barium Ferrite. *Crystal Growth & Design* **2012,** *12* (11), 5174-5179.

77. Kim, D.-H.; Rozhkova, E. A.; Ulasov, I. V.; Bader, S. D.; Rajh, T.; Lesniak, M. S.; Novosad, V., Biofunctionalized magnetic-vortex microdiscs for targeted cancer-cell destruction. *Nature Materials* **2010,** *9* (2), 165.

78. Connell, D.; Miller, G.; Farrington, J., Petroleum hydrocarbons in aquatic ecosystems—behavior and effects of sublethal concentrations: Part 2. *Critical Reviews in Environmental Science and Technology* **1981,** *11* (2), 105-162.

79. Cheryan, M.; Rajagopalan, N., Membrane processing of oily streams. Wastewater treatment and waste reduction. *Journal of Membrane Science* **1998,** *151* (1), 13-28.

80. Krebs, T.; Schroën, C.; Boom, R., Separation kinetics of an oil-in-water emulsion under enhanced gravity. *Chemical Engineering Science* **2012,** *71*, 118-125.

81. Zeng, Y.; Yang, C.; Zhang, J.; Pu, W., Feasibility investigation of oily wastewater treatment by combination of zinc and PAM in coagulation/flocculation. *Journal of Hazardous Materials* **2007,** *147* (3), 991-996.

82. Xuan, Y.; Peng, J.; Cui, L.; Wang, H.; Li, B.; Han, Y., Morphology development of ultrathin symmetric diblock copolymer film via solvent vapor treatment. *Macromolecules* **2004,** *37* (19), 7301-7307.

83. Fan, J. B.; Song, Y.; Wang, S.; Meng, J.; Yang, G.; Guo, X.; Feng, L.; Jiang, L., Directly Coating Hydrogel on Filter Paper for Effective Oil–Water Separation in Highly Acidic, Alkaline, and Salty Environment. *Advanced Functional Materials* **2015,** *25* (33), 5368-5375.

84. Paul, U. C.; Fragouli, D.; Bayer, I. S.; Athanassiou, A., Functionalized Cellulose Networks for Efficient Oil Removal from Oil–Water Emulsions. *Polymers* **2016,** *8* (2), 52.

85. Pickering, S. U., Emulsions. *Journal of Chemical Society* **1907,** *91*, 2001-2021.

86. Stocco, A.; Rio, E.; Binks, B. P.; Langevin, D., Aqueous foams stabilized solely by particles. *Soft Matter* **2011,** *7* (4), 1260-1267.

87. Gonzenbach, U. T.; Studart, A. R.; Tervoort, E.; Gauckler, L. J., Ultrastable particle-stabilized foams. *Angewandte Chemie International Edition* **2006,** *45* (21), 3526-3530.

88. Rayner, M.; Marku, D.; Eriksson, M.; Sjöö, M.; Dejmek, P.; Wahlgren, M., Biomass-based particles for the formulation of Pickering type emulsions in food and topical

applications. *Colloids and Surfaces A: Physicochemical and Engineering Aspects* **2014,** *458*, 48-62.

89. Aveyard, R.; Binks, B. P.; Clint, J. H., Emulsions stabilised solely by colloidal particles. *Advances in Colloid and Interface Science* **2003,** *100*, 503-546.

90. Arditty, S.; Schmitt, V.; Giermanska-Kahn, J.; Leal-Calderon, F., Materials based on solid-stabilized emulsions. *Journal of Colloid and Interface Science* **2004,** *275* (2), 659-664.

91. Herzig, E. M.; White, K. A.; Schofield, A. B.; Poon, W. C. K.; Clegg, P. S., Bicontinuous emulsions stabilized solely by colloidal particles. *Nature Materials* **2007,** *6* (12), 966-971.

92. Binks, B. P.; Boa, A. N.; Kibble, M. A.; Mackenzie, G.; Rocher, A., Sporopollenin capsules at fluid interfaces: particle-stabilised emulsions and liquid marbles. *Soft Matter* **2011,** *7* (8), 4017-4024.

93. Kim, S. H.; Lee, S. Y.; Yang, S. M., Janus Microspheres for a Highly Flexible and Impregnable Water-Repelling Interface. *Angewandte Chemie International Edition* **2010,** *49* (14), 2535-2538.

94. Aussillous, P.; Quere, D., Liquid marbles. *Nature* **2001,** *411* (6840), 924-927.

95. Jiang, J. H.; Zhu, Y.; Cui, Z. G.; Binks, B. P., Switchable Pickering Emulsions Stabilized by Silica Nanoparticles Hydrophobized In Situ with a Switchable Surfactant. *Angewandte Chemie International Edition* **2013,** *52* (47), 12373-12376.

96. Chen, Z. W.; Zhou, L.; Bing, W.; Zhang, Z. J.; Li, Z. H.; Ren, J. S.; Qu, X. G., Light Controlled Reversible Inversion of Nanophosphor-Stabilized Pickering Emulsions for Biphasic Enantioselective Biocatalysis. *Journal of the American Chemical Society* **2014,** *136* (20), 7498-7504.

97. Sacanna, S.; Kegel, W. K.; Philipse, A. P., Thermodynamically stable pickering emulsions. *Physical Review Letters* **2007,** *98* (15), 158301.

98. de Folter, J. W. J.; van Ruijven, M. W. M.; Velikov, K. P., Oil-in-water Pickering emulsions stabilized by colloidal particles from the water-insoluble protein zein. *Soft Matter* **2012,** *8* (25), 6807-6815.

99. Destribats, M.; Rouvet, M.; Gehin-Delval, C.; Schmitt, C.; Binks, B. P., Emulsions stabilised by whey protein microgel particles: towards food-grade Pickering emulsions. *Soft Matter* **2014,** *10* (36), 6941-6954.

100. Mejia, A. F.; Diaz, A.; Pullela, S.; Chang, Y. W.; Simonetty, M.; Carpenter, C.; Batteas, J. D.; Mannan, M. S.; Clearfield, A.; Cheng, Z. D., Pickering emulsions stabilized by amphiphilic nano-sheets. *Soft Matter* **2012,** *8* (40), 10245-10253.

101. Reger, M.; Sekine, T.; Okamoto, T.; Watanabe, K.; Hoffmann, H., Pickering emulsions stabilized by novel clay-hydrophobin synergism. *Soft Matter* **2011,** *7* (22), 11021-11030.

102. Wu, W.; Chen, H.; Liu, C.; Wen, Y.; Yuan, Y.; Zhang, Y., Preparation of cyclohexanone/water Pickering emulsion together with modification of silica particles in the presence of PMHS by one pot method. *Colloids and Surfaces A: Physicochemical and Engineering Aspects* **2014,** *448*, 130-139.

103. Kpogbemabou, D.; Lecomte-Nana, G.; Aimable, A.; Bienia, M.; Niknam, V.; Carrion, C., Oil-in-water Pickering emulsions stabilized by phyllosilicates at high solid content. *Colloids and Surfaces A: Physicochemical and Engineering Aspects* **2014,** *463*, 85-92.

104. Liu, J.; Yin, D.; Zhang, S.; Liu, H.; Zhang, Q., Synthesis of polymeric core/shell microspheres with spherical virus-like surface morphology by Pickering emulsion. *Colloids and Surfaces A: Physicochemical and Engineering Aspects* **2015,** *466*, 174-180.

105. Cao, L.; Wang, X.; Meziani, M. J.; Lu, F. S.; Wang, H. F.; Luo, P. J. G.; Lin, Y.; Harruff, B. A.; Veca, L. M.; Murray, D.; Xie, S. Y.; Sun, Y. P., Carbon dots for multiphoton bioimaging. *Journal of the American Chemical Society* **2007,** *129* (37), 11318.

106. Chen, B. S.; Li, F. M.; Li, S. X.; Weng, W.; Guo, H. X.; Guo, T.; Zhang, X. Y.; Chen, Y. B.; Huang, T. T.; Hong, X. L.; You, S. Y.; Lin, Y. M.; Zeng, K. H.; Chen, S., Large scale synthesis of photoluminescent carbon nanodots and their application for bioimaging. *Nanoscale* **2013,** *5* (5), 1967-1971.

107. Ponomarenko, L. A.; Schedin, F.; Katsnelson, M. I.; Yang, R.; Hill, E. W.; Novoselov, K. S.; Geim, A. K., Chaotic dirac billiard in graphene quantum dots. *Science* **2008,** *320* (5874), 356-358.

108. Liu, F. P.; Wang, S.; Guan, J.; Wei, T.; Zeng, M. X.; Yang, S. F., Putting a Terbium-Monometallic Cyanide Cluster into the C-82 Fullerene Cage: TbCN@C-2(5)-C-82. *Inorganic Chemistry* **2014,** *53* (10), 5201-5205.

109. Yin, G. N.; Zheng, Z.; Wang, H. T.; Du, Q. G.; Zhang, H. D., Preparation of graphene oxide coated polystyrene microspheres by Pickering emulsion polymerization. *Journal of Colloid and Interface Science* **2013,** *394*, 192-198.

110. Landfester, K.; Bechthold, N.; Tiarks, F.; Antonietti, M., Miniemulsion polymerization with cationic and nonionic surfactants: A very efficient use of surfactants for heterophase polymerization. *Macromolecules* **1999,** *32* (8), 2679-2683.

111. Li, L. L.; Wu, G. H.; Yang, G. H.; Peng, J.; Zhao, J. W.; Zhu, J. J., Focusing on luminescent graphene quantum dots: current status and future perspectives. *Nanoscale* **2013,** *5* (10), 4015-4039.

112. Bourlinos, A. B.; Stassinopoulos, A.; Anglos, D.; Zboril, R.; Karakassides, M.; Giannelis, E. P., Surface functionalized carbogenic quantum dots. *Small* **2008,** *4* (4), 455-458.

113. Wang, J.; Wang, C. F.; Chen, S., Amphiphilic Egg-Derived Carbon Dots: Rapid Plasma Fabrication, Pyrolysis Process, and Multicolor Printing Patterns. *Angewandte Chemie International Edition* **2012,** *51* (37), 9297-9301.

114. Hodgson, D. M.; Man, S.; Powell, K. J.; Perko, Z.; Zeng, M. X.; Moreno-Clavijo, E.; Thompson, A. L.; Moore, M. D., Intramolecular Oxonium Ylide Formation-[2,3] Sigmatropic Rearrangement of Diazocarbonyl-Substituted Cyclic Unsaturated Acetals: A Formal Synthesis of Hyperolactone C. *Journal of Organic Chemistry* **2014,** *79* (20), 9728-9734.

115. Wu, W. T.; Zhang, Z. H.; Liebeskind, L. S., In Situ Carboxyl Activation Using a Silatropic Switch: A New Approach to Amide and Peptide Constructions. *Journal of the American Chemical Society* **2011,** *133* (36), 14256-14259.

116. Sk, M. A.; Ananthanarayanan, A.; Huang, L.; Lim, K. H.; Chen, P., Revealing the tunable photoluminescence properties of graphene quantum dots. *Journal of Material Chemistry C* **2014,** *2* (34), 6954-6960.

117. Liu, W. R.; Sun, D. J.; Li, C. F.; Liu, Q.; Xu, H., Formation and stability of paraffin oil-in-water nano-emulsions prepared by the emulsion inversion point method. *Journal of Colloid and Interface Science* **2006,** *303* (2), 557-563.

118. Binks, B. P.; Lumsdon, S. O., Catastrophic phase inversion of water-in-oil emulsions stabilized by hydrophobic silica. *Langmuir* **2000,** *16* (6), 2539-2547.

119. Tiarks, F.; Landfester, K.; Antonietti, M., Preparation of polymeric nanocapsules by miniemulsion polymerization. *Langmuir* **2001,** *17* (3), 908-918.

120. Lin, K. Y. A.; Yang, H. T.; Petit, C.; Lee, W. D., Magnetically controllable Pickering emulsion prepared by a reduced graphene oxide-iron oxide composite. *Journal of Colloid and Interface Science* **2015,** *438*, 296-305.

121. Kim, S. D.; Zhang, W. L.; Choi, H. J., Pickering emulsion-fabricated polystyrene-graphene oxide microspheres and their electrorheology. *Journal of Material Chemistry C* **2014,** *2* (36), 7541-7546.

122. Sun, J.; Bi, H., Pickering emulsion fabrication and enhanced supercapacity of graphene oxide-covered polyaniline nanoparticles. *Materials Letters* **2012,** *81*, 48-51.

123. Tang, M. Y.; Tao, W.; Xu, X. Y.; Lei, Z.; Fei, W., Factors that affect the stability, type and morphology of Pickering emulsion stabilized by silver nanoparticles/graphene oxide nanocomposites. *Materials Research Bullitin* **2014,** *60*, 118-129.

124. Zhai, W. Y.; Li, G. P.; Yu, P.; Yang, L. F.; Mao, L. Q., Silver Phosphate/Carbon Nanotube-Stabilized Pickering Emulsion for Highly Efficient Photocatalysis. *Journal of Physical Chemistry C* **2013,** *117* (29), 15183-15191.

125. Man, S. H. C.; Yusof, N. Y. M.; Whittaker, M. R.; Thickett, S. C.; Zetterlund, P. B., Influence of Monomer Type on Miniemulsion Polymerization Systems Stabilized by Graphene

Oxide as Sole Surfactant. *Journal of Polymer Science Part A-Polymer Chemistry* **2013,** *51* (23), 5153-5162.

126. Wang, Z.; Han, Q.; Xia, J.; Xia, L.; Ding, M.; Tang, J., Graphene-based solid-phase extraction disk for fast separation and preconcentration of trace polycyclic aromatic hydrocarbons from environmental water samples. *Journal of Separation Science* **2013,** *36* (11), 1834-1842.

127. Liu, Q.; Shi, J.; Zeng, L.; Wang, T.; Cai, Y.; Jiang, G., Evaluation of graphene as an advantageous adsorbent for solid-phase extraction with chlorophenols as model analytes. *Journal of Chromatography A* **2011,** *1218* (2), 197-204.

128. McManus, D.; Vranic, S.; Withers, F.; Sanchez-Romaguera, V.; Macucci, M.; Yang, H.; Sorrentino, R.; Parvez, K.; Son, S.-K.; Iannaccone, G.; Kostarelos, K.; Fiori, G.; Casiraghi, C., Water-based and biocompatible 2D crystal inks for all-inkjet-printed heterostructures. *Nature Nanotechnology* **2017,** *12* (4), 343.

129. Xiao, F.-X.; Miao, J.; Liu, B., Layer-by-layer self-assembly of CdS quantum dots/graphene nanosheets hybrid films for photoelectrochemical and photocatalytic applications. *Journal of the American Chemical Society* **2014,** *136* (4), 1559-1569.

130. Schlierf, A.; Yang, H.; Gebremedhn, E.; Treossi, E.; Ortolani, L.; Chen, L.; Minoia, A.; Morandi, V.; Samori, P.; Casiraghi, C., Nanoscale insight into the exfoliation mechanism of graphene with organic dyes: effect of charge, dipole and molecular structure. *Nanoscale* **2013,** *5* (10), 4205-4216.

131. He, P.; Sun, J.; Tian, S.; Yang, S.; Ding, S.; Ding, G.; Xie, X.; Jiang, M., Processable aqueous dispersions of graphene stabilized by graphene quantum dots. *Chemistry of Materials* **2014**, *27* (1), 218-226.

132. Xu, M.; Zhang, W.; Yang, Z.; Yu, F.; Ma, Y.; Hu, N.; He, D.; Liang, Q.; Su, Y.; Zhang, Y., One-pot liquid-phase exfoliation from graphite to graphene with carbon quantum dots. *Nanoscale* **2015,** *7* (23), 10527-10534.

133. Li, F.; Larock, R. C., Synthesis, Structure and Properties of New Tung Oil−Styrene−Divinylbenzene Copolymers Prepared by Thermal Polymerization. *Biomacromolecules* **2003,** *4* (4), 1018-1025.

134. Bhanu, V. A.; Kishore, K., Role of Oxygen in Polymerization Reactions. *Chemical Reviews* **1991,** *91* (2), 99-117.

135. Zhao, J.; Holmes, M. A.; Osterloh, F. E., Quantum confinement controls photocatalysis: a free energy analysis for photocatalytic proton reduction at CdSe nanocrystals. *ACS Nano* **2013,** *7* (5), 4316-4325.

136. Shen, J.; Zhu, Y.; Chen, C.; Yang, X.; Li, C., Facile preparation and upconversion luminescence of graphene quantum dots. *Chemical Communications* **2011,** *47* (9), 2580-2582.

137. Peng, J.; Gao, W.; Gupta, B. K.; Liu, Z.; Romero-Aburto, R.; Ge, L.; Song, L.; Alemany, L. B.; Zhan, X.; Gao, G., Graphene quantum dots derived from carbon fibers. *Nano Letters* **2012,** *12* (2), 844-849.

138. Parviz, D.; Irin, F.; Shah, S. A.; Das, S.; Sweeney, C. B.; Green, M. J., Challenges in Liquid-Phase Exfoliation, Processing, and Assembly of Pristine Graphene. *Advanced Materials* **2016,** *28* (40), 8796-8818.

139. Wang, H.; Chen, Z.; Xin, L.; Cui, J.; Zhao, S.; Yan, Y., Synthesis of pyrene-capped polystyrene by free radical polymerization and its application in direct exfoliation of graphite into graphene nanosheets. *Journal of Polymer Science Part A: Polymer Chemistry* **2015,** *53* (18), 2175-2185.

140. English, A. R.; Voeltz, G. K., Rab10 GTPase regulates ER dynamics and morphology. *Nature Cell Biology* **2013,** *15* (2), 169-178.

141. Bahrami, A. H.; Hummer, G., Formation and Stability of Lipid Membrane Nanotubes. *ACS Nano* **2017,** *11* (9), 9558-9565.

142. Huang, C.; Forth, J.; Wang, W.; Hong, K.; Smith, G. S.; Helms, B. A.; Russell, T. P., Bicontinuous structured liquids with sub-micrometre domains using nanoparticle surfactants. *Nature Nanotechnology* **2017,** *12* (11), 1060.

143. Lv, N.; Zhang, J.; Li, G.; Wang, X.; Ni, J., Novel Strategy for Facile Synthesis of C-Shaped CeO2 Nanotubes with Enhanced Catalytic Properties. *The Journal of Physical Chemistry C* **2017,** *121* (21), 11926-11931.

144. Witt, J.; Mumm, D.; Mohraz, A., Microstructural tunability of co-continuous bijel-derived electrodes to provide high energy and power densities. *Journal of Materials Chemistry A* **2016,** *4* (3), 1000-1007.

145. Lee, M. N.; Thijssen, J. H.; Witt, J. A.; Clegg, P. S.; Mohraz, A., Making a robust interfacial scaffold: bijel rheology and its link to processability. *Advanced Functional Materials* **2013,** *23* (4), 417-423.

146. Ziguang, Z.; Kangjun, Z.; Yuxia, L.; Jiajia, Z.; Mingjie, L., Highly Stretchable, Shape Memory Organohydrogels Using Phase-Transition Microinclusions. *Advanced Materials* **2017,** *29* (33), 1701695.

147. Creighton, M. A.; Zhu, W.; van Krieken, F.; Petteruti, R. A.; Gao, H.; Hurt, R. H., Three-Dimensional Graphene-Based Microbarriers for Controlling Release and Reactivity in Colloidal Liquid Phases. *ACS Nano* **2016,** *10* (2), 2268-2276.

148. Wang, X.; Zeng, M.; Yu, Y.-H.; Wang, H.; Mannan, M. S.; Cheng, Z., Thermosensitive ZrP-PNIPAM Pickering Emulsifier and the Controlled-Release Behavior. *ACS Applied Materials & Interfaces* **2017,** *9* (8), 7852-7858.

149. Ramachandran, S.; Al-Muntasheri, G.; Leal, J.; Wang, Q. In *Corrosion and Scale Formation in High Temperature Sour Gas Wells: Chemistry and Field Practice*, SPE International Symposium on Oilfield Chemistry, Society of Petroleum Engineers: **2015** (April).

150. Deng, J.; Lu, X.; Constant, C.; Dogariu, A.; Fang, J., Design of β-CD–surfactant complex-coated liquid crystal droplets for the detection of cholic acid via competitive host–guest recognition. *Chemical Communications* **2015,** *51* (43), 8912-8915.

151. Gu, C.; Botto, L., Direct calculation of anisotropic surface stresses during deformation of a particle-covered drop. *Soft Matter* **2016,** *12* (3), 705-716.

152. Zeng, M.; Shah, S. A.; Huang, D.; Parviz, D.; Yu, Y.-H.; Wang, X.; Green, M. J.; Cheng, Z., Aqueous exfoliation of graphite into graphene assisted by sulfonyl graphene quantum dots for photonic crystal applications. *ACS Applied Materials & Interfaces* **2017**, *9* (36), 30797-30804.

153. Yu, Y.-H.; Chen, Y.-P.; Zeng, M.; Cheng, Z., Microwave-assisted rapid synthesis of hexagonal α-zirconium phosphate nanodisks as a Pickering emulsion stabilizer. *Materials Letters* **2016,** *163*, 158-161.

154. Zeng, M.; Shah, S. A.; Huang, D.; Parviz, D.; Yu, Y.-H.; Wang, X.; Green, M. J.; Cheng, Z., Aqueous exfoliation of graphite into graphene assisted by sulfonyl graphene quantum dots for photonic crystal applications. *ACS Applied Materials & Interfaces* **2017,** *9* (36), 30797-30804.

155. Zeng, M.; Wang, P.; Luo, J.; Peng, B.; Ding, B.; Zhang, L.; Wang, L.; Huang, D.; Echols, I.; Abo Deeb, E.; Bordovsky, E.; Choi, C.-H.; Ybanez, C.; Meras, P.; Situ, E.; Mannan, M. S.; Cheng, Z., Hierarchical, Self-Healing and Superhydrophobic Zirconium Phosphate Hybrid Membrane Based on the Interfacial Crystal Growth of Lyotropic 2D Nanoplatelets. *ACS Applied Materials & Interfaces* **2018**, *10* (26), 22793–22800

156. Kirillova, A.; Stoychev, G.; Ionov, L.; Eichhorn, K. J.; Malanin, M.; Synytska, A., Platelet Janus Particles with Hairy Polymer Shells for Multifunctional Materials. *ACS Applied Materials & Interfaces* **2014,** *6* (15), 13106-13114.

157. Liu, J.; Liu, G.; Zhang, M.; Sun, P.; Zhao, H., Synthesis and self-assembly of amphiphilic Janus laponite disks. *Macromolecules* **2013,** *46* (15), 5974-5984.

158. Yang, H.; Liang, F.; Wang, X.; Chen, Y.; Zhang, C.; Wang, Q.; Qu, X.; Li, J.; Wu, D.; Yang, Z., Responsive Janus composite nanosheets. *Macromolecules* **2013,** *46* (7), 2754-2759.

159. Yukselen, Y.; Kaya, A., Zeta potential of kaolinite in the presence of alkali, alkaline earth and hydrolyzable metal ions. *Water, Air, and Soil Pollution* **2003,** *145* (1-4), 155-168.

160. Vane, L. M.; Zang, G. M., Effect of aqueous phase properties on clay particle zeta potential and electro-osmotic permeability: Implications for electro-kinetic soil remediation processes. *Journal of Hazardous Materials* **1997,** *55* (1-3), 1-22.

161. Binks, B.; Lumsdon, S., Catastrophic phase inversion of water-in-oil emulsions stabilized by hydrophobic silica. *Langmuir* **2000,** *16* (6), 2539-2547.

162. Chen, Y. C.; Dimonie, V.; El-Aasser, M. S., Effect of interfacial phenomena on the development of particle morphology in a polymer latex system. *Macromolecules* **1991,** *24* (13), 3779-3787.

163. Kinlen, P.; Liu, J.; Ding, Y.; Graham, C.; Remsen, E., Emulsion polymerization process for organically soluble and electrically conducting polyaniline. *Macromolecules* **1998,** *31* (6), 1735-1744.

164. Castellón, E.; Zayat, M.; Levy, D., Molecular configuration transitions of a nematic liquid crystal encapsulated in organically modified silicas. *Physical Chemistry Chemical Physics* **2009,** *11* (29), 6234-6241.

165. Khan, W.; Park, S.-Y., Configuration change of liquid crystal microdroplets coated with a novel polyacrylic acid block liquid crystalline polymer by protein adsorption. *Lab on a Chip* **2012,** *12* (21), 4553-4559.

166. Wang, L.; Li, Q., Stimuli-Directing Self-Organized 3D Liquid-Crystalline Nanostructures: From Materials Design to Photonic Applications. *Advanced Functional Materials* **2016,** *26* (1), 10-28.

167. Lee, H.-G.; Munir, S.; Park, S.-Y., Cholesteric liquid crystal droplets for biosensors. *ACS Applied Materials & Interfaces* **2016,** *8* (39), 26407-26417.

168. Dukhin, S. S.; Kretzschmar, G.; Miller, R., *Dynamics of Adsorption at Liquid Interfaces: Theory, Experiment, Application*. Elsevier: **1995**; Vol. 1.

169. Cheng, S.; Vachon, R., A technique for predicting the thermal conductivity of suspensions, emulsions and porous materials. *International Journal of Heat and Mass Transfer* **1970,** *13* (3), 537-546.

170. Verma, L.; Shrotriya, A.; Singh, R.; Chaudhary, D., Thermal conduction in two-phase materials with spherical and non-spherical inclusions. *Journal of Physics D: Applied Physics* **1991,** *24* (10), 1729.

171. Volgraf, M.; Gorostiza, P.; Numano, R.; Kramer, R. H.; Isacoff, E. Y.; Trauner, D., Allosteric control of an ionotropic glutamate receptor with an optical switch. *Nature Chemical Biology* **2006,** *2* (1), 47.

172. Creighton, M. A.; Zhu, W.; Van Krieken, F.; Petteruti, R. A.; Gao, H.; Hurt, R. H., Three-Dimensional Graphene-Based Microbarriers for Controlling Release and Reactivity in Colloidal Liquid Phases. *ACS Nano* **2016**, *10* (2), 2268–2276

173. Gelebart, A. H.; Jan, M. D.; Varga, M.; Konya, A.; Vantomme, G.; Meijer, E.; Selinger, R. L.; Broer, D. J., Making waves in a photoactive polymer film. *Nature* **2017,** *546* (7660), 632.

174. Luo, J.; Zeng, M.; Peng, B.; Tang, Y.; zhang, l.; Wang, P.; He, L.; Huang, D.; Wang, L.; Wang, X.; Chen, M.; Lei, S.; Lin, P.; Chen, Y.; Cheng, Z., Electrostatic-driven Dynamic Jamming of 2D Nanoparticles at Interfaces for Controlled Molecular Diffusion. *Angewandte Chemie International Edition* **2018**, *130* (36), 11926-11931.

175. Ma, X.; Hahn, K.; Sanchez, S., Catalytic Mesoporous Janus Nanomotors for Active Cargo Delivery. *Journal of the American Chemical Society* **2015,** *137* (15), 4976-4979.

176. Soler, L.; Magdanz, V.; Fomin, V. M.; Sanchez, S.; Schmidt, O. G., Self-Propelled Micromotors for Cleaning Polluted Water. *ACS Nano* **2013,** *7* (11), 9611-9620.

177. Wu, J.; Balasubramanian, S.; Kagan, D.; Manesh, K. M.; Campuzano, S.; Wang, J., Motion-based DNA detection using catalytic nanomotors. *Nature Communications* **2010,** *1*, 36.

178. Tu, Y.; Peng, F.; Sui, X.; Men, Y.; White, P. B.; van Hest, J. C.; Wilson, D. A., Self-propelled supramolecular nanomotors with temperature-responsive speed regulation. *Nature Chemistry* **2017,** *9* (5), 480.

179. Xuan, M.; Mestre, R.; Gao, C.; Zhou, C.; He, Q.; Sanchez, S., Non-Continuous Super-Diffusive Dynamics of Light-Activated Nanobottle Motor. *Angewandte Chemie International Edition* **2018**, *57* (23), 6838-6842.

180. Vilela, D.; Parmar, J.; Zeng, Y.; Zhao, Y.; Sánchez, S., Graphene-based microbots for toxic heavy metal removal and recovery from water. *Nano Letters* **2016,** *16* (4), 2860-2866.

181. Li, J.; Gao, W.; Dong, R.; Pei, A.; Sattayasamitsathit, S.; Wang, J., Nanomotor lithography. *Nature Communications* **2014,** *5*, 5026.

182. Golestanian, R.; Liverpool, T.; Ajdari, A., Designing phoretic micro-and nano-swimmers. *New Journal of Physics* **2007,** *9* (5), 126.

183. Ebbens, S.; Tu, M.-H.; Howse, J. R.; Golestanian, R., Size dependence of the propulsion velocity for catalytic Janus-sphere swimmers. *Physical Review E* **2012,** *85* (2), 20401.

184. Nourhani, A.; Lammert, P. E., Geometrical performance of self-phoretic colloids and microswimmers. *Physical Review Letters* **2016,** *116* (17), 178302.

185. Kline, T. R.; Paxton, W. F.; Mallouk, T. E.; Sen, A., Catalytic nanomotors: remote-controlled autonomous movement of striped metallic nanorods. *Angewandte Chemie International Edition* **2005,** *44* (5), 744-746.

186. Li, R.-Z.; Hu, A.; Bridges, D.; Zhang, T.; Oakes, K. D.; Peng, R.; Tumuluri, U.; Wu, Z.; Feng, Z., Robust Ag nanoplate ink for flexible electronics packaging. *Nanoscale* **2015,** *7* (16), 7368-7377.

187. Lu, X.; Feng, X.; Werber, J. R.; Chu, C.; Zucker, I.; Kim, J.-H.; Osuji, C. O.; Elimelech, M., Enhanced antibacterial activity through the controlled alignment of graphene oxide nanosheets. *Proceedings of the National Academy of Sciences* **2017**, 201710996

188. Lee, T.-C.; Alarcón-Correa, M.; Miksch, C.; Hahn, K.; Gibbs, J. G.; Fischer, P., Self-propelling nanomotors in the presence of strong Brownian forces. *Nano Letters* **2014,** *14* (5), 2407-2412.

189. Abbot, J.; Brown, D. G., Stabilization of iron-catalysed hydrogen peroxide decomposition by magnesium. *Canadian Journal of Chemistry* **1990,** *68* (9), 1537-1543.

190. Shahwan, T.; Sirriah, S. A.; Nairat, M.; Boyacı, E.; Eroğlu, A. E.; Scott, T. B.; Hallam, K. R., Green synthesis of iron nanoparticles and their application as a Fenton-like catalyst for the degradation of aqueous cationic and anionic dyes. *Chemical Engineering Journal* **2011,** *172* (1), 258-266.

191. Malik, P. K.; Saha, S. K., Oxidation of direct dyes with hydrogen peroxide using ferrous ion as catalyst. *Separation and Purification Technology* **2003,** *31* (3), 241-250.

192. Vukusic, P.; Sambles, J. R., Photonic structures in biology. *Nature* **2003,** *424* (6950), 852-855.

193. Parker, A. R.; Townley, H. E., Biomimetics of photonic nanostructures. *Nature Nanotechnology* **2007,** *2* (6), 347-353.

194. Parker, A. R., A geological history of reflecting optics. *Journal of the Royal Society Interface* **2005,** *2* (2), 1-17.

195. Holtz, J. H.; Asher, S. A., Polymerized colloidal crystal hydrogel films as intelligent chemical sensing materials. *Nature* **1997,** *389* (6653), 829-832.

196. Kelly, J. A.; Shukaliak, A. M.; Cheung, C. C.; Shopsowitz, K. E.; Hamad, W. Y.; MacLachlan, M. J., Responsive photonic hydrogels based on nanocrystalline cellulose. *Angewandte Chemie International Edition* **2013,** *52* (34), 8912-8916.

197. Finnemore, A.; Cunha, P.; Shean, T.; Vignolini, S.; Guldin, S.; Oyen, M.; Steiner, U., Biomimetic layer-by-layer assembly of artificial nacre. *Nature Communications* **2012,** *3*, 966.

198. Li, Z.; Okasinski, J. S.; Gosztola, D. J.; Ren, Y.; Sun, Y., Silver chlorobromide nanocubes with significantly improved uniformity: synthesis and assembly into photonic crystals. *Journal of Material Chemistry C* **2015,** *3* (1), 58-65.

199. Giese, M.; Blusch, L. K.; Khan, M. K.; Hamad, W. Y.; MacLachlan, M. J., Responsive Mesoporous Photonic Cellulose Films by Supramolecular Cotemplating. *Angewandte Chemie International Edition* **2014,** *53* (34), 8880-8884.

200. Zhang, W.; Anaya, M.; Lozano, G.; Calvo, M. E.; Johnston, M. B.; M ǵuez, H. n.; Snaith, H. J., Highly efficient perovskite solar cells with tunable structural color. *Nano Letters* **2015,** *15* (3), 1698-1702.

201. Wu, S.; Liu, B.; Su, X.; Zhang, S., Structural Color Patterns on Paper Fabricated by Inkjet Printer and Their Application in Anti-Counterfeiting. *The Journal of Physical Chemistry Letters* **2017**.

202. Li, P.; Wong, M.; Zhang, X.; Yao, H.; Ishige, R.; Takahara, A.; Miyamoto, M.; Nishimura, R.; Sue, H.-J., Tunable lyotropic photonic liquid crystal based on graphene oxide. *ACS Photonics* **2014,** *1* (1), 79-86.

203. Shen, T.-Z.; Hong, S.-H.; Lee, B.; Song, J.-K., Bottom-up and top-down manipulations for multi-order photonic crystallinity in a graphene-oxide colloid. *NPG Asia Materials* **2016,** *8* (8), e296.

204. Shopsowitz, K. E.; Qi, H.; Hamad, W. Y.; MacLachlan, M. J., Free-standing mesoporous silica films with tunable chiral nematic structures. *Nature* **2010,** *468* (7322), 422-425.

205. van der Kooij, F. M.; Kassapidou, K.; Lekkerkerker, H. N., Liquid crystal phase transitions in suspensions of polydisperse plate-like particles. *Nature* **2000,** *406* (6798), 868-871.

206. Shuai, M.; Mejia, A. F.; Chang, Y.-W.; Cheng, Z., Hydrothermal synthesis of layered [small alpha]-zirconium phosphate disks: control of aspect ratio and polydispersity for nano-architecture. *CrystEngComm* **2013,** *15* (10), 1970-1977.

207. Mejia, A. F.; Chang, Y. W.; Ng, R.; Shuai, M.; Mannan, M. S.; Cheng, Z. D., Aspect ratio and polydispersity dependence of isotropic-nematic transition in discotic suspensions. *Physical Review E* **2012,** *85* (6), 61708.

208. Wong, M. H.; Ishige, R.; Hoshino, T.; Hawkins, S.; Li, P.; Takahara, A.; Sue, H. J., Solution Processable Iridescent Self-Assembled Nanoplatelets with Finely Tunable Interlayer Distances Using Charge- and Sterically Stabilizing Oligomeric Polyoxyalkyleneamine Surfactants. *Chemistry of Materials* **2014,** *26* (4), 1528-1537.

209. Schenk, F.; Wilts, B. D.; Stavenga, D. G., The Japanese jewel beetle: a painter's challenge. *Bioinspiration & Biomimetics* **2013,** *8* (4), 45002.

210. Forster, J. D.; Noh, H.; Liew, S. F.; Saranathan, V.; Schreck, C. F.; Yang, L.; Park, J. G.; Prum, R. O.; Mochrie, S. G.; O'Hern, C. S., Biomimetic isotropic nanostructures for structural coloration. *Advanced Materials* **2010,** *22* (26-27), 2939-2944.

211. Kleshchanok, D.; Holmqvist, P.; Meijer, J.-M.; Lekkerkerker, H. N. W., Lyotropic Smectic B Phase Formed in Suspensions of Charged Colloidal Platelets. *Journal of the American Chemical Society* **2012,** *134* (13), 5985-5990.

212. Vis, M.; Wensink, H.; Lekkerkerker, H.; Kleshchanok, D., Nematic and lamellar liquid-crystalline phases in suspensions of charged silica-coated gibbsite platelets. *Molecular Physics* **2014**, *113* (9-10), 1053-1060.

213. Lee, H. S.; Shim, T. S.; Hwang, H.; Yang, S.-M.; Kim, S.-H., Colloidal photonic crystals toward structural color palettes for security materials. *Chemistry of Materials* **2013,** *25* (13), 2684-2690.

214. Yang, D.; Ye, S.; Ge, J., Solvent wrapped metastable colloidal crystals: highly mutable colloidal assemblies sensitive to weak external disturbance. *Journal of the American Chemical Society* **2013,** *135* (49), 18370-18376.

215. Sun, X.; Luo, D.; Liu, J.; Evans, D. G., Monodisperse chemically modified graphene obtained by density gradient ultracentrifugal rate separation. *ACS Nano* **2010,** *4* (6), 3381-3389.

216. Pusey, P.; Van Megen, W., Phase behaviour of concentrated suspensions of nearly hard colloidal spheres. *Nature* **1986,** *320* (6060), 340-342.

217. Segad, M.; Cabane, B.; Jönsson, B., Reactivity, swelling and aggregation of mixed-size silicate nanoplatelets. *Nanoscale* **2015,** *7* (39), 16290-16297.

218. Segad, M., Microstructure determination of IQ-WB clays: a direct procedure by small-angle X-ray scattering. *Journal of Applied Crystallography* **2013,** *46* (5), 1316-1322.

219. Liu, M.; Ishida, Y.; Ebina, Y.; Sasaki, T.; Hikima, T.; Takata, M.; Aida, T., An anisotropic hydrogel with electrostatic repulsion between cofacially aligned nanosheets. *Nature* **2015,** *517* (7532), 68-72.

220. Kintisch, E., An audacious decision in crisis gets cautious praise. *Science* **2010,** *329* (5993), 735-736.

221. Shannon, M. A.; Bohn, P. W.; Elimelech, M.; Georgiadis, J. G.; Marinas, B. J.; Mayes, A. M., Science and technology for water purification in the coming decades. *Nature* **2008,** *452* (7185), 301-310.

222. Zhang, L.; Zhang, Z.; Wang, P., Smart surfaces with switchable superoleophilicity and superoleophobicity in aqueous media: toward controllable oil/water separation. *NPG Asia Materials* **2012,** *4* (2), e8.

223. Wang, S. H.; Li, M.; Lu, Q. H., Filter Paper with Selective Absorption and Separation of Liquids that Differ in Surface Tension. *ACS Applied Materials & Interfaces* **2010,** *2* (3), 677-683.

224. Zhu, J.; Li, H.; Du, J.; Ren, W.; Guo, P.; Xu, S.; Wang, J., A robust and coarse surface mesh modified by interpenetrating polymer network hydrogel for oil-water separation. *Journal of Applied Polymer Science* **2015,** *132* (19), 41949.

225. Ju, J.; Wang, T.; Wang, Q., A facile approach in fabricating superhydrophobic and superoleophilic poly (vinylidene fluoride) membranes for efficient water–oil separation. *Journal of Applied Polymer Science* **2015,** *132* (24), 42077.

226. Wang, X. Z.; Zhang, L. C.; Yu, Y. H.; Jia, L. S.; Mannan, M. S.; Chen, Y.; Cheng, Z. D., Nano-encapsulated PCM via Pickering Emulsification. *Scientific Reports* **2015,** *5*, 13357.

227. Wang, J.; Chen, Y., Oil–water separation capability of superhydrophobic fabrics fabricated via combining polydopamine adhesion with lotus-leaf-like structure. *Journal of Applied Polymer Science* **2015,** *132* (39), 42614.

228. Wang, Y.; Shi, Y.; Pan, L.; Yang, M.; Peng, L.; Zong, S.; Shi, Y.; Yu, G., Multifunctional superhydrophobic surfaces templated from innately microstructured hydrogel matrix. *Nano Letters* **2014,** *14* (8), 4803-4809.

229. Ma, W.; Zhang, Q.; Hua, D.; Xiong, R.; Zhao, J.; Rao, W.; Huang, S.; Zhan, X.; Chen, F.; Huang, C., Electrospun fibers for oil-water separation. *RSC Advances* **2016,** *6* (16), 12868-12884.

230. Liu, Y. W.; Zhang, C. H.; Wang, Z. Q.; Fu, X.; Wei, R., Scaly bionic structures constructed on a polyester fabric with anti-fouling and anti-bacterial properties for highly efficient oil-water separation. *RSC Advances* **2016,** *6* (90), 87332-87340.

231. Zhou, X.; Zhang, Z.; Xu, X.; Guo, F.; Zhu, X.; Men, X.; Ge, B., Robust and durable superhydrophobic cotton fabrics for oil/water separation. *ACS Applied Materials & Interfaces* **2013,** *5* (15), 7208-7214.

232. Wang, B.; Li, J.; Wang, G.; Liang, W.; Zhang, Y.; Shi, L.; Guo, Z.; Liu, W., Methodology for robust superhydrophobic fabrics and sponges from in situ growth of transition metal/metal oxide nanocrystals with thiol modification and their applications in oil/water separation. *ACS Applied Materials & Interfaces* **2013,** *5* (5), 1827-1839.

233. Li, J.; Li, D.; Yang, Y.; Li, J.; Zha, F.; Lei, Z., A prewetting induced underwater superoleophobic or underoil (super) hydrophobic waste potato residue-coated mesh for selective efficient oil/water separation. *Green Chemistry* **2016,** *18* (2), 541-549.

234. Xue, Z.; Wang, S.; Lin, L.; Chen, L.; Liu, M.; Feng, L.; Jiang, L., A novel superhydrophilic and underwater superoleophobic hydrogel-coated mesh for oil/water separation. *Advanced Materials* **2011,** *23* (37), 4270-4273.

235. Cao, Y.; Zhang, X.; Tao, L.; Li, K.; Xue, Z.; Feng, L.; Wei, Y., Mussel-inspired chemistry and michael addition reaction for efficient oil/water separation. *ACS Applied Materials & Interfaces* **2013,** *5* (10), 4438-4442.

236. Zhang, F.; Zhang, W. B.; Shi, Z.; Wang, D.; Jin, J.; Jiang, L., Nanowire-Haired Inorganic Membranes with Superhydrophilicity and Underwater Ultralow Adhesive Superoleophobicity for High-Efficiency Oil/Water Separation. *Advanced Materials* **2013,** *25* (30), 4192-4198.

237. Luo, Z.-Y.; Chen, K.-X.; Wang, J.-H.; Mo, D.-C.; Lyu, S.-S., Hierarchical nanoparticle-induced superhydrophilic and under-water superoleophobic Cu foam with ultrahigh

water permeability for effective oil/water separation. *Journal of Materials Chemistry A* **2016,** *4* (27), 10566-10574.

238. Liu, C.-T.; Liu, Y.-L., pH-Induced switches of the oil- and water-selectivity of crosslinked polymeric membranes for gravity-driven oil-water separation. *Journal of Materials Chemistry A* **2016,** *4* (35), 13543-13548.

239. Zhang, W.; Lu, X.; Xin, Z.; Zhou, C., A self-cleaning polybenzoxazine/TiO2 surface with superhydrophobicity and superoleophilicity for oil/water separation. *Nanoscale* **2015,** *7* (46), 19476-19483.

240. Zhang, J.; Seeger, S., Polyester materials with superwetting silicone nanofilaments for oil/water separation and selective oil absorption. *Advanced Functional Materials* **2011,** *21* (24), 4699-4704.

241. Zhang, W.; Zhu, Y.; Liu, X.; Wang, D.; Li, J.; Jiang, L.; Jin, J., Salt-Induced Fabrication of Superhydrophilic and Underwater Superoleophobic PAA-g-PVDF Membranes for Effective Separation of Oil-in-Water Emulsions. *Angewandte Chemie International Edition* **2014,** *53* (3), 856-860.

242. Lee, S. E.; Kim, H.-J.; Lee, S.-H.; Choi, D.-G., Superamphiphobic Surface by Nanotransfer Molding and Isotropic Etching. *Langmuir* **2013,** *29* (25), 8070-8075.

243. Choi, H.-J.; Choo, S.; Shin, J.-H.; Kim, K.-I.; Lee, H., Fabrication of Superhydrophobic and Oleophobic Surfaces with Overhang Structure by Reverse Nanoimprint Lithography. *The Journal of Physical Chemistry C* **2013,** *117* (46), 24354-24359.

244. Latthe, S. S.; Terashima, C.; Nakata, K.; Sakai, M.; Fujishima, A., Development of sol–gel processed semi-transparent and self-cleaning superhydrophobic coatings. *Journal of Materials Chemistry A* **2014,** *2* (15), 5548-5553.

245. Aruna, S.; Binsy, P.; Richard, E.; Basu, B. J., Properties of phase separation method synthesized superhydrophobic polystyrene films. *Applied Surface Science* **2012,** *258* (7), 3202-3207.

246. Yao, L.; He, J., Facile dip-coating approach to fabrication of mechanically robust hybrid thin films with high transmittance and durable superhydrophilicity. *Journal of Materials Chemistry A* **2014,** *2* (19), 6994-7003.

247. Bolto, B.; Tran, T.; Hoang, M.; Xie, Z., Crosslinked poly (vinyl alcohol) membranes. *Progress in Polymer Science* **2009,** *34* (9), 969-981.

248. Bonakdar, S.; Emami, S. H.; Shokrgozar, M. A.; Farhadi, A.; Ahmadi, S. A. H.; Amanzadeh, A., Preparation and characterization of polyvinyl alcohol hydrogels crosslinked by biodegradable polyurethane for tissue engineering of cartilage. *Materials Science and Engineering: C* **2010,** *30* (4), 636-643.

249. Gao, Z.; Gu, J.; Wang, X.; Li, Z.; Bai, X., FTIR and XPS study of the reaction of phenyl isocyanate and cellulose with different moisture contents. *Pigment & Resin Technology* **2005,** *34* (5), 282-289.

250. Deng, X.; Mammen, L.; Butt, H.-J.; Vollmer, D., Candle soot as a template for a transparent robust superamphiphobic coating. *Science* **2012,** *335* (6064), 67-70.

251. Tanaka, Y.; Reig, M.; Casas, S.; Aladjem, C.; Cortina, J. L., Computer simulation of ion-exchange membrane electrodialysis for salt concentration and reduction of RO discharged brine for salt production and marine environment conservation. *Desalination* **2015,** *367*, 76-89.

252. Altshuller, A.; Everson, H., The solubility of ethyl acetate in water. *Journal of the American Chemical Society* **1953,** *75* (7), 1727-1727.

253. Zhang, W.; Shi, Z.; Zhang, F.; Liu, X.; Jin, J.; Jiang, L., Superhydrophobic and superoleophilic PVDF membranes for effective separation of water-in-oil emulsions with high flux. *Advanced Materials* **2013,** *25* (14), 2071-2076.

254. Quintero, S. M. M.; Cremona, M.; Triques, A.; d'Almeida, A.; Braga, A., Swelling and morphological properties of poly (vinyl alcohol)(PVA) and poly (acrylic acid)(PAA) hydrogels in solution with high salt concentration. *Polymer* **2010,** *51* (4), 953-958.

255. Li, H.-J.; Cao, Y.-M.; Qin, J.-J.; Jie, X.-M.; Wang, T.-H.; Liu, J.-H.; Yuan, Q., Development and characterization of anti-fouling cellulose hollow fiber UF membranes for oil–water separation. *Journal of Membrane Science* **2006,** *279* (1–2), 328-335.

256. Lobo, A.; Cambiella, Á.; Benito, J. M.; Pazos, C.; Coca, J., Ultrafiltration of oil-in-water emulsions with ceramic membranes: Influence of pH and crossflow velocity. *Journal of Membrane Science* **2006,** *278* (1–2), 328-334.

257. Gutiérrez, G.; Lobo, A.; Benito, J. M.; Coca, J.; Pazos, C., Treatment of a waste oil-in-water emulsion from a copper-rolling process by ultrafiltration and vacuum evaporation. *Journal of Hazardous Materials* **2011,** *185* (2–3), 1569-1574.

258. Xu, Z.; Parra, D.; Gómez, D.; Salinas, I.; Zhang, Y.-A.; von Gersdorff Jørgensen, L.; Heinecke, R. D.; Buchmann, K.; LaPatra, S.; Sunyer, J. O., Teleost skin, an ancient mucosal surface that elicits gut-like immune responses. *Proceedings of the National Academy of Sciences* **2013,** *110* (32), 13097-13102.

259. Salinas, I.; Zhang, Y.-A.; Sunyer, J. O., Mucosal immunoglobulins and B cells of teleost fish. *Developmental & Comparative Immunology* **2011,** *35* (12), 1346-1365.

260. Tacchi, L.; Musharrafieh, R.; Larragoite, E. T.; Crossey, K.; Erhardt, E. B.; Martin, S. A.; LaPatra, S. E.; Salinas, I., Nasal immunity is an ancient arm of the mucosal immune system of vertebrates. *Nature Communications* **2014,** *5*, 5205.

261. Balebona, M.; Morinigo, M.; Faris, A.; Krovacek, K.; Månsson, I.; Bordas, M.; Borrego, J., Influence of salinity and pH on the adhesion of pathogenic Vibrio strains to Sparus aurata skin mucus. *Aquaculture* **1995,** *132* (1-2), 113-120.

262. Venkataraman, P.; Tang, J.; Frenkel, E.; McPherson, G. L.; He, J.; Raghavan, S. R.; Kolesnichenko, V.; Bose, A.; John, V. T., Attachment of a hydrophobically modified biopolymer at the oil–water interface in the treatment of oil spills. *ACS Applied Materials & Interfaces* **2013,** *5* (9), 3572-3580.

263. Nevárez, L. M.; Casarrubias, L. B.; Canto, O. S.; Celzard, A.; Fierro, V.; Gómez, R. I.; Sánchez, G. G., Biopolymers-based nanocomposites: Membranes from propionated lignin and cellulose for water purification. *Carbohydrate Polymers* **2011,** *86* (2), 732-741.

264. Lu, L.; Chen, W., Supramolecular self-assembly of biopolymers with carbon nanotubes for biomimetic and bio-inspired sensing and actuation. *Nanoscale* **2011,** *3* (6), 2412-2420.

265. Lee, H.-Y.; Tiwari, K. R.; Raghavan, S. R., Biopolymer capsules bearing polydiacetylenic vesicles as colorimetric sensors of pH and temperature. *Soft Matter* **2011,** *7* (7), 3273-3276.

266. Okamoto, M.; John, B., Synthetic biopolymer nanocomposites for tissue engineering scaffolds. *Progress in Polymer Science* **2013,** *38* (10), 1487-1503.

267. Matson, J. B.; Stupp, S. I., Self-assembling peptide scaffolds for regenerative medicine. *Chemical Communications* **2012,** *48* (1), 26-33.

268. Jayarama Reddy, V.; Radhakrishnan, S.; Ravichandran, R.; Mukherjee, S.; Balamurugan, R.; Sundarrajan, S.; Ramakrishna, S., Nanofibrous structured biomimetic strategies for skin tissue regeneration. *Wound Repair and Regeneration* **2013,** *21* (1), 1-16.

269. Hanani, Z. N.; Roos, Y.; Kerry, J., Use and application of gelatin as potential biodegradable packaging materials for food products. *International Journal of Biological Macromolecules* **2014,** *71*, 94-102.

270. Acosta, S.; Jiménez, A.; Cháfer, M.; González-Martínez, C.; Chiralt, A., Physical properties and stability of starch-gelatin based films as affected by the addition of esters of fatty acids. *Food Hydrocolloids* **2015,** *49*, 135-143.

271. Fabra, M.; Jiménez, A.; Atarés, L.; Talens, P.; Chiralt, A., Effect of fatty acids and beeswax addition on properties of sodium caseinate dispersions and films. *Biomacromolecules* **2009,** *10* (6), 1500-1507.

272. Kollarigowda, R. H.; Abraham, S.; Montemagno, C., Anti-fouling Cellulose Hybrid Bio-membrane for Effective Oil/Water Separation. *ACS Applied Materials & Interfaces* **2017**, *9* (35), 29812-29819.

273. Jeon, J. H.; Cheedarala, R. K.; Kee, C. D.; Oh, I. K., Dry-type artificial muscles based on pendent sulfonated chitosan and functionalized graphene oxide for greatly enhanced ionic interactions and mechanical stiffness. *Advanced Functional Materials* **2013,** *23* (48), 6007-6018.

274. Chen, S.; Chinnathambi, S.; Shi, X.; Osaka, A.; Zhu, Y.; Hanagata, N., Fabrication of novel collagen-silica hybrid membranes with tailored biodegradation and strong cell contact guidance ability. *Journal of Material Chemistry* **2012,** *22* (41), 21885-21892.

275. Wang, B.; Liang, W.; Guo, Z.; Liu, W., Biomimetic super-lyophobic and super-lyophilic materials applied for oil/water separation: a new strategy beyond nature. *Chemical Society Reviews* **2015,** *44* (1), 336-361.

276. Mullangi, D.; Shalini, S.; Nandi, S.; Choksi, B.; Ramanathan, V., Super-hydrophobic Covalent Organic Frameworks for Chemical Resistant Coatings, Hydrophobic Paper and Textile Composites. *Journal of Materials Chemistry A* **2017**, *5* (18), 8376-8384

277. Sai, H.; Fu, R.; Xing, L.; Xiang, J.; Li, Z.; Li, F.; Zhang, T., Surface modification of bacterial cellulose aerogels' web-like skeleton for oil/water separation. *ACS Applied Materials & Interfaces* **2015,** *7* (13), 7373-7381.

278. Zeng, M.; Peng, B.; Ybanez, C.; Tan, N. W.; Deeb, E. A.; Bordovsky, E.; Choi, C.-H.; Echols, I.; Nguyen, A.; Ye, A.; Dendumrongsup, N.; Zhang, L.; Huang, D.; Wang, P.; Luo, J.; Situ, Y.; Cheng, Z., High-flux underwater superoleophobic hybrid membranes for effective oil-water separation from oil-contaminated water. *RSC Advances* **2017,** *7* (15), 9051-9056.

279. Ge, J.; Shi, L.-A.; Wang, Y.-C.; Zhao, H.-Y.; Yao, H.-B.; Zhu, Y.-B.; Zhang, Y.; Zhu, H.-W.; Wu, H.-A.; Yu, S.-H., Joule-heated graphene-wrapped sponge enables fast clean-up of viscous crude-oil spill. *Nature Nanotechnology* **2017,** *12* (5), 434.

280. Fakhru'l-Razi, A.; Pendashteh, A.; Abdullah, L. C.; Biak, D. R. A.; Madaeni, S. S.; Abidin, Z. Z., Review of technologies for oil and gas produced water treatment. *Journal of Hazardous Materials* **2009,** *170* (2), 530-551.

281. Gupta, V. K.; Ali, I.; Saleh, T. A.; Nayak, A.; Agarwal, S., Chemical treatment technologies for waste-water recycling—an overview. *RSC Advances* **2012,** *2* (16), 6380-6388.

282. Peng, B.; Zhang, L.; Luo, J.; Wang, P.; Ding, B.; Zeng, M.; Cheng, Z., A review of nanomaterials for nanofluid enhanced oil recovery. *RSC Advances* **2017,** *7* (51), 32246-32254.

283. Fu, F.; Wang, Q., Removal of heavy metal ions from wastewaters: a review. *Journal of Environmental Management* **2011,** *92* (3), 407-418.

284. Zhang, Y.-q.; Xie, B.-j.; Gan, X., Advance in the applications of konjac glucomannan and its derivatives. *Carbohydrate Polymers* **2005,** *60* (1), 27-31.

285. Xu, C.; Luo, X.; Lin, X.; Zhuo, X.; Liang, L., Preparation and characterization of polylactide/thermoplastic konjac glucomannan blends. *Polymer* **2009,** *50* (15), 3698-3705.

286. Meng, F.; Zheng, L.; Wang, Y.; Liang, Y.; Zhong, G., Preparation and properties of konjac glucomannan octenyl succinate modified by microwave method. *Food Hydrocolloids* **2014,** *38*, 205-210.

287. Niu, C.; Wu, W.; Wang, Z.; Li, S.; Wang, J., Adsorption of heavy metal ions from aqueous solution by crosslinked carboxymethyl konjac glucomannan. *Journal of Hazardous Materials* **2007,** *141* (1), 209-214.

288. Liu, F.; Luo, X.; Lin, X., Adsorption of tannin from aqueous solution by deacetylated konjac glucomannan. *Journal of Hazardous Materials* **2010,** *178* (1), 844-850.

289. Gan, L.; Shang, S.; Hu, E.; Yuen, C. W. M.; Jiang, S.-x., Konjac glucomannan/graphene oxide hydrogel with enhanced dyes adsorption capability for methyl blue and methyl orange. *Applied Surface Science* **2015,** *357*, 866-872.

290. Guelcher, S. A.; Gallagher, K. M.; Didier, J. E.; Klinedinst, D. B.; Doctor, J. S.; Goldstein, A. S.; Wilkes, G. L.; Beckman, E. J.; Hollinger, J. O., Synthesis of biocompatible segmented polyurethanes from aliphatic diisocyanates and diurea diol chain extenders. *Acta Biomaterialia* **2005,** *1* (4), 471-484.

291. Zia, K. M.; Zuber, M.; Bhatti, I. A.; Barikani, M.; Sheikh, M. A., Evaluation of biocompatibility and mechanical behavior of chitin-based polyurethane elastomers. Part-II: Effect of diisocyanate structure. *International Journal of Biological Macromolecules* **2009,** *44* (1), 23-28.

292. Wang, X.; Zeng, M.; Yu, Y.-H.; Wang, H.; Mannan, M. S.; Cheng, Z., Thermosensitive ZrP-PNIPAM Pickering Emulsifier and the Controlled-release Behavior. *ACS Applied Materials & Interfaces* **2017**, 9(8), 7852-7858.

293. Zeng, M.; Wang, X.; Yu, Y.-H.; Zhang, L.; Shafi, W.; Huang, X.; Cheng, Z., The Synthesis of Amphiphilic Luminescent Graphene Quantum Dot and Its Application in Miniemulsion Polymerization. *Journal of Nanomaterials* **2016,** *2016*, 8.

294. Liu, X.; Ge, L.; Li, W.; Wang, X.; Li, F., Layered Double Hydroxide Functionalized Textile for Effective Oil/Water Separation and Selective Oil Adsorption. *ACS Applied Materials & Interfaces* **2015,** *7* (1), 791-800.

295. Jang, H. Y.; Zhang, K.; Chon, B. H.; Choi, H. J., Enhanced oil recovery performance and viscosity characteristics of polysaccharide xanthan gum solution. *Journal of Industrial and Engineering Chemistry* **2015,** *21*, 741-745.

296. Muller, G.; Aurhourrache, M.; Lecourtier, J.; Chauveteau, G., Salt dependence of the conformation of a single-stranded xanthan. *International Journal of Biological Macromolecules* **1986,** *8* (3), 167-172.

297. Macdonald, N. P.; Zhu, F.; Hall, C.; Reboud, J.; Crosier, P.; Patton, E.; Wlodkowic, D.; Cooper, J., Assessment of biocompatibility of 3D printed photopolymers using zebrafish embryo toxicity assays. *Lab on a Chip* **2016,** *16* (2), 291-297.

298. Nurunnabi, M.; Khatun, Z.; Huh, K. M.; Park, S. Y.; Lee, D. Y.; Cho, K. J.; Lee, Y.-k., In vivo biodistribution and toxicology of carboxylated graphene quantum dots. *ACS Nano* **2013,** *7* (8), 6858-6867.

299. Sverdrup, L. E.; Krogh, P. H.; Nielsen, T.; Kjær, C.; Stenersen, J., Toxicity of eight polycyclic aromatic compounds to red clover (Trifolium pratense), ryegrass (Lolium perenne), and mustard (Sinapsis alba). *Chemosphere* **2003,** *53* (8), 993-1003.

300. Maila, M. P.; Cloete, T. E., Germination of Lepidium sativum as a method to evaluate polycyclic aromatic hydrocarbons (PAHs) removal from contaminated soil. *International Biodeterioration & Biodegradation* **2002,** *50* (2), 107-113.

301. Henner, P.; Schiavon, M.; Druelle, V.; Lichtfouse, E., Phytotoxicity of ancient gaswork soils. Effect of polycyclic aromatic hydrocarbons (PAHs) on plant germination. *Organic Geochemistry* **1999,** *30* (8), 963-969.

302. Smith, M.; Flowers, T.; Duncan, H.; Alder, J., Effects of polycyclic aromatic hydrocarbons on germination and subsequent growth of grasses and legumes in freshly contaminated soil and soil with aged PAHs residues. *Environmental Pollution* **2006,** *141* (3), 519-525.

303. McCormick, K.; Panozzo, J.; Hong, S., A swelling power test for selecting potential noodle quality wheats. *Australian Journal of Agricultural Research* **1991,** *42* (3), 317-323.

304. Chen, S.-H.; Liu, L.; Fratini, E.; Baglioni, P.; Faraone, A.; Mamontov, E., Observation of fragile-to-strong dynamic crossover in protein hydration water. *Proceedings of the National Academy of Sciences* **2006,** *103* (24), 9012-9016.

305. Timasheff, S. N., Protein-solvent preferential interactions, protein hydration, and the modulation of biochemical reactions by solvent components. *Proceedings of the National Academy of Sciences* **2002,** *99* (15), 9721-9726.

306. Guo, Y.; Yang, S.; Fu, W.; Qi, J.; Li, R.; Wang, Z.; Xu, H., Adsorption of malachite green on micro-and mesoporous rice husk-based active carbon. *Dyes and Pigments* **2003,** *56* (3), 219-229.

307. Tan, K. B.; Vakili, M.; Horri, B. A.; Poh, P. E.; Abdullah, A. Z.; Salamatinia, B., Adsorption of dyes by nanomaterials: recent developments and adsorption mechanisms. *Separation and Purification Technology* **2015,** *150*, 229-242.

308. Crini, G., Non-conventional low-cost adsorbents for dye removal: a review. *Bioresource Technology* **2006,** *97* (9), 1061-1085.

309. Ghorai, S.; Sarkar, A.; Raoufi, M.; Panda, A. B.; Schönherr, H.; Pal, S., Enhanced removal of methylene blue and methyl violet dyes from aqueous solution using a nanocomposite of hydrolyzed polyacrylamide grafted xanthan gum and incorporated nanosilica. *ACS Applied Materials & Interfaces* **2014,** *6* (7), 4766-4777.

310. Pavan, F. A.; Lima, E. C.; Dias, S. L.; Mazzocato, A. C., Methylene blue biosorption from aqueous solutions by yellow passion fruit waste. *Journal of Hazardous Materials* **2008,** *150* (3), 703-712.

311. Paulino, A. T.; Guilherme, M. R.; Reis, A. V.; Campese, G. M.; Muniz, E. C.; Nozaki, J., Removal of methylene blue dye from an aqueous media using superabsorbent hydrogel supported on modified polysaccharide. *Journal of Colloid and Interface Science* **2006,** *301* (1), 55-62.

312. Pal, S.; Ghorai, S.; Das, C.; Samrat, S.; Ghosh, A.; Panda, A. B., Carboxymethyl tamarind-g-poly (acrylamide)/silica: a high performance hybrid nanocomposite for adsorption of methylene blue dye. *Industrial & Engineering Chemistry Research* **2012,** *51* (48), 15546-15556.

313. Hancock, R. D.; Martell, A. E., Ligand design for selective complexation of metal ions in aqueous solution. *Chemical Reviews* **1989,** *89* (8), 1875-1914.

314. Sahni, S. K.; Reedijk, J., Coordination chemistry of chelating resins and ion exchangers. *Coordination Chemistry Reviews* **1984,** *59*, 1-139.

315. Bargardi, F. L.; Le Ferrand, H.; Libanori, R.; Studart, A. R., Bio-inspired self-shaping ceramics. *Nature Communications* **2016,** *7*, 13912.

316. Roth, W. J.; Gil, B.; Makowski, W.; Marszalek, B.; Eliášová, P., Layer like porous materials with hierarchical structure. *Chemical Society Reviews* **2016,** *45* (12), 3400-3438.

317. Nandy, K.; Palmeri, M.; Burke, C.; An, Z.; Nguyen, S.; Putz, K.; Brinson, L., Stop Motion Animation Reveals Formation Mechanism of Hierarchical Structure in Graphene Oxide Papers. *Advanced Materials Interfaces* **2016,** *3* (6), 1500666.

318. Webber, M. J.; Appel, E. A.; Meijer, E.; Langer, R., Supramolecular biomaterials. *Nature Materials* **2016,** *15* (1), 13.

319. Wei, J.; Hu, Y.; Wu, Z.; Liang, Y.; Leong, S.; Kong, B.; Zhang, X.; Zhao, D.; Simon, G. P.; Wang, H., A graphene-directed assembly route to hierarchically porous Co–N x/C catalysts for high-performance oxygen reduction. *Journal of Materials Chemistry A* **2015,** *3* (32), 16867-16873.

320. Tang, C.; Li, B. Q.; Zhang, Q.; Zhu, L.; Wang, H. F.; Shi, J. L.; Wei, F., CaO-Templated Growth of Hierarchical Porous Graphene for High-Power Lithium–Sulfur Battery Applications. *Advanced Functional Materials* **2016,** *26* (4), 577-585.

321. Zeng, M.; Echols, I.; Wang, P.; Lei, S.; Luo, J.; Peng, B.; He, L.; Zhang, L.; Huang, D.; Mejia, C.; Wang, L.; Mannan, M. S.; Cheng, Z., Highly Biocompatible, Underwater Superhydrophilic and Multifunctional Biopolymer Membrane for Efficient Oil–Water Separation and Aqueous Pollutant Removal. *ACS Sustainable Chemistry & Engineering* **2018,** *6* (3), 3879-3887.

322. Verho, T.; Korhonen, J. T.; Sainiemi, L.; Jokinen, V.; Bower, C.; Franze, K.; Franssila, S.; Andrew, P.; Ikkala, O.; Ras, R. H., Reversible switching between superhydrophobic states on a hierarchically structured surface. *Proceedings of the National Academy of Sciences* **2012,** *109* (26), 10210-10213.

323. Du, R.; Gao, X.; Feng, Q.; Zhao, Q.; Li, P.; Deng, S.; Shi, L.; Zhang, J., Microscopic dimensions engineering: stepwise manipulation of the surface wettability on 3d substrates for oil/water separation. *Advanced Materials* **2016,** *28* (5), 936-942.

324. Li, J.; Shi, L.; Chen, Y.; Zhang, Y.; Guo, Z.; Su, B.-l.; Liu, W., Stable superhydrophobic coatings from thiol-ligand nanocrystals and their application in oil/water separation. *Journal of Material Chemistry* **2012,** *22* (19), 9774-9781.

325. Gao, X.; Zhou, J.; Du, R.; Xie, Z.; Deng, S.; Liu, R.; Liu, Z.; Zhang, J., Robust Superhydrophobic Foam: A Graphdiyne-Based Hierarchical Architecture for Oil/Water Separation. *Advanced Materials* **2016,** *28* (1), 168-173.

326. Hou, C.; Huang, T.; Wang, H.; Yu, H.; Zhang, Q.; Li, Y., A strong and stretchable self-healing film with self-activated pressure sensitivity for potential artificial skin applications. *Scientific Reports* **2013,** *3,* 3138.

327. Nie, W.; Blancon, J.-C.; Neukirch, A. J.; Appavoo, K.; Tsai, H.; Chhowalla, M.; Alam, M. A.; Sfeir, M. Y.; Katan, C.; Even, J., Light-activated photocurrent degradation and self-healing in perovskite solar cells. *Nature Communications* **2016,** *7,* 11574.

328. Vimalanandan, A.; Lv, L. P.; Tran, T. H.; Landfester, K.; Crespy, D.; Rohwerder, M., Redox-Responsive Self-Healing for Corrosion Protection. *Advanced Materials* **2013,** *25* (48), 6980-6984.

329. Thakur, V. K.; Kessler, M. R., Self-healing polymer nanocomposite materials: A review. *Polymer* **2015,** *69*, 369-383.

330. Jin, H.; Mangun, C. L.; Griffin, A. S.; Moore, J. S.; Sottos, N. R.; White, S. R., Thermally Stable Autonomic Healing in Epoxy using a Dual-Microcapsule System. *Advanced Materials* **2014,** *26* (2), 282-287.

331. Blaiszik, B.; Kramer, S.; Olugebefola, S.; Moore, J. S.; Sottos, N. R.; White, S. R., Self-healing polymers and composites. *Annual Review of Materials Research* **2010,** *40*, 179-211.

332. Norris, C.; Bond, I.; Trask, R., Healing of low-velocity impact damage in vascularised composites. *Composites Part A: Applied Science and Manufacturing* **2013,** *44*, 78-85.

333. Meure, S.; Furman, S.; Khor, S., Poly [ethylene-co-(methacrylic acid)] Healing Agents for Mendable Carbon Fiber Laminates. *Macromolecular Materials and Engineering* **2010,** *295* (5), 420-424.

334. Patrick, J. F.; Hart, K. R.; Krull, B. P.; Diesendruck, C. E.; Moore, J. S.; White, S. R.; Sottos, N. R., Continuous Self-Healing Life Cycle in Vascularized Structural Composites. *Advanced Materials* **2014,** *26* (25), 4302-4308.

335. Fang, W.; Liu, L.; Li, T.; Dang, Z.; Qiao, C.; Xu, J.; Wang, Y., Electrospun N-Substituted Polyurethane Membranes with Self-Healing Ability for Self-Cleaning and Oil/Water Separation. *Chemistry -A European Journal* **2016,** *22* (3), 878-883.

336. Zhou, H.; Wang, H.; Niu, H.; Fang, J.; Zhao, Y.; Lin, T., Superstrong, Chemically Stable, Superamphiphobic Fabrics from Particle-Free Polymer Coatings. *Advanced Materials Interfaces* **2015,** *2* (6), 1400559.

337. Hori, H.; Yamamoto, A.; Hayakawa, E.; Taniyasu, S.; Yamashita, N.; Kutsuna, S.; Kiatagawa, H.; Arakawa, R., Efficient decomposition of environmentally persistent perfluorocarboxylic acids by use of persulfate as a photochemical oxidant. *Environmental Science & Technology* **2005,** *39* (7), 2383-2388.

338. Marechal, M.; Cuetos, A.; Martínez-Haya, B.; Dijkstra, M., Phase behavior of hard colloidal platelets using free energy calculations. *The Journal of Chemical Physics* **2011,** *134* (9), 94501.

339. Sun, D.; Sue, H.-J.; Cheng, Z.; Martínez-Ratón, Y.; Velasco, E., Stable smectic phase in suspensions of polydisperse colloidal platelets with identical thickness. *Physical Review E* **2009,** *80* (4), 41704.

340. Chang, Y.-W.; Mejia, A. F.; Cheng, Z.; Di, X.; McKenna, G. B., Gelation via Ion Exchange in Discotic Suspensions. *Physical Review Letters* **2012,** *108* (24), 247802.

341. Chen, Z.; Pronkin, S.; Fellinger, T.-P.; Kailasam, K.; Vilé, G.; Albani, D.; Krumeich, F.; Leary, R.; Barnard, J.; Thomas, J. M., Merging Single-Atom-Dispersed Silver and Carbon Nitride to a Joint Electronic System via Copolymerization with Silver Tricyanomethanide. *ACS Nano* **2016,** *10* (3), 3166-3175.

342. Kaschak, D. M.; Johnson, S. A.; Hooks, D. E.; Kim, H. N.; Ward, M. D.; Mallouk, T. E., Chemistry on the edge: A microscopic analysis of the intercalation, exfoliation, edge functionalization, and monolayer surface tiling reactions of alpha-zirconium phosphate. *Journal of the American Chemical Society* **1998,** *120* (42), 10887-10894.

343. Xue, C.-H.; Bai, X.; Jia, S.-T., Robust, self-healing superhydrophobic fabrics prepared by one-step coating of PDMS and octadecylamine. *Scientific Reports* **2016,** *6*, 27262.

344. Kowalonek, J.; Kaczmarek, H.; Dąbrowska, A., Air plasma or UV-irradiation applied to surface modification of pectin/poly (vinyl alcohol) blends. *Applied Surface Science* **2010,** *257* (1), 325-331.

345. Chen, K.; Zhou, S.; Wu, L., Self-Healing Underwater Superoleophobic and Anti-Biofouling Coatings Based on the Assembly of Hierarchical Microgel Spheres. *ACS Nano* **2016**, *10*, 1386-1394.

346. Wang, H.; Xue, Y.; Ding, J.; Feng, L.; Wang, X.; Lin, T., Durable, Self-Healing Superhydrophobic and Superoleophobic Surfaces from Fluorinated-Decyl Polyhedral Oligomeric Silsesquioxane and Hydrolyzed Fluorinated Alkyl Silane. *Angewandte Chemie International Edition* **2011,** *50* (48), 11433-11436.

347. Chen, S.; Li, X.; Li, Y.; Sun, J., Intumescent flame-retardant and self-healing superhydrophobic coatings on cotton fabric. *ACS Nano* **2015,** *9* (4), 4070-4076.

348. Wu, M.; Ma, B.; Pan, T.; Chen, S.; Sun, J., Silver-Nanoparticle-Colored Cotton Fabrics with Tunable Colors and Durable Antibacterial and Self-Healing Superhydrophobic Properties. *Advanced Functional Materials* **2016,** *26* (4), 569-576.

349. Kwon, G.; Kota, A.; Li, Y.; Sohani, A.; Mabry, J. M.; Tuteja, A., On-demand separation of oil-water mixtures. *Advanced Materials* **2012,** *24* (27), 3666-3671.

350. Xue, Z.; Cao, Y.; Liu, N.; Feng, L.; Jiang, L., Special wettable materials for oil/water separation. *Journal of Materials Chemistry A* **2014,** *2* (8), 2445-2460.

351. Patrick, J. F.; Robb, M. J.; Sottos, N. R.; Moore, J. S.; White, S. R., Polymers with autonomous life-cycle control. *Nature* **2016,** *540* (7633), 363-370.

352. Li, C.-H.; Wang, C.; Keplinger, C.; Zuo, J.-L.; Jin, L.; Sun, Y.; Zheng, P.; Cao, Y.; Lissel, F.; Linder, C., A highly stretchable autonomous self-healing elastomer. *Nature Chemistry* **2016,** *8* (6), 618-624.